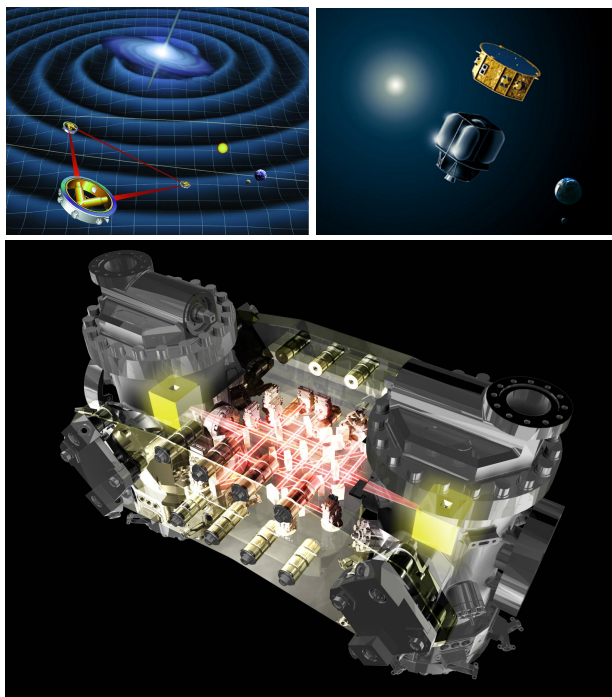# GRAVITATIONAL WAVE OBSERVATION FROM SPACE: OPTICAL MEASUREMENT TECHNIQUES FOR LISA AND LISA PATHFINDER

FELIPE GUZMÁN CERVANTES

Felipe Guzmán Cervantes

Gravitational Wave Observation from Space:
optical measurement techniques for LISA and LISA Pathfinder

GRAVITATIONAL WAVE OBSERVATION FROM SPACE: OPTICAL MEASUREMENT TECHNIQUES FOR LISA AND LISA PATHFINDER

Der Fakultät für Mathematik und Physik der
Gottfried Wilhelm Leibniz Universität Hannover
zur Erlangung des Grades

**Doktor der Naturwissenschaften
– Dr. rer. nat. –**

genehmigte Dissertation von

Felipe Guzmán Cervantes, M.Sc.

geboren am 24. September 1980 in San José, Costa Rica

2009

Referent: Prof. Dr. Karsten Danzmann
Koreferent: Dr. Henry Ward

Tag der Promotion: 19. Juni 2009

A mis padres
y a la fuerza que me levanta
cuando no puedo ponerme de pie ...

ABSTRACT

The Laser Interferometer Space Antenna (LISA) is a joint ESA-NASA mission designed as the first space-based gravitational wave observatory and will operate in the frequency range between 0.1 mHz to 100 mHz. LISA will complement the ground-based observatories, as these low frequencies are inaccessible to detectors on Earth due to seismic noise predominance at frequencies lower than 10 Hz. LISA is a constellation of three identical spacecraft separated by 5 million kilometers, flying free-falling test masses. Relative changes in the separation between test masses located in different satellites reveal the presence of gravitational waves. LISA requires a measurement accuracy of better than $40\,\mathrm{pm}/\sqrt{\mathrm{Hz}}$, which is achieved by means of precision laser interferometry.

Due to the challenges LISA represents, ESA plans to launch the technology demonstration mission LISA Pathfinder in order to test LISA core technologies in the frequency range from $3-30\,\mathrm{mHz}$. A high precision laser interferometer with picometer accuracy has been included to measure the displacement and attitude of the free-falling test masses and produces input signals for the test mass drag-free and spacecraft control.

This thesis describes three experiments related to LISA and LISA Pathfinder: an optical cavity, a phase-modulated homodyne interferometer, and a heterodyne interferometer were set up and characterized for test mass position and attitude measurements. During investigations on the LISA Pathfinder (LPF) interferometry, two testbeds were further developed: a laboratory test setup and a test facility for engineering models of subunits of the optical metrology system. The two setups and the results obtained are compared and described in detail.

Hardware simulations of the expected in-orbit cross-talk between test mass angular and displacement degrees of freedom have been conducted. Noise subtraction algorithms have been developed to correct for sensitivity limiting effects like the coupling of test mass jitter into displacement readout, and fluctuations of the laser frequency and the non-linear optical pathlength difference. A previously developed real-time wavefront detector has been used to help the adequate beam preparation, the manufacture of quasi-monolithic fiber injectors for the LPF optical bench, and the characterization of the LPF optical window.

Keywords: gravitational wave detection in space, laser interferometry, noise subtraction, data analysis

KURZZUSAMMENFASSUNG

Die gemeinsame ESA-NASA-Mission Laser Interferometer Space Antenna (LISA) wird als das erste weltraumgestützte Gravitationswellenobservatorium im Frequenzbereich von 0.1 mHz bis 100 mHz konzipiert. LISA ergänzt hiermit erdgebundene Gravitationswellendetektoren, deren Empfindlichkeit durch seismisches Rauschen der Erde unterhalb 10 Hz begrenzt ist. LISA besteht aus drei identischen Satelliten in einem Abstand von 5 Millionen km mit frei fliegenden Testmassen. Von Gravitationswellen hervorgerufene relative Abstandsänderungen zwischen zwei Testmassen werden mit einer Genauigkeit besser als $40\,\mathrm{pm}/\sqrt{\mathrm{Hz}}$ mittels hochempfindlicher Laserinterferometrie gemessen. Aufgrund der technologischen Herausforderungen von LISA beschloss die ESA, vor LISA den Technologiedemonstrator LISA Pathfinder (LPF) zu starten, der LISA Kerntechnologien im Frequenzbereich $3-30\,\mathrm{mHz}$ erprobt. Ein Laserinterferometer mit picometer-Genauigkeit wird zur Abstands- und Winkelmessung der Testmassen verwendet und generiert Signale zur Testmassen und Satellitenansteuerung.

In dieser Arbeit werden drei Experimente für LISA und LISA Pathfinder behandelt: ein optischer Resonator, ein phasenmoduliertes Homodyninterferometer und ein Heterodyninterferometer wurden aufgebaut und charakterisiert, um Testmassenpositionen und Winkel zu messen.

Im Rahmen der LISA Pathfinder Interferometrie wurden zwei Testaufbauten weiterentwickelt: ein Labortestaufbau und ein Testaufbau für die Prototypen der Flugmodelle (Engineering Models). Die Aufbauten und damit erzielten Ergebnisse werden beschrieben und verglichen.

Laborhardwaresimulationen der im Weltraumflug zu erwartenden Kreuzkopplung zwischen Winkel- und Abstandsfreiheitsgraden der Testmassen wurden durchgeführt. Rauschsubtraktionsalgorithmen wurden zur Korrektur von Faktoren, die die Empfindlichkeit begrenzen, entwickelt, wie z.B. Testmassenrestwinkelrauschen, Laserfrequenz- und nicht-lineare optische Weglängenfluktuationen. Ein zuvor entwickelter Wellenfrontdetektor wurde charakterisiert und bei der Herstellung quasimonolithischer Faserauskoppler für LPF und bei der Charakterisierung des optischen Fensters in LPF eingesetzt.

Schlagworte: Gravitationswellendetektion im Weltraum, Laserinterferometrie, Rauschsubtraction, Datenanalyse

CONTENTS

LIST OF FIGURES

LIST OF TABLES

ACRONYMS

AAF   anti-alasing filter

ADC   analog-to-digital converter

AEI   Albert Einstein Institute Hannover

AOM   acousto-optic modulators

AR   anti-reflection

CCD   charge-coupled device

CTE   coefficient of thermal expansion

DAC   digital-to-analog converter

DAQ   data acquisition system

DDS   direct digital synthesizer

DFACS   drag-free and attitude control system

DFT   Discrete Fourier Transform

DMU   data management unit

DOF   degree of freedom

DRS   Disturbance Reduction System

DSP   digital signal processor

DWS   differential wavefront sensing

EGSE   electrical ground support equipment

EH   electrode housing

EM   engineering model

EOM   electro-optic modulator

ESA   European Space Agency

FFT   Fast Fourier Transform

FIOS   fiber injector optical subassembly

FM   flight model

FPGA   Field Programmable Gate Array

GUI   graphical user interface

HV   high-voltage

IGR   Institute for Gravitational Research

IIR   infinite impulse response

InGaAs Indium Gallium Arsenide

ITO   Indium-Tin Oxide

KTM   Kayser-Threde Munich

LA   laser assembly

LISA   Laser Interferometer Space Antenna

LMU   laser modulator unit

LPF   LISA Pathfinder

LSD   linear spectral density

LTP   LISA Technology Package

LTPDA   LTP data analysis tool

Nd:YAG neodymium-doped yttrium aluminium garnet

NPRO   non-planar ring oscillator

OB   optical bench

OBC   onboard computer

OLG   open loop gain

OMS   optical metrology system

OPD   optical pathlength difference

PAAM   point-ahead angle mechanism

PC   personal computer

PD-AMP   transimpedance amplifier

PLL   phase-locked loop

PMS   phase measurement system

PDH   Pound-Drever-Hall

PZT   piezo-electric transducer

QPD   quadrant photodetector

RLU   reference laser unit

RF   radio frequency

SBFT   single-bin discrete Fourier Transform

SH   sample-and-hold

SNR   signal-to-noise ratio

TCVCXO   temperature compensated voltage-controlled crystal oscillator

TF   transfer function

TM   test mass

TUM   Technische Universität München

TTL   transistor-transistor logic

ULE   ultra-low expansion

INTRODUCTION

In his General Theory of Relativity presented in 1915[1] [1], Albert Einstein introduced a model for the geometric description of Gravitation as the spacetime curvature produced by masses and radiation present in it (see Figure 1 [2]).
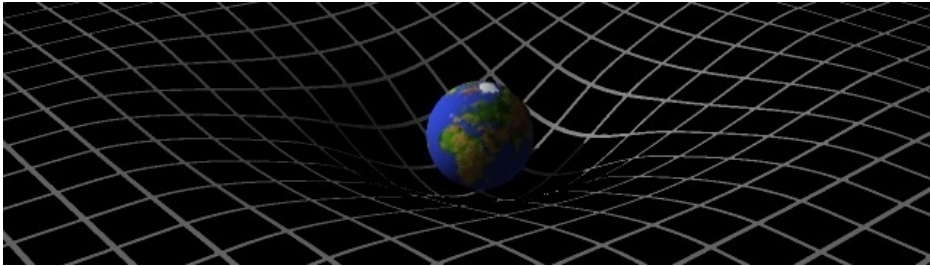
Figure 1: Illustration of Gravitation as the geometric curvature of spacetime.

Accelerated masses excite oscillations[2] of the spacetime itself which propagate at the speed of light and are called gravitational waves. Their theoretically predicted interaction with other physical phenomena is very small, which helps to preserve high quality information on the cosmological events emitting them while the waves travel through the universe. However, this fact also make gravitational waves extremely challenging to detect.

Current astronomy is mainly based on the detection of electromagnetic radiation emitted by celestial bodies and their interactions. Due to the fundamental difference in the physical process of their emission, the detection of gravitational radiation opens a completely novel field in astronomy that enables to reach a more extensive understanding of the universe and would help probe essential questions about its very origin and evolution.

---

1 Lecture given at the Preußische Akademie der Wissenschaften.
2 "Similarly" to a ball moving on a rubber elastic bandage.

GRAVITATIONAL WAVE OBSERVATION

The functional principle of laser interferometric gravitational wave detectors is based on measuring the distance between test masses – suspended mirrors of the interferometer – that changes at the pass of a gravitational wave.

The scientific community has been investing a considerable effort in the setup of a worldwide network consisting of five ground-based laser interferometric gravitational wave observatories.

Variations in the gravitational field of the Earth restrict the measurement bandwidth of these detectors to frequencies above a few hertz.

Therefore, a space-based gravitational wave observatory is currently under development in order to complement the ground-based network observation bandwidth in the millihertz range.

LISA: LASER INTERFEROMETER SPACE ANTENNA

The Laser Interferometer Space Antenna (LISA) is the first space-based laser interferometric gravitational wave observatory, designed to operate in the frequency band between 10^{-4} and 10^{-1} Hz. Astrophysical sources such as super massive black hole binaries, coalescences and mergers, as well as a cosmological gravitational wave background are expected to be detectable in this frequency range.

LISA is a joint mission between the European Space Agency (ESA) and NASA, and consists of three identical spacecraft in an equilateral triangle formation, separated by 5 million kilometers. The LISA triangular constellation follows the Earth at a distance of 50 million km (20°) in a heliocentric orbit at 1 AU from the Sun. The plane of this assembly is tilted by 60° with respect to the ecliptic as shown in Figure 2.

LISA flies a total of six drag-free test masses, two in each spacecraft, and measures variations in their separation originating from gravitational waves with an accuracy of $40\,\mathrm{pm}/\sqrt{\mathrm{Hz}}$ over their nominal separation of 5 million km, which corresponds to a relative length measurement precision of the order of $\frac{\delta L}{L} = 8 \times 10^{-21}\,/\sqrt{\mathrm{Hz}}$. In order to achieve this displacement sensitivity for the gravitational wave measurement, effects of non-gravitational forces have to be
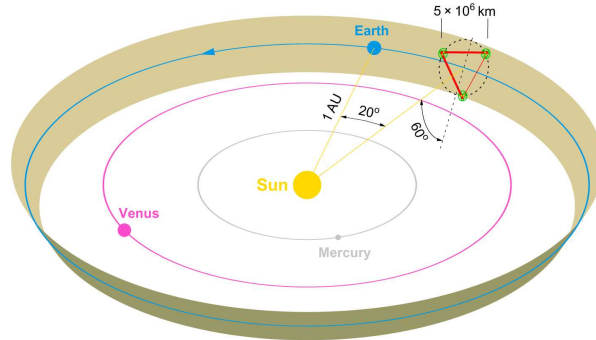
Figure 2: Heliocentric orbit of the spacecraft constituting LISA

suppressed below the level of $3 \times 10^{-15}\,\mathrm{N}/\sqrt{\mathrm{Hz}}$ at $3\,\mathrm{mHz}$ (see Figure 3).
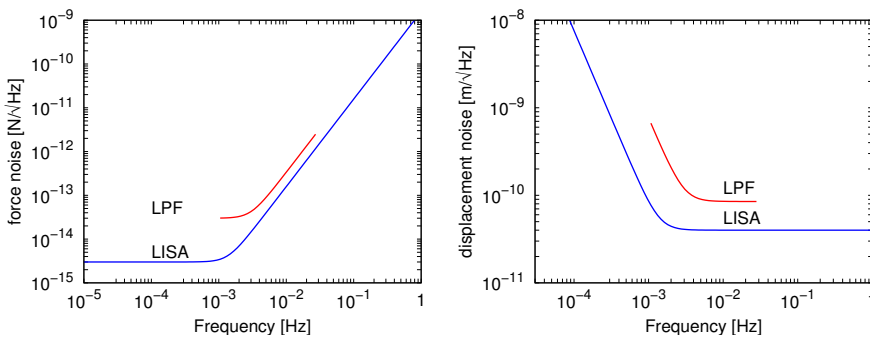
Figure 3: Force and displacement noise budgets for LISA and LISA Pathfinder

LISA PATHFINDER

LISA requires some novel technology that is under development and cannot be tested on Earth. It is therefore that ESA decided to launch the technology demonstration mission LISA Pathfinder (LPF) to test core technology in a similar space environment as is expected for LISA.

LPF consists of a single satellite that carries two experiments: the ESA payload LTP, and the Disturbance Reduction System (DRS) from NASA. This thesis concentrates on research topics concerning LTP only.

The main aim of LTP is to verify drag-free control of test masses to a level better than $3 \times 10^{-14}\,\mathrm{m\,s^{-2}}/\sqrt{\mathrm{Hz}}$ in the observation band of $3 - 30\,\mathrm{mHz}$.

A laser interferometer has been included with the capability of measuring the test mass with a displacement accuracy of $6.3\,\mathrm{pm}/\sqrt{\mathrm{Hz}}$ and an angular resolution of $20\,\mathrm{nrad}/\sqrt{\mathrm{Hz}}$ [3]. The requirements on the LTP test mass displacement noise are plotted in Figure 4.
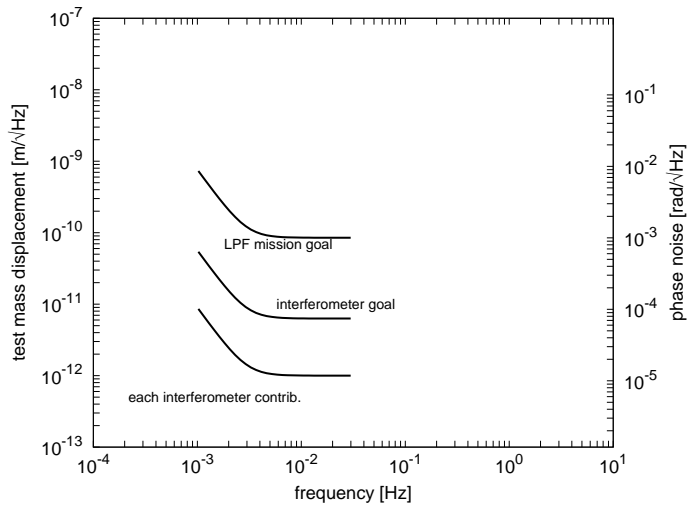
Figure 4: Requirements on the LTP test mass displacement noise

The upper trace at a level of $85\,\mathrm{pm}/\sqrt{\mathrm{Hz}}$ defines the requirement on the LTP test mass displacement noise under drag-free control. The middle trace at $6.3\,\mathrm{pm}/\sqrt{\mathrm{Hz}}$ defines the requirement on the accuracy of the optical metrology system for the test mass displacement measurement. The lower trace at $1\,\mathrm{pm}/\sqrt{\mathrm{Hz}}$ is the noise budget allocated to each noise source of the interferometer.

This thesis presents the development and implementation of three different optical metrology techniques for the measurement of test mass attitude and displacement:

1. **Part i**
   Introduces some common optical length and attitude measurement techniques used for the investigations presented in this thesis: resonant cavities, conventional and phase-modulated homodyne interferometry, heterodyne interferometry, and spatially resolving wavefront measurements.

2. **Part ii**
   Describes the design and initial testing of an optical cavity used for displacement measurements at the level of $1\,\mathrm{pm}/\sqrt{\mathrm{Hz}}$ in the millihertz frequency band. This facility was developed to test candidates for the LISA point-ahead angle mechanism.

3. **Part iii**
   Reports the development of a homodyne interferometry technique based on the deep phase modulation over several radians of one interferometer arm, reaching a sensitivity of the test mass displacement measurement at the level of $10\,\mathrm{pm}/\sqrt{\mathrm{Hz}}$ at millihertz frequencies.

4. **Part iv**
   Presents the status, as of May 2009, of the LTP interferometry, the development and testing of engineering models of its optical metrology subunits, and various performance investigations, concerning characterization of optical components, hardware simulation of in-orbit test mass behavior, and noise subtraction techniques.

Part I

OPTICAL MEASUREMENT TECHNIQUES
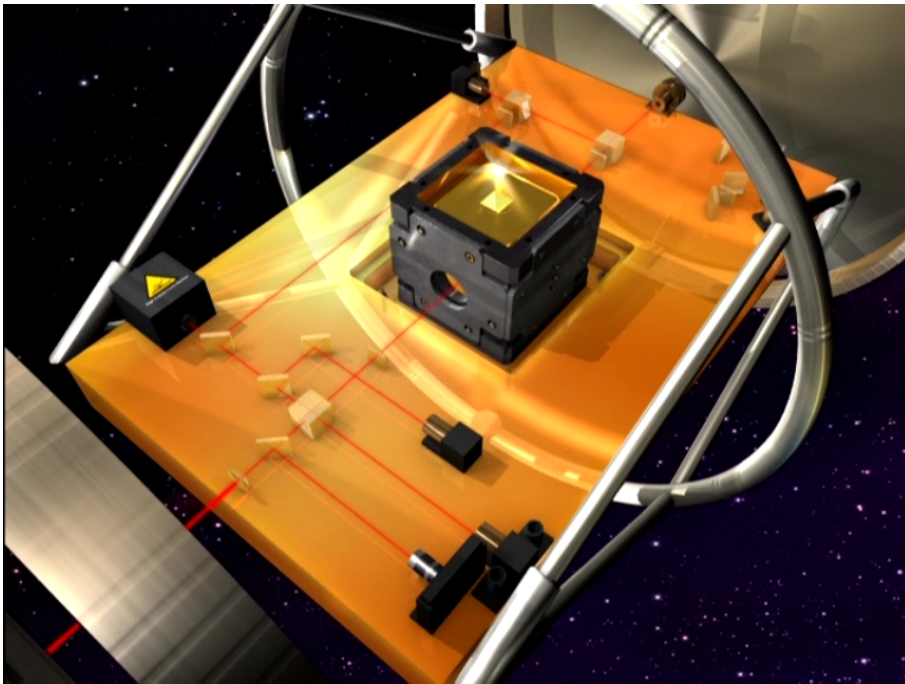
1

LENGTH AND ATTITUDE MEASUREMENT

The development of the laser in 1960 by Theodore Maiman at Hughes Research Laboratories set a technological milestone with a device that has become indispensable nowadays, being utilized in standard telecommunications, data storage, material processing, and almost all optical metrology systems in many different varieties and application areas, including space research and technology.

Especially in the field of optical metrology, where the physical properties of the employed light source often determine the precision of measurements, the high spatial and temporal coherence at an intense light beam provided by the laser, represented a revolution to the achievable accuracy of interferometers. The short and stable wavelength over large distances makes the laser an ideal reference *ruler* for very accurate distance measurements.

This chapter gives a short description of the physical principle of three different optical measurement techniques based on laser interferometry. The performance of each of these three methods at millihertz frequencies, as required for the optical metrology of LISA and LPF, has been experimentally assessed in the laboratory. The corresponding experimental setups and obtained results for each technique are presented in Parts ii, iii, and iv.

1.1 LENGTH MEASUREMENT

1.1.1 *Resonant cavity*

Optical cavities are commonly used as stable length reference for laser frequency stabilization in interferometry applications, due to the direct proportionality between laser frequency fluctuations and displacement noise.

To this end, the laser frequency ν is tuned by a control loop to the q-th resonance frequency ν_q of the optical cavity, which is given by [4]

$$\nu_q = q\,\frac{c}{2\,L}, \quad q \in \mathbb{N} \tag{1.1}$$

where $2\,L$ is the round-trip length of the cavity that is made stable for frequency stabilization purposes. Fluctuations δL of the cavity length translate as laser frequency fluctuations as [4, 5]

$$\frac{\delta\nu}{\nu} = \frac{\delta L}{L}, \tag{1.2}$$

This principle can be used to measure small displacement fluctuations of a given test mass in the optical path of the cavity, provided the remaining components are sufficiently stable. However, this can be usually applied for small fluctuations only in order to maintain the cavity in resonance within the operation fringe q.

Thus, in the case of LISA and LISA Pathfinder where the dynamic range of the test mass motion is of the order of several wavelengths of the laser beam, a different method must be applied.

Nevertheless, if the cavity can be held in resonance, this metrology technique reaches high accuracy by comparing the frequency of the laser beam to a sufficiently stable reference oscillator, which is typically a second laser stabilized to a frequency standard that can be, for instance, a more stable cavity or an atomic energy transition.

This can be done by overlapping the two laser beams and measuring the fluctuations of the beat note frequency resulting from the optical down mix process at the photodetector – optical heterodyning –, which is further explained in Section 1.1.2. Provided the frequency of the reference oscillator ν_{ref} is much more stable than the measurement cavity: $\delta\nu_{ref} \ll \delta\nu_{meas}$; the corresponding distance fluctuations of the test mass δL can be obtained as

$$\delta L = L\,\frac{\delta\nu_{meas}}{\nu_{meas}} \tag{1.3}$$

An example of the use of resonant cavities for the measurement of displacement fluctuations of a test mass is given in Part ii that is an investigation conducted for the stability assessment of potential candidates for the LISA point-ahead angle mechanism (PAAM), but can be similarly used for other optical metrology applications.

1.1.2 *Interferometers*

The representation of a light field $E(t)$ at a fixed point in space can be expressed as

$$E(t) = E \cdot e^{i \cdot (\omega t + \phi)}. \tag{1.4}$$

Given the two light fields $E_1(t)$ and $E_2(t)$

$$E_1(t) = E_1 \cdot e^{i \cdot (\omega_1 t + \phi_1)}$$

$$E_2(t) = E_2 \cdot e^{i \cdot (\omega_2 t + \phi_2)} \tag{1.5}$$

where $\omega_n = 2\pi \cdot f_n$ is the angular frequency and ϕ_n is the phase, their overlap at a beamsplitter, as shown in Figure 5, can be described as
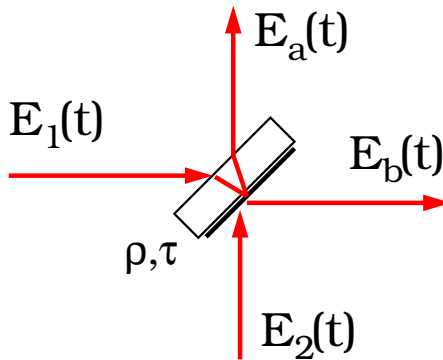
Figure 5: Recombination of light fields at a beamsplitter in an interferometer.

$$\begin{pmatrix} E_b(t) \\ E_a(t) \end{pmatrix} = \begin{pmatrix} i\tau & \rho \\ \rho & i\tau \end{pmatrix} \begin{pmatrix} E_1(t) \\ E_2(t) \end{pmatrix}$$

$$\begin{pmatrix} E_b(t) \\ E_a(t) \end{pmatrix} = \begin{pmatrix} i\tau \cdot E_1 \cdot e^{i \cdot (\omega_1 t + \phi_1)} + \rho \cdot E_2 \cdot e^{i \cdot (\omega_2 t + \phi_2)} \\ \rho \cdot E_1 \cdot e^{i \cdot (\omega_1 t + \phi_1)} + i\tau \cdot E_2 \cdot e^{i \cdot (\omega_2 t + \phi_2)} \end{pmatrix} \tag{1.6}$$

11

where $E_a(t)$ and $E_b(t)$ are the light fields emerging from the outputs of the beamsplitter.

The intensity $I_b(t)$ averaged over the THz carrier frequency and measured at a photodetector can be expressed as

$$|E_b|^2 \quad = \quad |\, i\tau \cdot E_1 \cdot e^{i \cdot (\omega_1 t + \phi_1)} + \rho \cdot E_2 \cdot e^{i \cdot (\omega_2 t + \phi_2)} \,|^2$$

$$= \left(i\tau E_1 \cdot e^{i(\omega_1 t + \phi_1)} + \rho E_2 \cdot e^{i(\omega_2 t + \phi_2)} \right) \left(i\tau E_1 \cdot e^{i(\omega_1 t + \phi_1)} + \rho E_2 \cdot e^{i(\omega_2 t + \phi_2)} \right)^*$$

$$= \left(i\tau E_1 \cdot e^{i(\omega_1 t + \phi_1)} + \rho E_2 \cdot e^{i(\omega_2 t + \phi_2)} \right) \left(-i\tau E_1 \cdot e^{-i(\omega_1 t + \phi_1)} + \rho E_2 \cdot e^{-i(\omega_2 t + \phi_2)} \right)$$

$$|E_b|^2 \quad = \quad \tau^2 \cdot E_1^2 + \rho^2 \cdot E_2^2 + i\tau\rho E_1 E_2 \underbrace{\left(e^{i \cdot (\omega_1 t + \phi_1)} - e^{-i \cdot (\omega_2 t + \phi_2)} \right)}_{2i\,\sin(\Delta\omega t + \Delta\phi)}$$

$$|E_b|^2 \quad = \quad \tau^2 \cdot E_1^2 + \rho^2 \cdot E_2^2 - 2\tau\rho E_1 E_2 \sin(\Delta\omega t + \Delta\phi) \tag{1.7}$$

where $\Delta\omega = \omega_1 - \omega_2 = \omega$ and $\Delta\phi = \phi_1 - \phi_2 = \phi$.

The effective signal V_{PD} measured at a photodetector can be expressed by

$$V_{PD}(t) = A\,[1 - c\cos(\omega t + \phi)], \tag{1.8}$$

where A combines nominally constant factors such as light power and detector efficiency, $c \leqslant 1$ is the interferometer contrast, ω is the frequency difference between the two interfering beams, also known as heterodyne frequency, and the phase shift ϕ is the interferometric measurand typically related to test mass displacements ΔL by

$$\phi = \frac{2\pi \Delta L}{\lambda} \tag{1.9}$$

where λ is the average wavelength of the two light fields $E_1(t)$ and $E_2(t)$ oscillating at the frequencies ω_1 and ω_2 respectively.

Specific interferometry techniques can be derived from the general interference of any two light fields:

Homodyne interferometer

Homodyne interferometry considers the case where the frequency of the two interfering electric fields is equal $\omega_1 = \omega_2 \Rightarrow \omega = 0$, which yields the following signal at the photodetector

$$V_{PD} = A \left[1 - c \cos(\phi) \right].$$ (1.10)

The length measurement is done by calibrating the interferometer phase to the photodetector output V_{PD} that corresponds to a DC readout.

In this case, the interferometer is usually set for small excursions about a predefined operating point in the linear range of the sinusoidal interferogram, which limits the dynamic range of the measurement to a this particular fraction of a fringe.

For this reason, similarly to the case of the resonant cavity, this technique cannot be considered for the readout of the test mass motion in LISA or LPF.

Phase-modulated homodyne interferometer

In order to overcome the dynamic range limitation of the basic homodyne interferometer, a modulation can be applied to one arm of the interferometer to encode the interferometer phase in the photodetector signal

$$V_{PD}(t) = A \left[1 - c \cos(\phi + m \cos(\omega_m t + \psi)) \right],$$ (1.11)

where m is the modulation depth (the amplitude of the modulation signal), ω_m is the modulation frequency, and ψ is the corresponding modulation phase.

The interferometer phase ϕ containing the test mass motion information can be extracted by proper demodulation of the photodetector signal that can be performed with different methods.

For small to moderate modulation depths $m \lesssim 1$, this technique is well-known and is used, for instance, in GEO600 [6] as "frontal (Schnupp) modulation". For large modulation depths $m \gg 1$, this modified technique offers the capability of measuring the test mass motion over a wide dynamic range with high accuracy, which makes it suitable for the local optical metrology of LISA and LPF.

An experimental demonstration of a novel deep phase modulation technique has been conducted and is described in detail in Part iii.

Heterodyne interferometer

In optical heterodyne detection, the frequencies of the interfering beams have a controlled difference that corresponds to a non-zero heterodyne frequency ω. Hence, the signal measured at the photodetector can be expressed as

$$V_{PD}(t) = A\left[1 - c\cos\left(\omega\,t + \phi\right)\right]. \tag{1.12}$$

The controlled time dependency of the signal does not require the interferometer to be set at a pre-determined phase operating point, which enables continuous measurement capabilities over a wide dynamic range.

This technique has been chosen as baseline optical metrology concept for the LPF interferometry, and its implementation and testing at laboratory breadboard level, engineering models, and associated performance and data analysis investigations are presented in detail in Part iv. LISA is also planned to be operated as a heterodyne interferometer.

1.2 ATTITUDE MEASUREMENT

Besides high precision test mass displacement measurements in the millihertz frequency band, it is also important in LISA and LISA Pathfinder to measure the test mass attitude. Due to the fact that the test masses are mirrors in the optical path of the interferometers, it is relevant to monitor their angular orientation in order to enable on-orbit auto-alignment procedures and characterization of cross-coupling between angular and displacement degrees of freedom (as explained in detail in Section 9.2).

To this end, the optical benches of LISA and LPF have been designed to include quadrant photodetectors at the interferometer outputs to allow this measurements.

Two different techniques can be applied: (a) a DC measurement is based on the calibration of the light power distribution on the quadrants of the photodetector, and (b) a second one uses the more sensitive differential phase measurement conducted at each quadrant "differential wavefront sensing (DWS)" [7, 8] to determine the test mass orientation. Variations from the calibrated nominal working point of each method provide information on the angular motion of the test masses, and can be applied in the same way to any of the phase measurement techniques described in Section 1.1.2.

Given the notation of the quadrant photodetector channels in Figure 6 and
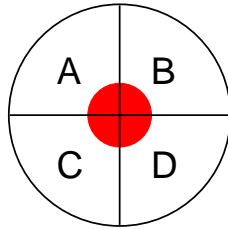
Figure 6: Notation of channels of a quadrant photodetector.

the incidence of the beams onto the photodetector as depicted in Figure 7, the
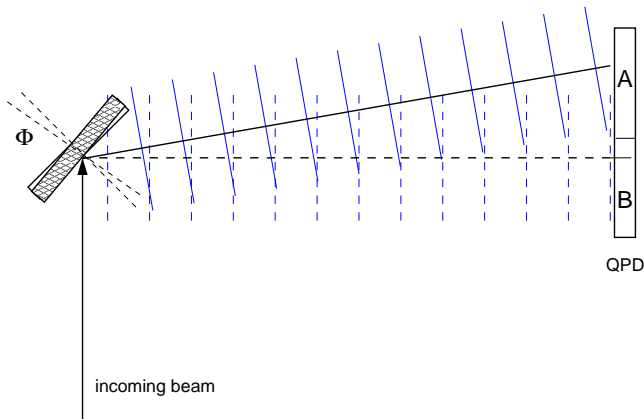
Figure 7: Representation of the beam incidence onto the photodetector for test mass angular measurements.

test mass attitude measurement techniques can be described as follows:

1.2.1 *DC angular measurement*

This technique is based on the measurement of the average light power distribution on the photodetector, consisting of the two overlapping beams. One beam has been precisely aligned on the center of the photodetector, and the

second one is being reflected on the test mass before reaching the photodetector. Angular jitter of the test mass will change the light power measurement at each individual quadrant, giving information on the test mass orientation.

The horizontal φ^{DC} and vertical η^{DC} angles can be computed as

$$\varphi^{DC} = \kappa^{DC} \frac{(\Sigma_A + \Sigma_C) - (\Sigma_B + \Sigma_D)}{\Sigma_A + \Sigma_C + \Sigma_B + \Sigma_D},$$

$$\eta^{DC} = \kappa^{DC} \frac{(\Sigma_A + \Sigma_B) - (\Sigma_C + \Sigma_D)}{\Sigma_A + \Sigma_C + \Sigma_B + \Sigma_D}, \tag{1.13}$$

where Σ_i is the light power measured at each quadrant $i = \{A, B, C, D\}$, and

$$\kappa^{DC} \approx \frac{L}{d} = 150 \, \text{rad/rad} \tag{1.14}$$

is the calibration factor of the DC measurement to real test mass angle, e.g., for a lever arm $L \approx 30 \, \text{cm}$ and a beam diameter $d \approx 2 \, \text{mm}$.

1.2.2 *Differential wavefront sensing*

In the more sensitive differential wavefront sensing (DWS) measurement of the test mass orientation, the phases between the interfering wavefronts at each quadrant are measured, determining the difference in geometry between the two interfering beams with a low but sufficient spatial resolution (4 pixels). The horizontal and angular orientation of the test mass can be nominally computed as

$$\varphi^{DWS} = \kappa^{DWS} \left[(\phi_A + \phi_C) - (\phi_B + \phi_D) \right],$$

$$\eta^{DWS} = \kappa^{DWS} \left[(\phi_A + \phi_B) - (\phi_C + \phi_D) \right], \tag{1.15}$$

where ϕ_i is the phase measured at quadrant i, and

$$\kappa^{DWS} \approx \frac{d}{\lambda} = 1.9 \, \text{krad/rad} \tag{1.16}$$

is the calibration factor of the DWS measurement to real test mass angle, e.g., for a beam diameter $d \approx 2 \, \text{mm}$ and a laser wavelength $\lambda = 1064 \, \text{nm}$.

However, in the implementations presented in Parts iii and iv, this computation has been slightly modified in order to avoid phase-jump problems and

take into account the signal-to-noise ratio (SNR): assuming one of the beams is strongly deviated from the photodetector center to its left side (A and B), Equations 1.15 would equally weight the more noisy phases (B and D), even though the SNR in that half of the detector would be significantly lower. In order to account for this, it is possible to express the signal $\zeta_i(\phi)$ measured at each quadrant as

$$\zeta_i(\phi) = \alpha_i\, e^{i\phi_i},\tag{1.17}$$

where α_i is the total amplitude of the signal at quadrant i. Hence, the angular orientation of the test mass can be recomputed as

$$
\begin{aligned}
\varphi^{DWS} &= \arg\left(\frac{\zeta_A(\phi)+\zeta_C(\phi)}{\zeta_B(\phi)+\zeta_D(\phi)}\right)\kappa^{DWS},\\[2ex]
\eta^{DWS} &= \arg\left(\frac{\zeta_A(\phi)+\zeta_B(\phi)}{\zeta_C(\phi)+\zeta_D(\phi)}\right)\kappa^{DWS},
\end{aligned}
\tag{1.18}
$$

which mathematically yields Equation 1.15 but additionally considers the relative amplitudes α_i for a proper weighting of the signals $\zeta_i(\phi)$ at each individual quadrant.

As mentioned above, this technique measures the difference in geometry of the two interfering wavefronts with a low but sufficient spatial resolution for this application. However, it is often required to measured the wavefront geometry with much higher resolution, for example, in the characterization of laser beams, or precision measurement of optical components and surfaces. An optical metrology instrument capable of performing these measurements in real-time is shortly introduced in Chapter 2.

2

HIGH-RESOLUTION DIFFERENTIAL WAVEFRONT
DETECTION

In most precision optical metrology applications, an adequate design and preparation of the laser beam is required. Irregularities and distortions in the geometry of the beam and other spatial effects of real optical components can have a considerable impact on the performance of the instrument.

An instrument capable of measuring in real-time the difference in geometry between two interfering wavefronts with high spatial resolution [9, 10], has been developed and applied[1] in the design, manufacture and characterization of various parts of the LTP optical metrology, as presented in detail in Section 9.1.

2.1 MEASUREMENT PRINCIPLE

The relative geometry of two interfering beams can be measured in the real-time interference pattern using a charge-coupled device (CCD) camera and pixelwise data processing.

Several mathematical approaches [11] can be used to obtain the phase of a sinusoid from a measured time-domain representation as given by Equation 1.11, which are based on measuring n equidistant intensity samples $I_k = I(t_k)$, with $t_k = k\,\Delta t$, where k is an integer. The approach chosen for this instrument is a 4-point algorithm [12], corresponding to a straightforward Discrete Fourier Transform (DFT) of the signal with $n = 4$ samples and $\Delta t = T/4$, where $T = 1/f$ is the period of the signal.

---

1 This instrument was developed by the author in his Master's thesis. However, detail functional and noise behavior characterization, and application of the instrument were subject of the research activities of this doctoral thesis.

In the ideal case of a noise-free signal, these intensities would be given by

$$I_k = I_{avg} \left[1 + C \cos \left(\varphi + k \frac{\pi}{2} \right) \right], \tag{2.1}$$

where I_{avg} is the average of the sampled intensities.

The phase at the pixel γ, φ_γ, can be calculated from these intensity samples $\left(I_0^{(\gamma)} \ldots I_3^{(\gamma)} \right)$ with the 4-point algorithm as

$$\varphi_\gamma = \arctan \left(\frac{I_3^{(\gamma)} - I_1^{(\gamma)}}{I_0^{(\gamma)} - I_2^{(\gamma)}} \right). \tag{2.2}$$

Additional useful data can also be obtained from these 4 intensity samples. Using the abbreviations

$$a_\gamma = I_0^{(\gamma)} - I_2^{(\gamma)} \tag{2.3}$$

$$b_\gamma = I_3^{(\gamma)} - I_1^{(\gamma)} \tag{2.4}$$

$$d_\gamma = I_0^{(\gamma)} + I_1^{(\gamma)} + I_2^{(\gamma)} + I_3^{(\gamma)}, \tag{2.5}$$

it yields:

- Contrast at the pixel γ:

$$C_\gamma = 2 \cdot \frac{\sqrt{a_\gamma^2 + b_\gamma^2}}{d_\gamma} \tag{2.6}$$

- Total phase over the CCD surface:

$$\varphi_{total} = \arctan \left(\frac{\sum_\gamma b_\gamma}{\sum_\gamma a_\gamma} \right) \tag{2.7}$$

- Total contrast over the CCD surface:

$$C_{total} = 2 \cdot \frac{\sqrt{\left(\sum_\gamma a_\gamma \right)^2 + \left(\sum_\gamma b_\gamma \right)^2}}{\sum_\gamma d_\gamma} \tag{2.8}$$

- Average intensity at the pixel γ:

$$I_{avg}^{(\gamma)} = \frac{d_\gamma}{4} \tag{2.9}$$

- The maximum and minimum intensity for the set of exposures ($I_0 \ldots I_3$) can also be determined for diagnostic purposes.

Furthermore, an exposure of the dark fringe can be directly captured by triggering the CCD camera with the appropriate delay τ_{df}:

$$\tau_{df} = \frac{3\pi/2 - \varphi_{total}}{2\pi} \, T_{het}. \tag{2.10}$$

The instrument consists of a Indium Gallium Arsenide (InGaAs) CCD camera with a 12-bit analog-to-digital converter (ADC) that is placed at one output port the a heterodyne interferometer and is triggered by the timing control electronics residing in a FPGA, which uses as reference the signal of a single-element photodiode at the second interferometer output.

The experimental setup is outlined in Figure 8.
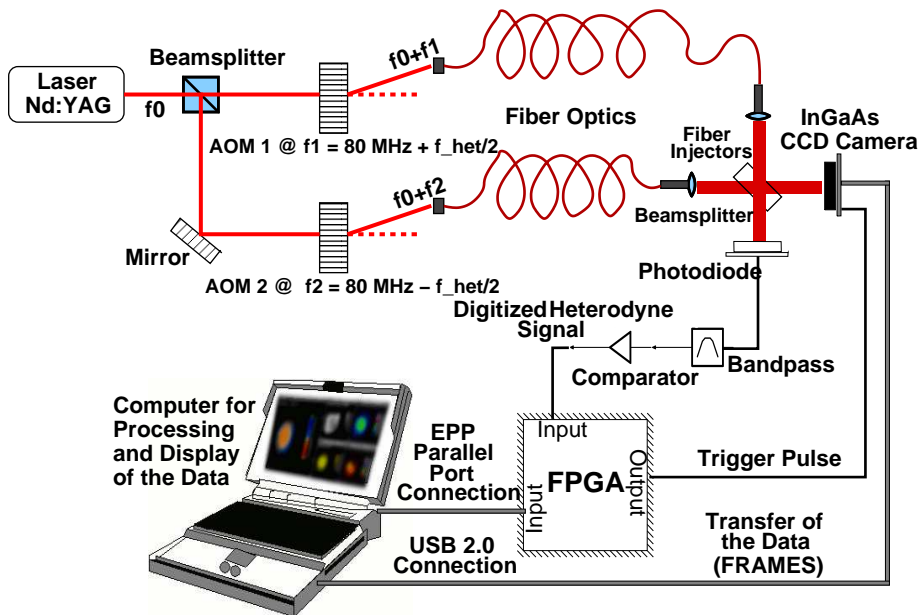
Figure 8: Experimental setup used for the phasemeter.

2.1.1 *Data display*

A graphical user interface (GUI) was developed to display the measured data in real-time (see Figure 9(a)) at a rate of approximately 5 to 6 data updates per second. This enables online adjustment of the optical setup according to the feedback information delivered by the instrument. Five different data displays have been included in the GUI. The corresponding information is also additionally plotted in Figure 9.
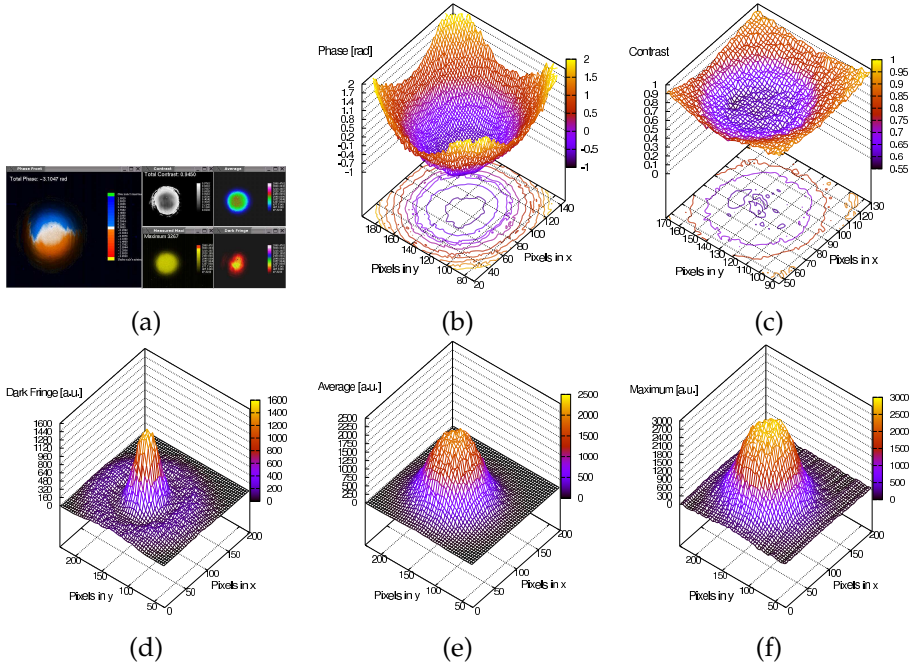
Figure 9: (a) Graphical User Interface programmed to display the measured data in real-time. (b) Spatial distribution of the phase. (c) Spatial distribution of the contrast. (d) Exposure of a dark fringe. (e) Average intensity over four exposures. (f) Maximum intensity over four exposures.

2.1.2 *Noise level measurement*

In order to measure the noise level of the instrument, the camera was illuminated with a spatially homogeneous light source (an array of infrared LED's behind a matt glass window), whose intensity was sinusoidally modulated. A rms phase error of 2.96 mrad was obtained over the CCD area of observation. According to Equation (1.9), this value corresponds to a rms spatial resolution ΔL of about 500 pm with a wavelength $\lambda = 1064$ nm for the neodymium-doped yttrium aluminium garnet (Nd:YAG) laser source employed.

As it can be seen in Equation (2.2), one noise source of the phase measurement is the fluctuation of the sampled intensities. The rms error of the phase, $\Delta\varphi_{rms}$, induced by intensity fluctuations ΔI_{rms} can be estimated from Equation (2.2) as:

$$\Delta\varphi_{rms} = \sqrt{\sum_k \left(\frac{\partial\varphi}{\partial I_k}\right)^2 \Delta I_{rms}} \tag{2.11}$$

$$= \sqrt{\frac{2}{(I_0 - I_2)^2 + (I_1 - I_3)^2} \Delta I_{rms}}.$$

After simplifying Equation (2.12) by using Equation (2.1), it can be obtained that:

$$\Delta\varphi_{rms} = \frac{\sqrt{2}}{C} \frac{\Delta I_{rms}}{I_{avg}}. \tag{2.12}$$

The following three error sources were identified, and their noise contribution to the phase measurement was estimated:

1. Laser power fluctuations: An Allan deviation of 8.6×10^{-4} was measured at an averaging time of 33 ms, which corresponds to the sampling period of the CCD camera (30 fps), yielding a phase error of 1.22 mrad from Equation (2.12).

2. ADC digital noise of the camera: A rms intensity error of four quantization units was measured by constant and spatially homogeneous illumination of the CCD camera. The pixelwise rms variation and an average over the CCD surface were then computed. This value corresponds to relative intensity fluctuations of the order of 9.76×10^{-4}, which translates (by using Equation (2.12)) into a phase error of 1.38 mrad.

3. Time jitter: There are at least three sources of jitter. Firstly, the synchroniza-tion delay of the comparator output with respect to the 10 MHz clock of the FPGA, which is uniformly distributed between 0 and 100 ns. Secondly, a similar delay between the FPGA clock and the CCD internal clock, which is also at 10 MHz but unsynchronized, and thirdly other jitter effects. A phase error of 0.99 mrad was obtained by simulating the first and second effects in software, using two independent random delays uniformly distributed.

Table 1 summarizes the noise contributions identified for the spatially resolving phase measurement.

Table 1: Main noise sources of the wavefront measurement.

Noise Source	RMS Error
Laser power fluctuations	1.22 mrad
ADC digital noise of the camera	1.38 mrad
Time jitter	0.99 mrad
Total contribution	**2.09 mrad**
Noise level measured	**2.96 mrad**

2.1.3 Functional testing

A series of measurements were conducted at a table-top interferometer shown in Figure 8 with the aim of intentionally change the curvature of one of the interfering wavefronts in order to measure it with the wavefront detector. Since the two interfering wavefronts are initially similar, a lens was introduced into the path of one beam, between the corresponding fiber injector and the beam combiner (see Figure 10).

The results of these measurements are shown in Figure 11: (a) $f = +500$ mm, (b) $f = -500$ mm, and (c) cylindrical lens with $f = +80$ mm.

A two-dimensional phase unwrapping algorithm [13, 14, 15] was developed and was used for data post-processing.

A further test was done on a table-top interferometer in order to adjust the lenses of two commercial fiber injectors by using this instrument. The aim of
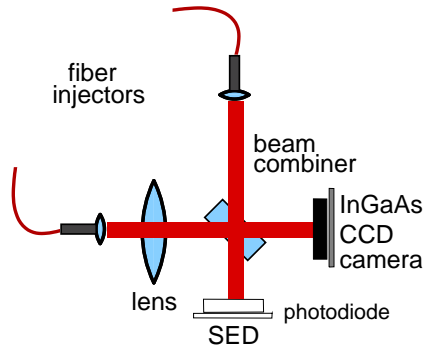
Figure 10: Experimental setup with an additional lens in the path of one beam to intentionally change the curvature of its wavefront.

(a) (b) (c)
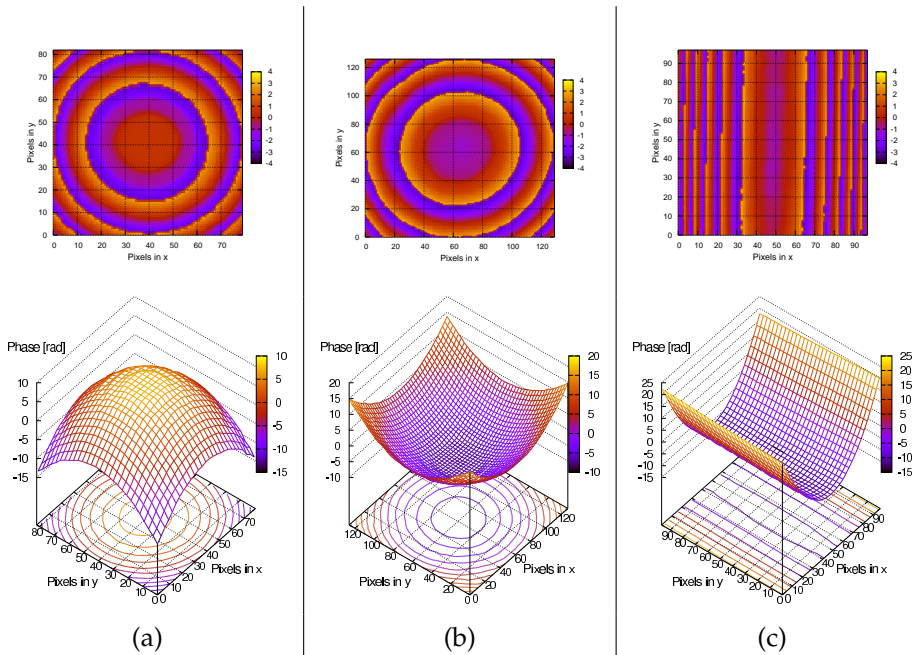
Figure 11: (a) Wrapped and unwrapped wavefront measured with a lens $f = +500\,\text{mm}$ in one arm of the interferometer. (b) Wrapped and unwrapped wavefront measured with a lens $f = -500\,\text{mm}$. (c) Wrapped and unwrapped wavefront measured with a cylindrical lens $f = +80\,\text{mm}$.

25
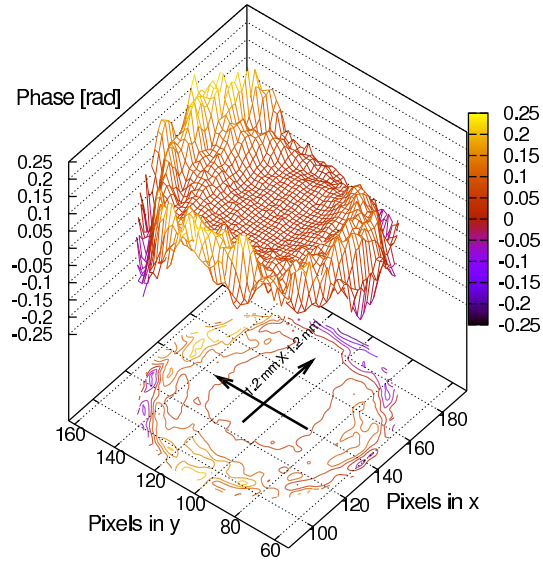
Figure 12: Adjusted phasefront measured on a table-top Mach-Zehnder interferometer.

this experiment was to match the parameters of the interfering beams and to obtain a homogeneous flat phasefront. The result of this experiment is shown in Figure 12.

It can be seen that over a surface of approximately $1.2\,\text{mm} \times 1.2\,\text{mm}$ (that corresponds to an area of 40×40 pixels for a 30 μm pixel pitch) the phasefront shows a reasonably homogeneous spatial profile. A circular section of approximately 1 mm diameter at the beam center was analyzed, obtaining a standard deviation of approximately 3.49 mrad, which is very close to the measured sensitivity of the instrument. This value corresponds to a spatial resolution of 590 pm.

Similar measurements have been performed at the LTP quasi-monolithic fiber injectors in order to characterize the wavefront the beams obtained. This instrument can also be applied in the characterization of optical components, as it has been done with the LTP optical window. These investigations are presented in Section 9.1.

Part II

POINT-AHEAD ANGLE MECHANISM

3
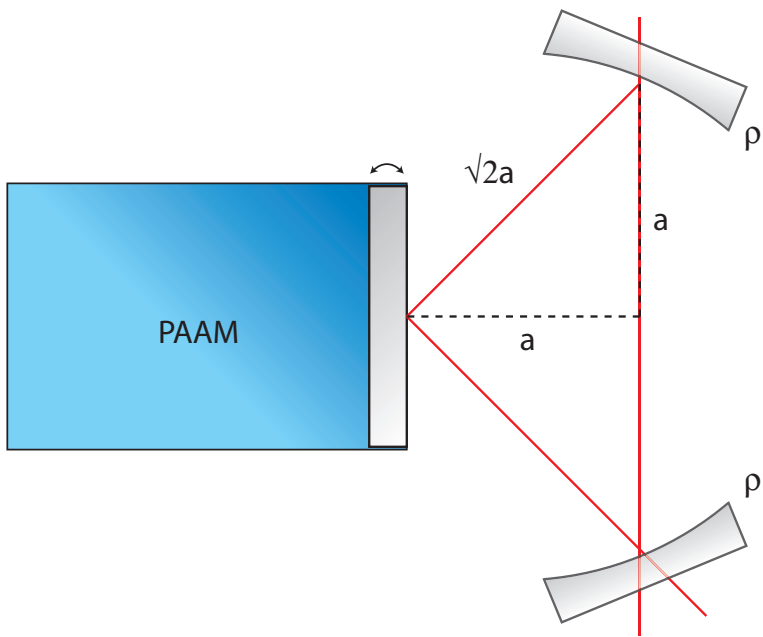
ORIGIN AND VERIFICATION METHOD

3.1 POINT-AHEAD ANGLE IN LISA

LISA consists of a constellation of three spacecraft in an equilateral triangle formation with an armlength of 5 million kilometers. The armlength varies by approximately 1% (50 000 km) over one year, due to celestial dynamics of the individual orbits. The rotation of the triangle combined with the finite speed of light, induces a non-zero angle [16] between the optical axes of the incoming beam that eventually reaches the remote spacecraft.

The orbits of the spacecraft have been analyzed [17] in order to estimate the variations of this *point-ahead* angle that arise from orbital dynamics. The results of this analysis showed an almost constant in-plane angle of approximately 3.3 μrad with variations of approximately 100 nrad (see Figure 13 [17]).

The variations of the out-of-plane angle, shown in Figure 14 [17], are much larger at 12 μrad (peak-to-peak) over one year orbital period, and correspond to a pointing effect of the output beam of the order of 60 km over the 5×10^9 m armlength. This would prevent the beam from reaching the remote spacecraft and must therefore be actively corrected by a mechanism at the emitter.

The PAAM is placed directly in the optical path of the transmit beam, and must be stable enough to avoid excess phase noise in the gravitational wave measurement. The longitudinal stability required for this device is 1.4 pm/$\sqrt{\text{Hz}}$ above 2.3 mHz and relaxes to lower frequencies, as shown in Figure 15 [18].

In order to verify this longitudinal stability for prototype PAAM devices, an appropriate optical metrology system has been developed at AEI based on the
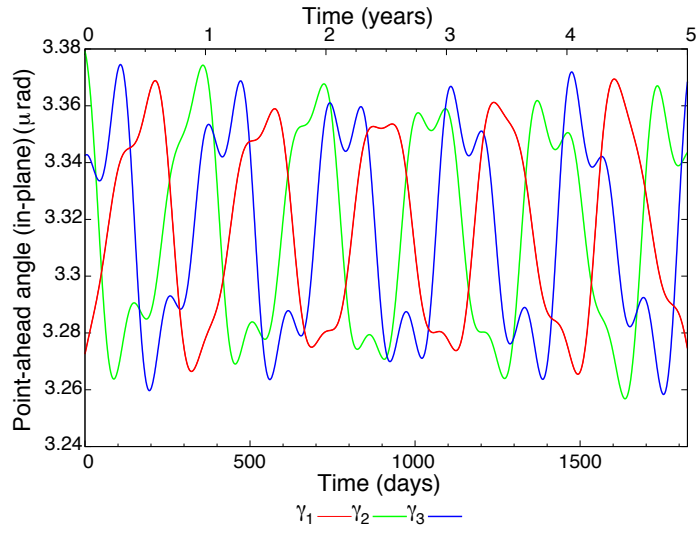
Figure 13: Estimated fluctuations of the in-plane point-ahead angle.
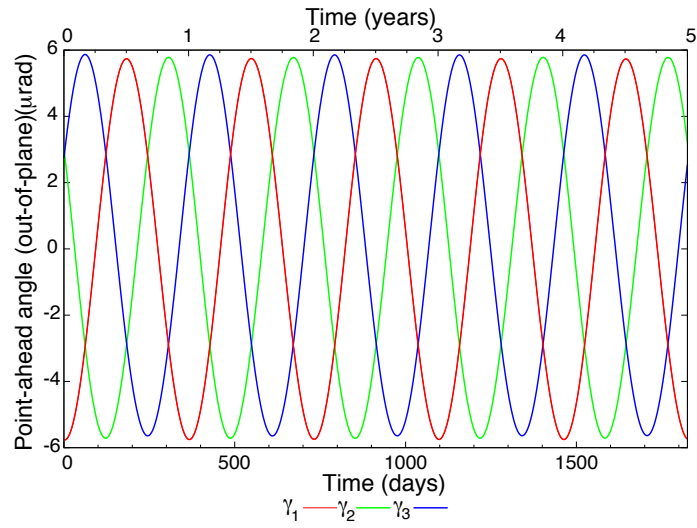
Figure 14: Estimated fluctuations of the out-of-plane point-ahead angle.
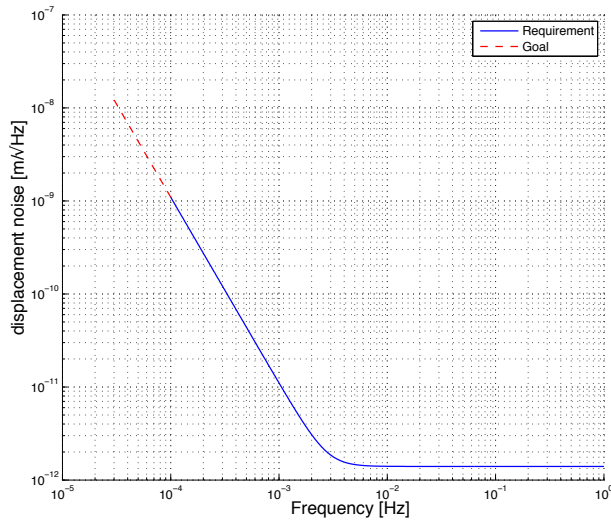
Figure 15: Required longitudinal stability for the point-ahead angle mechanism.

frequency readout of a laser that is stabilized to the length of a reference cavity[1].

The design of this optical system is presented in the Section 3.2.

3.2 OPTICAL METROLOGY CONCEPT

The required stability of $1.4\,\mathrm{pm}/\sqrt{\mathrm{Hz}}$ at millihertz frequencies demands a highly sensitive and stable optical setup. Interferometer systems developed for similar applications, consisting of phase modulated homodyne interferometers and optical heterodyne detection, have demonstrated sensitivities to the level of few picometers in this frequency band, which is not sufficient in this case. Developments and investigations on these other techniques are presented in Parts iii and iv.

Hence, the chosen optical metrology concept is based on the frequency stabilization of a laser to a resonant cavity that contains the PAAM within its optical path. The mechanical stability of the PAAM is measured by monitoring the laser

---

1 This work was done together with Benjamin Sheard, who is the leading scientist of this project in the AEI LISA Group.

frequency fluctuations $\delta\nu$ that are proportional to changes δL of the cavity length L as

$$\delta L = \frac{L}{\nu}\delta\nu, \tag{3.1}$$

where ν is the resonance frequency, as described in Section 1.1.1.

The current baseline design of the LISA optical bench defines an angle of incidence of 45° of the laser beam onto the PAAM. In order to verify the stability of the PAAM under this condition, typical linear cavities cannot be used. In addition, the mirror mounted on the PAAM has been defined to be flat, which requires at least one additional mirror to be curved in order to obtain a stable eigenmode.

After some design trade-offs, a triangular cavity of L = 14.5 cm round trip length, with two concave mirrors (radius of curvature of 500 mm) attached to an ultra-stable optical bench made of Zerodur® by using hydroxide-catalysis bonding [19], was chosen as baseline configuration [20]. The low coefficient of thermal expansion (CTE) of Zerodur® of the order of 10^{-7}/K together with the bonding technique of the mirrors provide a high thermal and mechanical stability. The third cavity mirror is attached on the PAAM, as shown in Figure 16.

Since fluctuations of the laser frequency depend on the length changes of the total cavity, the optical assembly is required to be stable enough in order to detect variations of the PAAM only. Defining a safety margin of a factor 10 for thermal induced length changes $\delta L = 0.14$ pm/$\sqrt{\text{Hz}}$, and given the CTE of Zerodur® together with the nominal designed cavity length, a requirement on the maximum thermal fluctuations δT allowed for the optical bench environment can be computed as

$$\delta T = \frac{\delta L}{L\,\text{CTE}} = \frac{0.14\,\text{pm}/\sqrt{\text{Hz}}}{14.5\,\text{cm}\,10^{-7}/\text{K}} = 9.6\,\mu\text{K}/\sqrt{\text{Hz}} \approx 10^{-5}\,\text{K}/\sqrt{\text{Hz}}. \tag{3.2}$$

In order to measure length fluctuations better than 1.4 pm/$\sqrt{\text{Hz}}$, according to Equation 3.1, the frequency fluctuations for a typical Nd:YAG laser ($\lambda = 1064$ nm $\Rightarrow \nu = 2.82 \times 10^{14}$ Hz) would be of the order of

$$\delta\nu = \frac{1.4\,\text{pm}/\sqrt{\text{Hz}}}{14.5\,\text{cm}}\,2.82 \times 10^{14}\,\text{Hz} = 2.7\,\text{kHz}/\sqrt{\text{Hz}}.$$

It is not physically possible to directly measure the frequency of the electric field of a laser beam, and thus, neither its fluctuations. Therefore, an optical
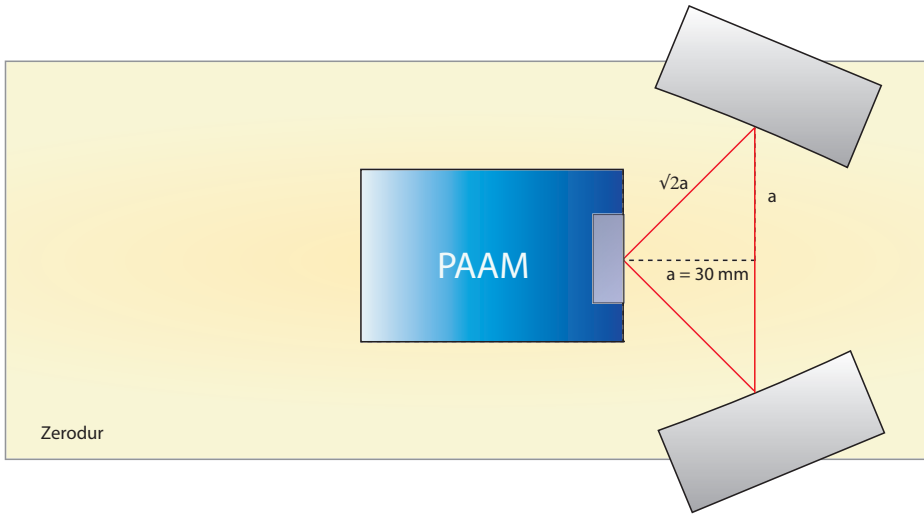
Figure 16: Design of the PAAM cavity optical bench.

down mix process of this signal is conducted by interfering this measurement electric field ("meas") with a local oscillator ("LO") that is a reference laser beam stabilized to a different reference cavity of length L_{LO}, whose frequency stability is sufficiently high. The resulting frequency of the beat note signal "bn" from the optical heterodyne interference (as explained in Section 1.1.2) can be expressed as the difference between the interfering beams (LO-meas)

$$\nu_{bn} = \nu_{LO} - \nu_{meas}. \tag{3.3}$$

Assuming uncorrelated fluctuations of the beams, the beat note fluctuations can be expressed as

$$\delta\nu_{bn} = \sqrt{\delta\nu_{LO}^2 + \delta\nu_{meas}^2} \ . \tag{3.4}$$

By substituting Equation 3.1 into Equation 3.4 for the individual frequency fluctuations $\delta\nu_{LO/meas}$, it yields

$$\delta\nu_{bn} = \sqrt{\left(\nu_{LO}\frac{\delta L_{LO}}{L_{LO}}\right)^2 + \left(\nu_{meas}\frac{\delta L_{meas}}{L_{meas}}\right)^2}, \tag{3.5}$$

33

where the fundamental laser beam frequencies (not their fluctuations) can be assumed as equal $\nu_{LO} = \nu_{meas} = \nu$ for the case of similar laser systems (Nd:YAG: $\lambda = 1064\,\text{nm}$). Hence, the beat note fluctuations can be computed as

$$\delta\nu_{bn} = \nu \sqrt{\left(\frac{\delta L_{LO}}{L_{LO}}\right)^2 + \left(\frac{\delta L_{meas}}{L_{meas}}\right)^2} \,. \tag{3.6}$$

A test facility has been set up in order to conduct the measurement of beat note fluctuations at the cavity designed for the PAAM stability verification. Chapter 4 presents a detailed description of this laboratory setup.

TEST FACILITY

A laboratory testbed has been setup for optical length measurements at the level of $1.4\,\mathrm{pm}/\sqrt{\mathrm{Hz}}$ at millihertz frequencies in order to assess the stability of prototypes of the LISA point-ahead angle mechanism (PAAM).

The testbed consists of two Nd:YAG laser systems, each stabilized in its frequency to a corresponding reference cavity operated in a vacuum chamber.

The two laser beams are recombined at a beamsplitter (as in Figure 5) in order to readout the fluctuations of the resulting beat note from the interference of the beams at a photodetector that is read out by a commercial frequency counter[1].

Characterization of the testbed and first length measurements[2] conducted at this optical setup are presented.

4.1 REFERENCE SYSTEM

A laser system with sufficient frequency stability is required to provide a beam as local oscillator for the beat note measurement. This reference system [5, 21] has been available at the AEI laboratories for several years and consists of a 21 cm linear cavity made of ultra-low expansion (ULE)$^{\circledR}$ glass, operated in a vacuum chamber at a typical pressure of 10^{-7} mbar. The laser frequency is stabilized to the resonance frequency of the cavity by applying the Pound-Drever-Hall (PDH) technique [22] to obtain an zero-crossing error signal. The phase of the laser beam is modulated at a frequency of 12 MHz by a fiber-coupled electro-optic modulator (EOM). The sidebands imprinted on the laser beam do not match

---

1 Agilent 53131A
2 The measurements and the testbed setup have been conducted in collaboration with Benjamin Sheard as team work in the AEI LISA group.

the resonance frequency of the cavity and are thus reflected to interfere with the laser beam at a photodetector. This signal can be demodulated with the local oscillator driving the EOM in order to obtain the error signal for the laser frequency stabilization. Figure 17 shows an schematic layout of the system. In
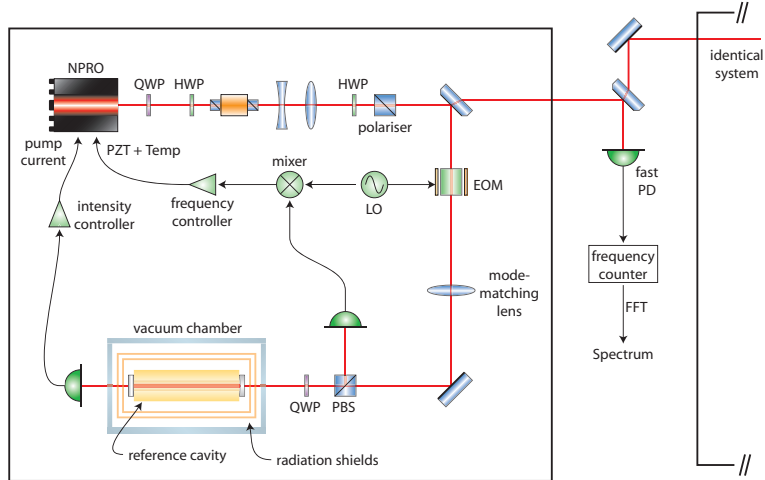
Figure 17: Schematic layout of the reference frequency system for beat note measurements.

order to measure the frequency stability of this setup, beat note measurements between two nominally identical systems were conducted [5], obtaining the result of approximately $50\,\mathrm{Hz}/\sqrt{\mathrm{Hz}}$ at $3\,\mathrm{mHz}$. Rescaled to the triangular ring cavity length designed for PAAM testing, this corresponds to length fluctuations of about $10^{-14}\,\mathrm{m}/\sqrt{\mathrm{Hz}}$, which is sufficiently stable as local oscillator reference for the measurements.

4.2 MEASUREMENT SYSTEM

The optical measurement system consists of a three mirror ring cavity with two curved mirrors rigidly attached to a Zerodur® baseplate. The third mirror is to be mounted on prototypes of the PAAM (see Figure 18).

Due to unavailability of actual PAAM prototypes at the time these first preliminary measurements were conducted, a test mount was used to fix a mirror
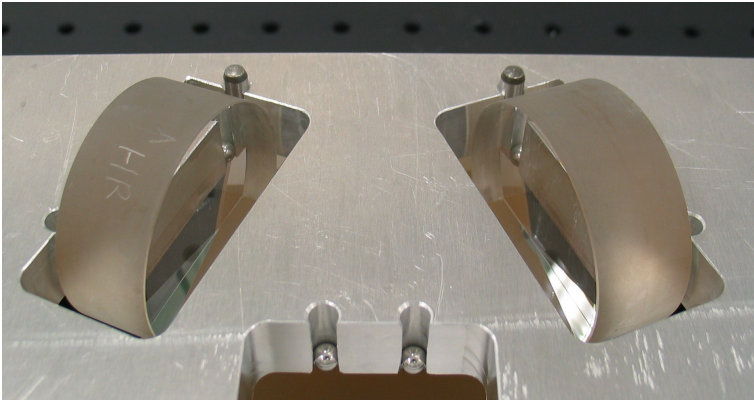
Figure 18: Photograph of the bonded curved mirrors on the baseplate.

at the nominal position on the optical bench. The test mount, as well as PAAM prototypes when available, are placed on the optical bench with a mass on top in order to prevent it from sliding on the bench. No additional attachment techniques (e.g. bonding, gluing or optical contacting) are foreseen.

Similarly to the reference system, the frequency of the measurement laser system ν_{meas} is stabilized to the triangular cavity on resonance, obtaining the error signal of the system by applying the PDH [22] technique.

The cavity resides in a vacuum chamber typically operated at a pressure of 10^{-5} mbar, which is shown in Figure 19.
A two-layer aluminum thermal shield was built and placed into the vacuum chamber to operate as a passive thermal housing isolation for the optical assembly (see Figure 20).
Viton o-rings were employed as intermediate layer between the shells of the thermal shield, and between its overlay and the inner side of the tank. This provides vibration insulation to the setup and additional thermal isolation, by avoiding direct contact of metallic surfaces with a non-thermally conductive material (the thermal conductivity of typical Viton compounds is $0.22\,\mathrm{W/m\,K}$ [23]).

A photograph of the optical bench setup inside the vacuum chamber and thermal shield is shown in Figure 21.
Temperature sensors were placed at different locations inside the vacuum tank

Figure 19: Photograph of the vacuum chamber for the PAAM test facility.
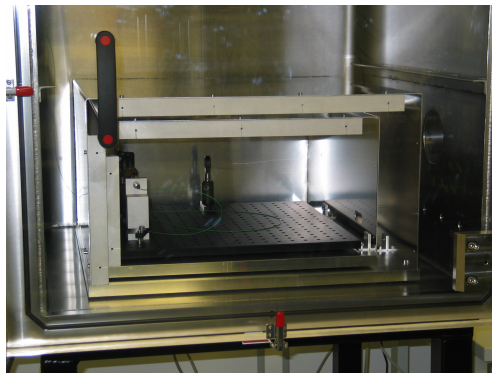
Figure 20: Photograph of the two-layer aluminum thermal shield inside the vacuum chamber.
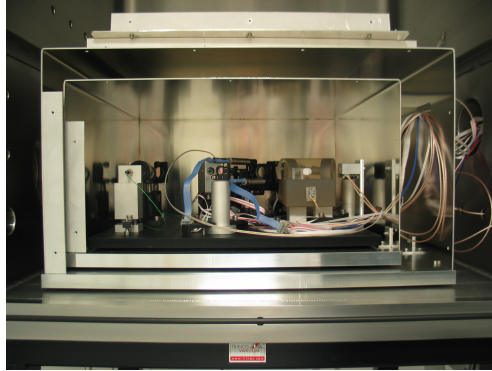
Figure 21: Photograph of optical setup inside the vacuum chamber and thermal shield in the laboratory.

and thermal shield to monitor the thermal fluctuations of the environment. In order to verify the required temperature stability of the optical setup (see Equation 3.2) a dedicated low noise 8-channel thermometer board, shown in Figure 22, based on platinum RTD sensors and a lock-in bridge readout[3] has been used to monitor the temperatures.

Figure 22: Photograph of dedicated temperature readout system.

---

3 developed by G. Heinzel

Figure 23 shows the temperature fluctuations measured from sensors placed at the inner side wall of the tank and on the aluminum breadboard inside the thermal shield.
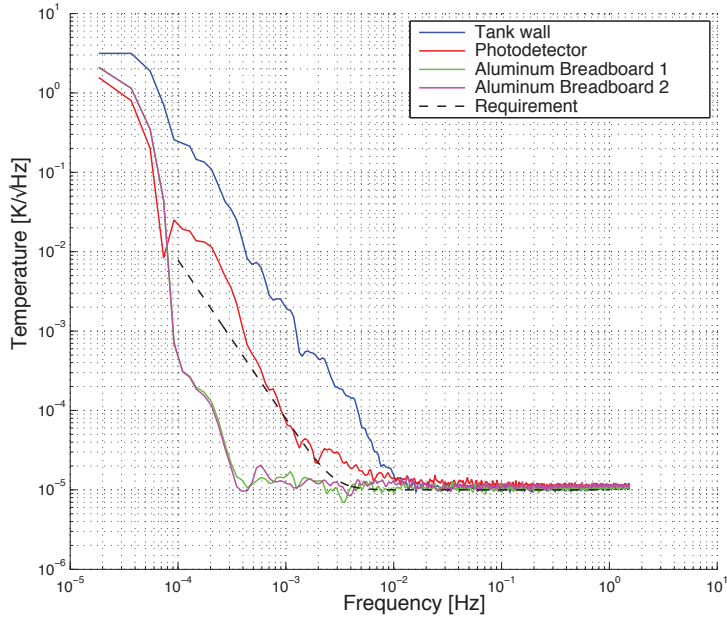
Figure 23: Temperature fluctuations measured at the inner tank wall and aluminum breadboard inside the thermal shield.

A set of temperature sensors were placed at the four lateral sides of the Zerodur® baseplate in order to directly measure temperature fluctuations at it, shown on Figure 24.

It can be seen that the required temperature stability of $10^{-5} \text{K}/\sqrt{\text{Hz}}$ in the millihertz range is achieved by the installed thermal isolation. The flat noise floor of Figure 24 at $10^{-5} \text{K}/\sqrt{\text{Hz}}$ above 6×10^{-4} Hz can be attributed to electronic noise of the readout system in accordance with theoretical models.

In order to measure the stability of the test cavity using a dummy test mirror at the location foreseen for PAAM prototypes, a beat note measurement was conducted by interfering the reference and measurement beams, each stabilized
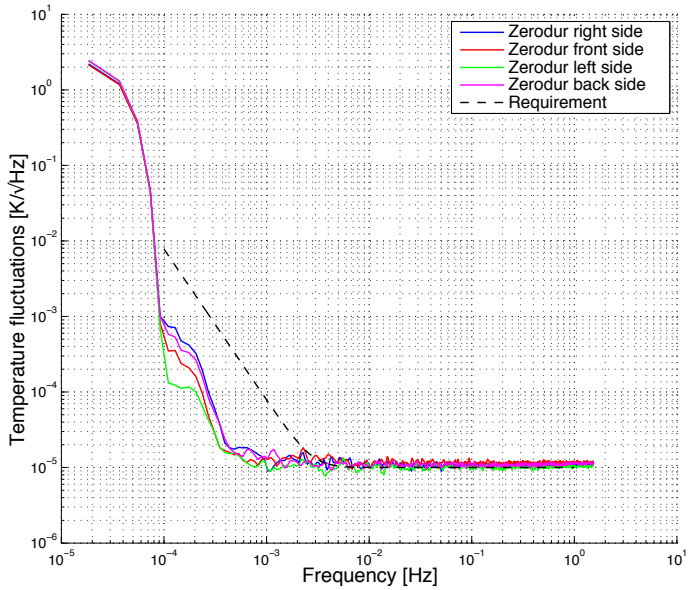
Figure 24: Temperature fluctuations measured at the lateral sides of the baseplate.
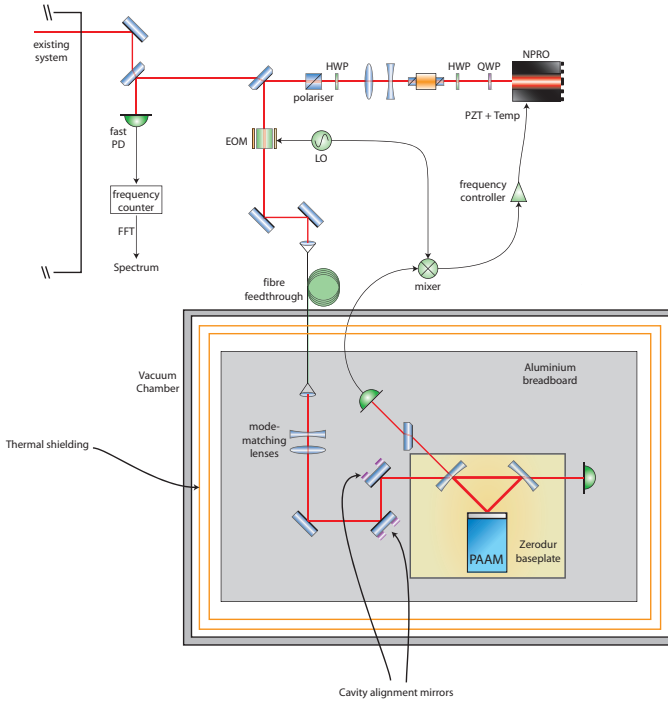
Figure 25: Schematic layout of the complete optical setup for beat note measurements.

Chapter 4

in frequency to its respective cavity. Figure 25 outlines the schematic layout of the setup for this measurement.

Figure 26 shows the beat note fluctuations measured at this test facility.
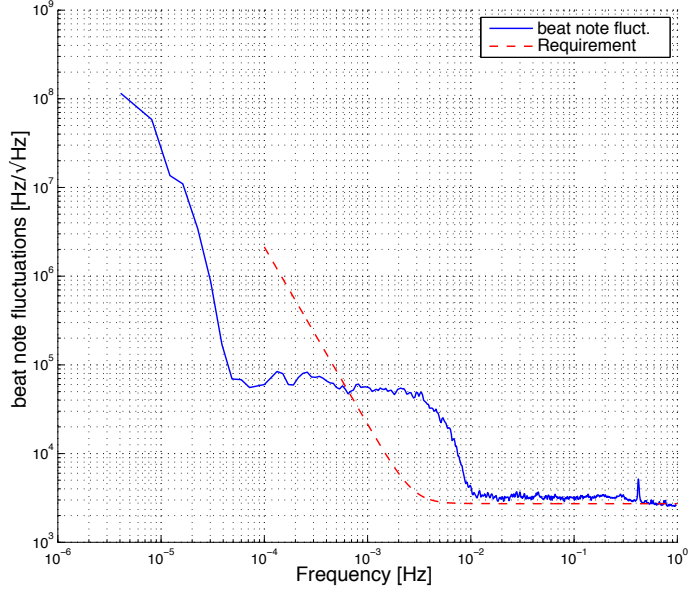
Figure 26: Measured fluctuations of the beat note.

The beat note fluctuations in the frequency range of $0.5 - 4\,\mathrm{mHz}$ are of the order of $60\,\mathrm{kHz}/\sqrt{\mathrm{Hz}}$.

By comparing this result to the measured frequency stability of the reference system ($50\,\mathrm{Hz}/\sqrt{\mathrm{Hz}}$ at $3\,\mathrm{mHz}$) which are over 3 orders of magnitude smaller, the scaling factor of length of the system that translates frequency fluctuations into cavity length variations can be obtained by simplifying Equation 3.6 in terms of the cavity length fluctuations δL_{meas} as

$$\delta L_{meas} = \frac{L_{meas}}{\nu}\,\delta\nu_{bn} = \frac{0.145\,\mathrm{m}}{284\,\mathrm{THz}}\,\delta\nu_{bn} = 5.1 \times 10^{-16}\,[\mathrm{m/Hz}]\,\delta\nu_{bn}\,. \quad (4.1)$$

The results of the beat note measurement rescaled by this factor to equivalent

pathlength fluctuations of the cavity are shown in Figure 27.
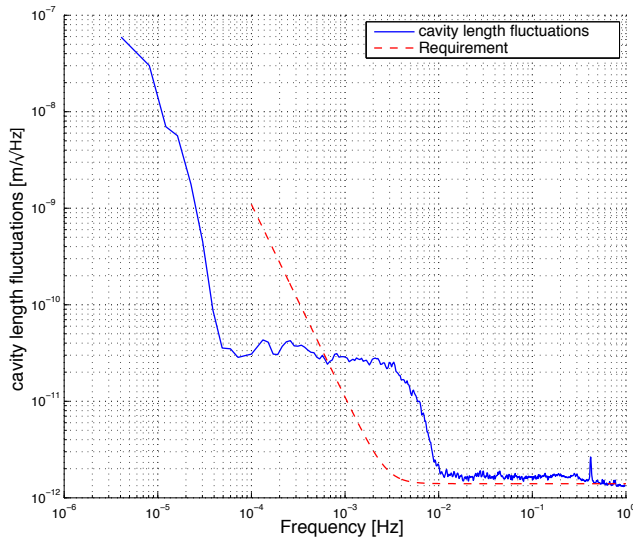
Figure 27: Equivalent cavity length fluctuations obtained from the beat note measurement.

The high frequency part above 10 mHz almost meets the requirements within an approximate factor of 1.3. Due to its flat shape and behavior over repeated observations, it has been attributed to the beat note readout instrument, which is the frequency counter. Cavity length fluctuations below 0.6 mHz, which is usually the most challenging frequency band, are well below the required sensitivity.

A candidate source of the excess noise shoulder in the frequency range of $1 - 10$ mHz has been investigated to be originated at the modulation system in charge of imprinting the sidebands on the laser beam in order to obtain the PDH error signals for the frequency stabilization.

A test run was conducted by reading out the PDH error signal and blocking the cavity during the measurement. The obtained linear spectral density (LSD) from this measurement is shown in Figure 28.
 A correlation between the spectral shapes of Figures 27 and 28 can be observed in the same frequency range. This is an indication that the source of this effect

Chapter 4
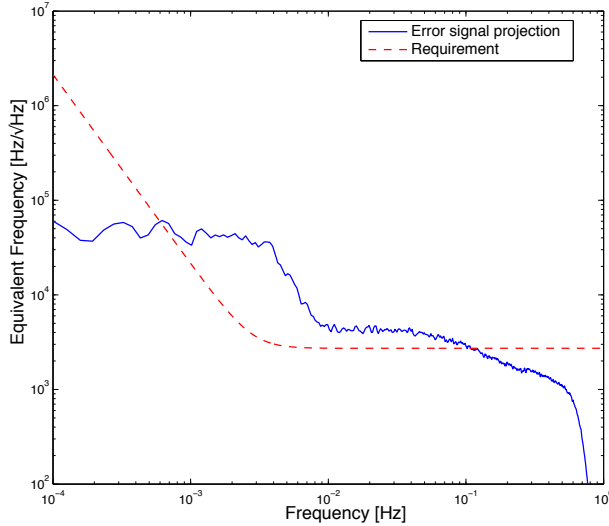
Figure 28: Readout of the error signal while the cavity was blocked.

couples into the beat note measurement through the modulation system inducing this excess noise.

It has been observed that changes of the thermal environment of the fiber-coupled modulator affects the shape of the noise contribution which points out to temperature fluctuations of the laboratory environment as the primary noise source, since the non-vacuum-compatible fiber-coupled EOM has been initially placed outside the vacuum chamber. Further investigations on this effect are necessary in order to assess temperature fluctuations as the actual noise source. Provided this is the case, it is suggested to procure a vacuum compatible fiber-coupled EOM that can be placed inside the thermal shield in order to profit from its significant thermal isolation and stability. Nevertheless, the required sensitivity of the test facility has been demonstrated at most frequencies of the LISA measurement bandwidth – $0.1 - 100\,\text{mHz}$ –, even at the usually most challenging region, and with sufficient margin below $1\,\text{mHz}$ [4].

---

4 Outside the time-scope of this thesis, further investigations on the noise behavior that eventually led to a noise floor below the requirements, have been subsequently conducted by Benjamin Sheard, utilizing a vacuum compatible fiber-coupled EOM inside the thermal shield for the modulation.

Part III

DEEP PHASE MODULATION INTERFEROMETRY
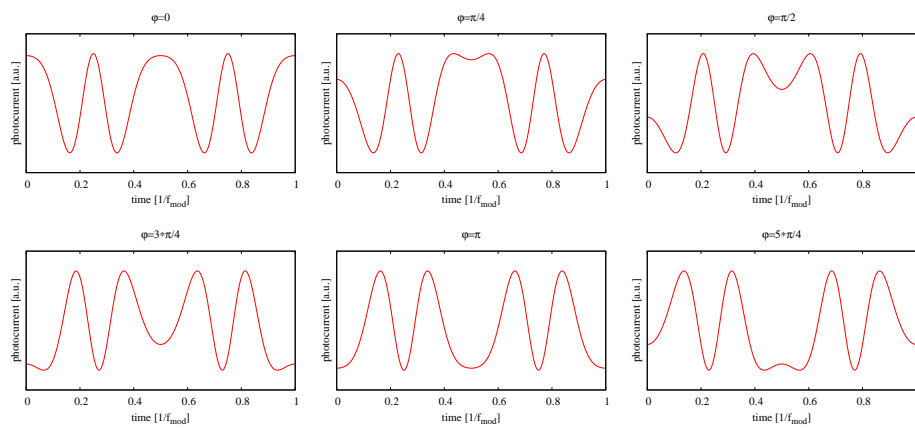
MEASUREMENT CONCEPT AND THEORY

5.1 MOTIVATION

The purpose of this research is the development of a simple and compact optical metrology system intended to improve the readout accuracy for the LISA test mass motion in their secondary degrees of freedom. The cross-coupling between geometrical degrees of freedom (seem Figure 29) in precision laser interferometric systems is a well known issue that could potentially be a performance limiting factor, especially between the optical axes **x** (longitudinal displacement) and the horizontal ϕ and vertical η angles. In the case of the LISA instrument, this cross-coupling may affect the sensitivity of the main science gravitational wave measurement. Such an effect has been studied in detail for the LTP experiment onboard the LPF satellite and is presented in Section 9.2.
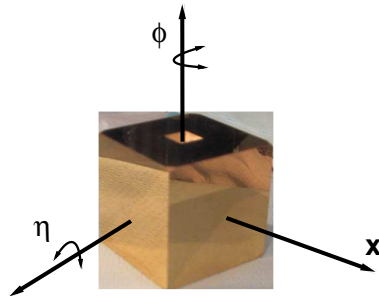
Figure 29: Test mass reference coordinate system: **x** denotes the optical axes for longitudinal test mass displacement. The horizontal and vertical test mass rotations are denoted by ϕ and η, respectively.

Chapter 5

The current baseline for LISA considers a single measurement system for these axes based on a capacitive readout. Each test mass resides in a electrode housing (EH), shown in Figure 30, which is a hollow cubical enclosure whose inner side walls consist of an array of electrodes acting as displacement sensors and actuators of the test mass.
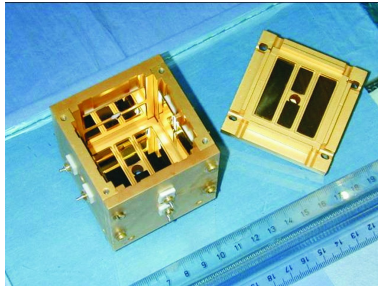
Figure 30: Photograph of a prototype electrode housing for the capacitive readout and electric actuation of the LISA test mass motion.

The test mass motion can be sensed by measuring the change in capacitance of the resulting capacitor between the EH inner side wall and the surface of the test mass. An electrostatic force can be applied to the test mass through the array of electrodes, in order to actuate its position and attitude[24]. Figure 31 shows a prototype of the current baseline design of the LISA and LISA Pathfinder test mass, which is a metal cube composed of a platinum-gold (Pt-Au) alloy of 4.3 cm side length and a mass of 2 kg. This alloy was chosen for a minimal magnetic susceptibility of the material.

The TM motion measurement accuracy achieved by the capacitive readout is of the order of $1\,\mathrm{nm}/\sqrt{\mathrm{Hz}}$ in the millihertz frequency band [25]. The investigations presented here were conducted, aiming at a measurement sensitivity better than an order of magnitude, using a compact and simple optical readout. This optical metrology system is required to faithfully monitor the test mass motion with constant high sensitivity over a wide dynamic range of about 2 mm which corresponds to many interference fringes. Hence, conventional interferometers with high accuracy, such as Fabry-Perot cavities on resonance or recycled Michelson interferometers that operate in a small fraction of a single fringe are not suitable for this application.
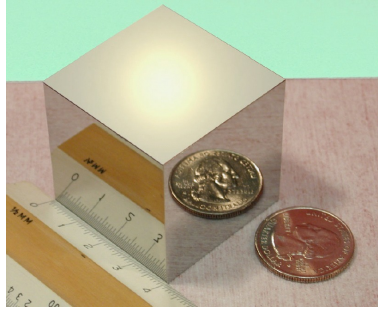
Figure 31: Photograph of a prototype test mass for LISA and LISA Pathfinder.

Various techniques are currently under investigation among the LISA community, such as a LTP-like approach with a modified optical bench reaching a sensitivity of about $300\,\mathrm{pm}/\sqrt{\mathrm{Hz}}\,@10\,\mathrm{mHz}$ [26], a compact homodyne interferometer with a sensitivity of $100\,\mathrm{pm}/\sqrt{\mathrm{Hz}}\,@10\,\mathrm{mHz}$ [27], and a robust implementation of an optical lever with a readout noise level of $100\,\mathrm{pm}/\sqrt{\mathrm{Hz}}\,@10\,\mathrm{mHz}$ [28].

A straightforward solution would be to implement an optical metrology system equivalent to the one developed for LISA Pathfinder, which is explained in detail in Part iv. However, this effort was focused on exploring different approaches, aiming at a simpler optical configuration that does not necessarily require acousto-optic modulators (AOM) for beam generation and the associated radio frequency (RF) high-voltage (HV) electronics.

The technique chosen here is based on a homodyne Mach-Zehnder interferometer with a so-called deep phase modulation that yields a wide sinusoidal phase excursion in one arm of the order of several fringes. The method was first proposed by G. Heinzel at the first LISA optical readout meeting in Hannover[29]. This technique can be considered as a generalization of the so-called "$J_1 \ldots J_4$" method [30, 31, 32] that comprehends a sinusoidal phase modulation at lower modulation depths $m \approx 1 \ldots 5$.

The results obtained from measurements conducted on a laboratory implementation for the millihertz band, showed a sensitivity of the order of $10\,\mathrm{pm}/\sqrt{\mathrm{Hz}}$ at $10\,\mathrm{mHz}$, which is comparable to the performance of the LTP interferometry and represents an improvement of the test mass readout accuracy by a factor of about two orders of magnitude in terms of capacitive sensing, and better than one

Chapter 5

order of magnitude referring to other techniques mentioned above [26, 27, 28]. In spite of the fact that the optical configuration of this system is simpler than the heterodyne approach chosen for LISA Pathfinder, it should also be mentioned that the associated data processing for interferometric phase extraction is more complex. However, depending on the application, the increase of data processing demand could be not only affordable but preferable to the implications of more complex hardware.

Besides the application on space-based gravitational wave observatories – the context within this research has been conducted – such a simple optical interferometer with sub-wavelength resolution over a wide dynamic range can be useful in many different applications like surface profiling or general metrology.

5.2 THEORETICAL BACKGROUND

The general output signal of a homodyne interferometer can be expressed as

$$V_{PD}(t) = A \left[1 - c \cos (\phi) \right], \tag{5.1}$$

where $V_{PD}(t)$ is the electrical output signal of a photodiode, ϕ is the interferometer phase proportional to the test mass motion, $c \leqslant 1$ is the contrast, and A combines nominally constant factors such as light powers and photodiode efficiencies.

In contrast to other phase modulation techniques applied in precision interferometry such as internal, external or Schnupp modulation [33] that use low modulation depths, the optical measurement concept presented here is based on the sinusoidal modulation of one arm of a homodyne Mach-Zehnder interferometer by long excursions of the phase ϕ of the order of several radians – deep phase modulation – as given by

$$\phi(t) = m \cos (\omega_m t + \psi) \tag{5.2}$$

with $m > 1$ (typically $5 < m < 20$) The signal measured at the photodetector can be mathematically expressed as

$$V_{PD}(t) = A \left[1 - c \cos (\varphi + m \cos (\omega_m t + \psi)) \right], \tag{5.3}$$

where

- φ is the main measurand; the interferometric phase which is proportional to the relative test mass position,

- A is the amplitude of the signal,

- c is the contrast or visibility of the interferometer,

- m is the modulation depth,

- $\omega_m = 2\pi f_m$ is the modulation frequency, and

- ψ is the modulation phase that is related to the difference between the modulation and sampling clocks.

Figure 32 shows typical waveforms of the photodetector signal obtained by applying this kind of modulation with various states of φ.
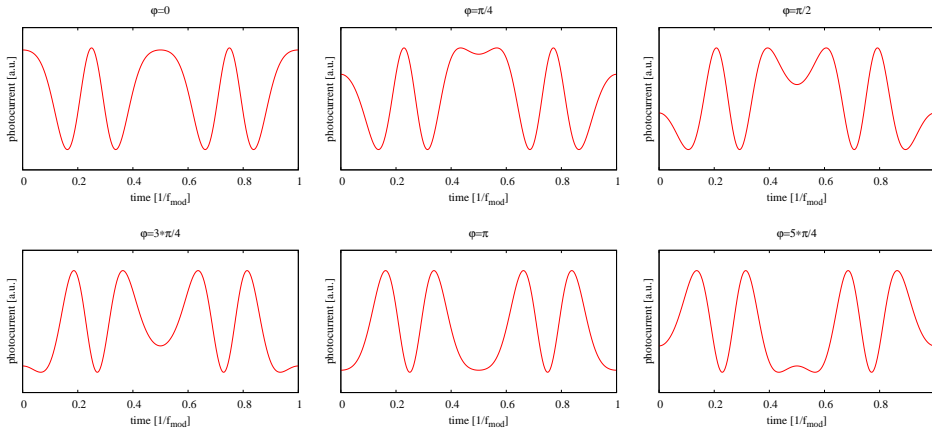
Figure 32: Waveform of the obtained interferogram for different operating points of the interferometer phase φ with a modulation depth $m = 6\,\text{rad}$.

The interferometer phase φ is the main measurand proportional to the test mass motion and is encoded in this time-dependent signal. It is possible to numerically extract it with a fit algorithm which processes the amplitude of the harmonic components that can be obtained from the spectral decomposition of the signal in terms of the Bessel functions $J_n(m)$. This is done in this method by sampling the signal and applying a Fast Fourier Transform (FFT) algorithm.

Chapter 5

5.2.1 *Spectral analysis*

Equation 5.3 can be rewritten as

$$V_{PD}(t) = \Re \left\{ A \left(1 + c e^{i\varphi} e^{im\cos(\omega_m t + \psi)} \right) \right\} \tag{5.4}$$

where the last term can be expanded in terms of the Bessel functions $J_n(m)$ as [34]

$$e^{im\cos(\omega_m t + \psi)} = J_0(m) + 2 \sum_{n=1}^{\infty} i^n J_n(m) \cos(n(\omega_m t + \psi)). \tag{5.5}$$

The signal $V_{PD}(t)$ in Equation 5.4 can be decomposed in its harmonic components as the following Fourier series

$$V_{PD}(t) = \underbrace{A \left(1 + c J_0(m) \cos \varphi \right)}_{V_{DC}(\varphi)} + \sum_{n=1}^{\infty} \underbrace{2cA \cos \left(\varphi + n\frac{\pi}{2} \right) J_n(m)}_{a_n} \cos(n(\omega_m t + \psi))$$

$$V_{PD}(t) = V_{DC}(\varphi) + \sum_{n=1}^{\infty} a_n \cos(n(\omega_m t + \psi)) \tag{5.6}$$

with

$$a_n = k J_n(m) (-1)^n \cos \left(\varphi + n\frac{\pi}{2} \right), \tag{5.7}$$

where $k = 2cA$. Figure 33 shows the dependence of the harmonic amplitudes a_n up to $n = 6$ in terms of φ.

The "$J_1 \ldots J_4$" method utilizes the harmonics a_n, typically obtained from a FFT, in order to analytically solve for the desired unknowns m and φ. The generalization of this technique yields for higher modulation depths $m \gtrsim 6$, which allows an improvement in the SNR and various consistency checks of the data, by considering the additional information contained in the harmonics a_n up to an order $n \approx m$. An overdimensioned system of equations that can be numerically solved for the four sought parameters φ, m, ψ, and the common factor k from Equation 5.7, by a least-squares algorithm. The information of the harmonic amplitude a_0, corresponding to the DC component is not considered, since it usually contains a higher noise level due to large variations in environmental and equipment conditions such as room illumination and electronic noise, among others. However, it can still be used for computation of the interferometer visibility and DC attitude measurements of the test mass, as explained is Section 1.2.
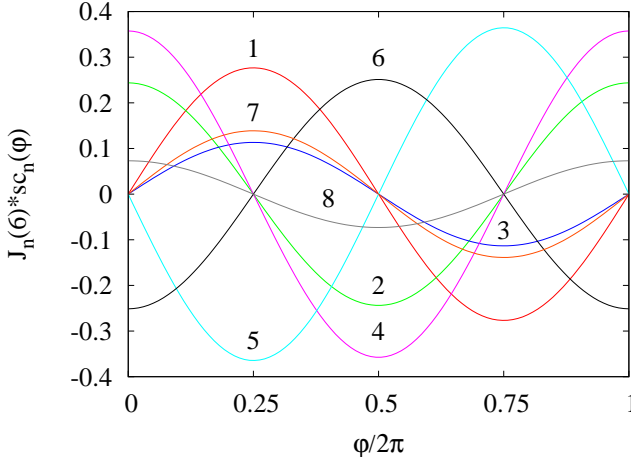
Figure 33: Dependence of the harmonics amplitudes a_n with respect to the interferometer phase φ with a modulation depth $m = 6\,\mathrm{rad}$.

5.2.2 *Fit algorithm*

The analog signal of Equation 5.3 measured at the photodetector is digitized by an ADC and split in segments of length N_{FFT} samples. Then, $N = N_{FFT}/2$ measured complex amplitudes $\tilde{c}_n$ are obtained by spectral decomposition of this time series via a FFT algorithm.

The fit algorithm aims to estimate the parameters for a minimal deviation between the measured $\tilde{c}_n$ and the complex amplitudes c_n computed from the model

$$c_n = a_n\, e^{in\psi}. \tag{5.8}$$

The four unknowns m, φ, ψ, and k can be obtained by setting up the following two separated and uncorrelated system of equations:

$$n\,\psi \;=\; \arctan\left(\frac{\mathfrak{I}\{c_n\}}{\mathfrak{R}\{c_n\}}\right),\; n = 1, 2, 3\ldots 20, \tag{5.9}$$

$$a_n \;=\; c_n\, e^{-in\psi},\; n = 1, 2, 3\ldots 20, \tag{5.10}$$

where $c_n\, e^{-in\psi}$ is a real number. However, this is not exactly the case for the measured $\tilde{c}_n\, e^{-in\psi}$, due to noise and distortions introduced by the analog

53

electronics of the data acquisition system (DAQ) that are further discussed in Section 6.2.

The solution for the four unknowns is obtained from the least-squares minimization of the expression

$$\chi^2 = \sum_{n=1}^{N} (c_n - \tilde{c}_n)^2,$$ (5.11)

where χ^2 is a four dimensional function of the parameters m, φ, ψ, and k. A modified version of the robust Nelder-Mead Simplex algorithm [35] is used as initial stage to obtain good starting values for a Levenberg-Marquardt algorithm [36, 37] that has been chosen to compute this minimization.

In order to find suitable values of the modulation index m and the number of bins N for an optimum performance of this technique, a numerical analysis of the Hessian matrix of χ^2 has been conducted [38], which is a symmetric 4×4 matrix given by

$$H = (H_{ij}) = \left(\frac{\partial^2 \chi^2}{\partial \Omega_i \partial \Omega_j} \right),$$ (5.12)

where $\Omega = \{m, \varphi, \psi, k\}$ are the four parameters.

The inverse of the Hessian matrix $H^{-1} = (\eta_{ij})$ yields information about the parameter estimates, on the variances σ^2 and correlation coefficients ρ_{ij}:

$$\sigma^2_{\Omega_i} \quad \propto \quad \eta_{ii},$$ (5.13)

$$\rho_{ij} \quad = \quad \frac{\eta_{ij}}{\sqrt{\eta_{ii}}\sqrt{\eta_{jj}}}.$$ (5.14)

An excursion of φ over the range $[0, 2\pi]$ is conducted in 64 steps by fixed N and m. The best, worst and average values of the standard deviation $\sigma_{\Omega_i}(N, m, \varphi)$ for all $\varphi \in [0, 2\pi]$ are shown in Figure 34. This excursion corresponds to an entire interferometer fringe. In order to investigate the behavior of the variance of our main measurement φ, a similar analysis is performed, assuming maximal values for the variances

$$\widehat{\sigma^2_{\Omega_i}(N, m)} = \max_{\varphi \in [0, 2\pi]} \sigma^2_{\Omega_i}(N, m, \varphi),$$ (5.15)

Figure 35 shows the maximal standard deviation $\widehat{\sigma_{\Omega_i}(N, m)}$ for some typical values of N and m.
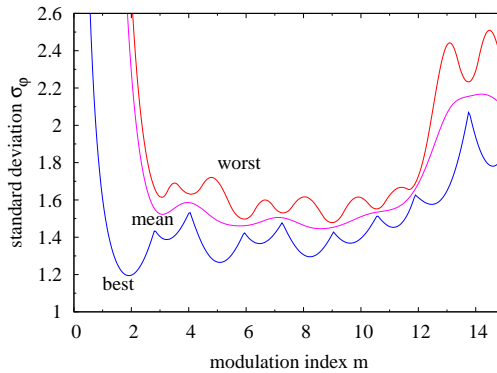
Figure 34: Ideal resolution in φ as function of the modulation index m for $N = 10$, for the best and worst φ as well as the average for all $\varphi \in [0, 2\pi]$.
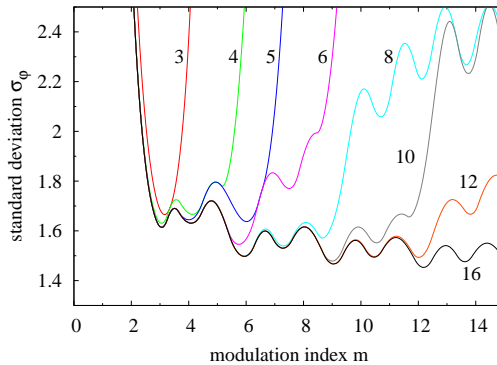
Figure 35: Ideal resolution in φ as function of the modulation index m for different orders N, for the worst value of φ at each point of each curve.

The results of this analysis show that a modulation index $3 \lesssim m \lesssim N$ provides indeed useful parameter estimates. This analysis also suggests possible best values of m for a minimal worst-case variance, as shown, for instance, in the case of $m = 6, N \geqslant 8$ and $m = 9, N \geqslant 10$, where a minimal ideal resolution of φ can be found. Nonetheless, these results can only be considered as rough guidelines, since real instrument noise has not been taken into account in this analysis. In spite of this, simulations and investigations on the laboratory prototype system shown in Chapter 6 indicate that this guideline can be taken as a good starting point.

The entire phase extraction method is illustrated in Figure 36, including the data acquisition and processing chain.
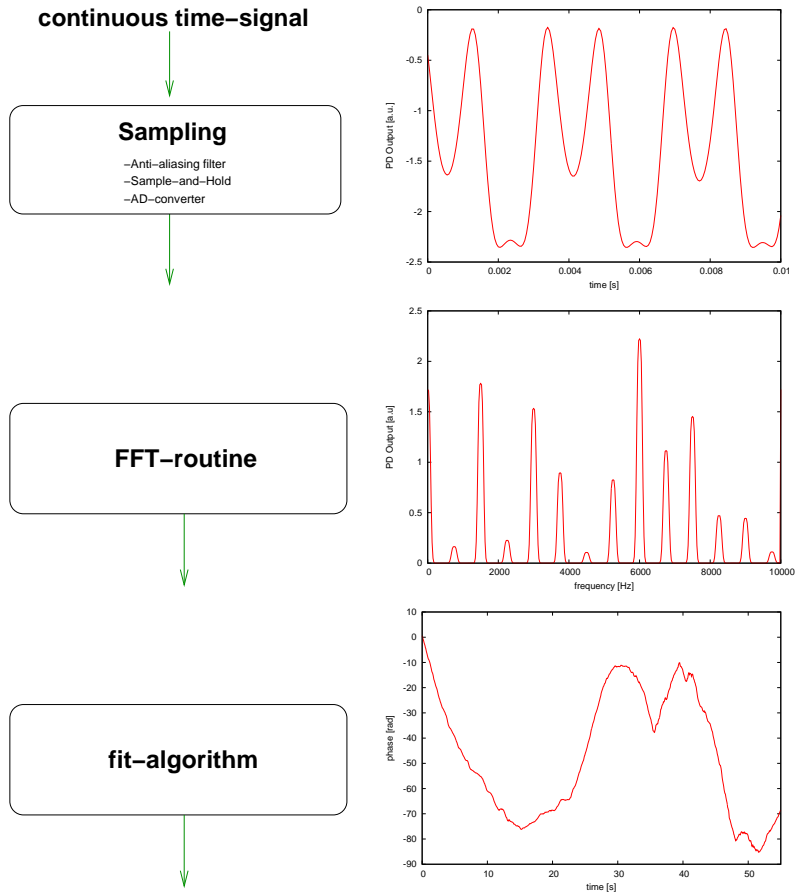
Figure 36: Data acquisition and processing chain for deep modulation phase extraction.

A prototype interferometer has been setup in the laboratory, in order to test this method with real optical signals. The definition of the setting parameters for modulation and demodulation is presented, as well as the debugging procedure and obtained test mass displacement and attitude measurements.

6

EXPERIMENTAL INVESTIGATIONS

A laboratory prototype consisting of a homodyne Mach-Zehnder interferometer was set up, in order to test the length measurement technique described in Chapter 5[1]. This implementation consists of the setup of an optical assembly for the phase modulated interferometer, the development of an appropriate real-time phase measurement system (PMS) and the associated investigation on functional operation and noise levels for an optimum performance of the system.

A piezo-electric transducer (PZT) has been chosen as phase modulator for large phase excursions of the order of several radians. Software and hardware simulations have been conducted in order to reach a better understanding of the noise sources and for better selection of the parameters for the modulation and phase measurement systems.

Measurements conducted on the engineering model of the LTP optical bench in a vacuum environment resulted in a phase readout accuracy of the order of $0.1\,\mathrm{mrad}/\sqrt{\mathrm{Hz}}$ at $10\,\mathrm{mHz}$, which corresponds to a measurement sensitivity of about $10\,\mathrm{pm}/\sqrt{\mathrm{Hz}}$ in terms of test mass displacement.

6.1 LABORATORY SETUP

6.1.1 *Optical assembly*

The optical assembly for the phase modulated interferometer was designed with a scheme similar to the LTP interferometry (presented in Chapter 7), consisting of two parts:

---

1 Part of the measurements and results presented here were obtained as team work together with A. García, G. Heinzel, J. Kullmann, and F. Wang

1. **Modulation bench**

   The the modulation bench, shown schematically in Figure 37(a), has been assembled on a aluminum breadboard using commercial optics and contains the light source and optical elements for the generation of phase modulated laser beams:

   - Laser head: The light source used is a Nd:YAG non-planar ring oscillator (NPRO) laser, emitting 300 mW at a wavelength of 1064 nm (Mephisto 500NE FC from Innolight) [39].

   - Phase modulator: Self-assembled fiber-coupled phase modulators consisting of fiber optics coiled around ring-PZTs [40] (see Figure 37(b)), are utilized for the beam generation.
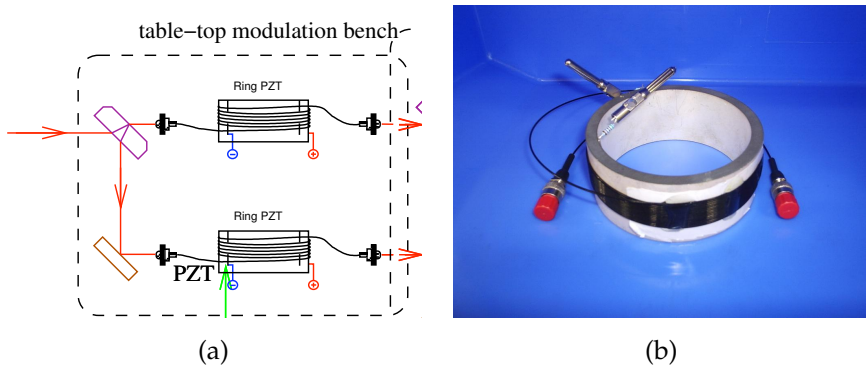
Figure 37: (a) Schematic layout of the optical modulation bench for the interferometer. (b) Self-assembled fiber-coupled phase modulators: fiber optics coiled around ring-PZTs for large phase excursions of the order of several interferometer fringes.

The main beam emerging from the laser head is split in two beams that are subsequently fiber coupled into ring-PZT phase modulators, and transferred through fiber optics to the optical bench.

In contrast to the LTP modulation bench, where both AOMs are necessary for the optical heterodyning, this configuration provides truly redundant phase modulators by including two ring-PZTs, one of which is sufficient for operation.

2. **Optical bench**

The EM of the LTP OB [41], shown in Figure 38, has been used as a very stable interferometer, in order to test the noise level of this method in a real length measurement. This optical bench consists of four non-polarizing
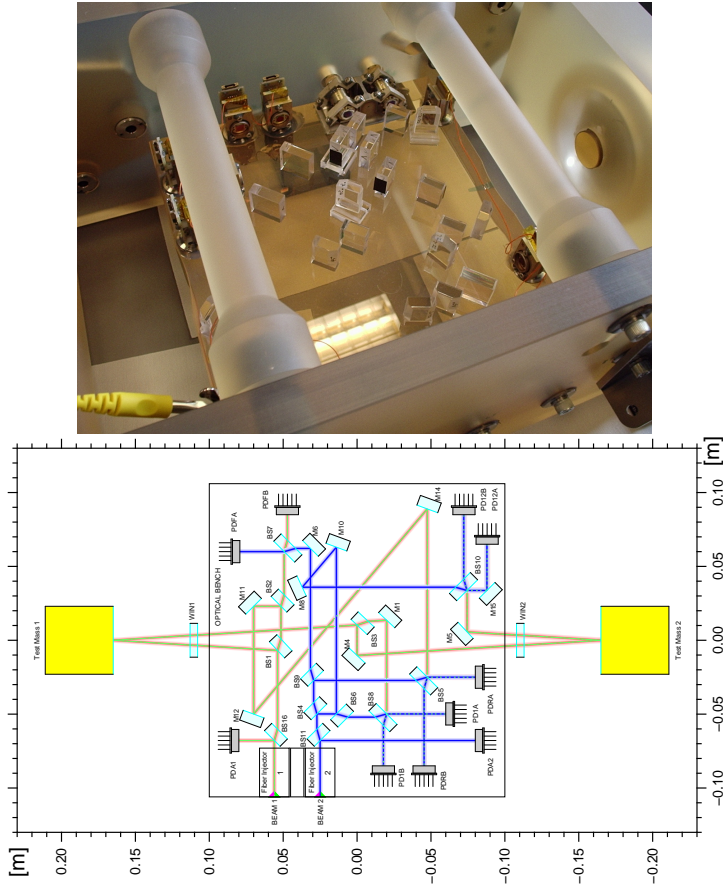
Figure 38: Photograph and schematic layout of the engineering model optical bench for LTP.

Mach-Zehnder interferometers, whose fused-silica optical components are attached onto a Zerodur® baseplate in a quasi-monolithic manner by

Chapter 6

59

hydroxide-catalysis bonding [19]. The low CTE of Zerodur® of the order of 10^{-7}/K at room temperature and the mechanical stability of the setup given by the bonding process provide a high stability optical system suitable for low-frequency precision interferometry.

The main optical length measurement is obtained by computing the difference between the phase extracted from the output of two individual interferometers on the optical bench. The interferometers chosen for the measurements are the so-called Reference interferometer that senses environmental common-mode noise, and the so-called X12 interferometer that contains two mirrors, each mounted on a 3-axes PZT as dummy test mass. The complete optical bench is discussed in detail in Part IV.

A schematic overview (only for purposes of outlining the interaction of these two parts) of the full optical system (modulation and optical benches) is depicted on Figure 39.
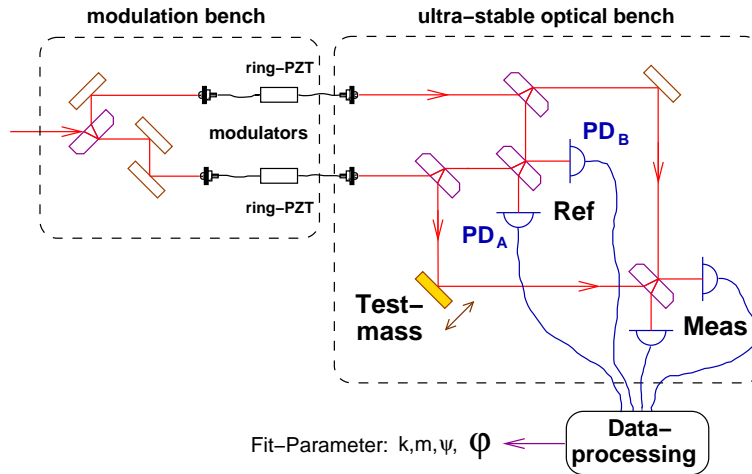
Figure 39: Schematic layout of the complete optical setup for the phase modulated interferometer.

The entire setup resides in a vacuum chamber typically operated at a pressure of the order of 10^{-3} mbar, in order to minimize effects of acoustic noise, pressure fluctuations and air currents that might otherwise perturb the optics. The vac-

uum chamber is equipped with appropriate optical and electrical feed-throughs, in order to inject the main laser beam into the modulation bench and the electric modulation signal into the PZTs, as well as to readout the photocurrents from the InGaAs photodetectors on the optical bench.

6.1.2 *Modulation and data acquisition system*

A commercial signal generator (Agilent 33220A) was used to produce the sinu-soidal modulation signal injected into one of the two ring-PZTs via a HV amplifier. This signal generator produces a 10 MHz transistor-transistor logic (TTL) output signal derived from the master clock of this direct digital synthesizer (DDS). This 10 MHz signal is used as master clock of the data acquisition system. This way, the sampling system running at a frequency f_{samp} is arranged to be coherent to the modulation signal.

The photocurrents emerging from the InGaAs quadrant photodetectors are con-verted to voltages with a low-noise transimpedance amplifier (PD-AMP). The resulting voltage signals are subsequently processed by a 9-pole Tschebyscheff anti-alasing filter (AAF) with a cut-off frequency $f_{cut} = 8$ kHz and fed into a sample-and-hold (SH) prior to being digitized by a multiplexed ADC. The si-multaneously triggered SH in each channel ensures synchronous digitization of several channels. The data acquisition board (National Instruments NI PCI-6014) installed in a standard personal computer (PC) running a Linux operating system provides 16 analog input channels – up to 10 can be used for the phasemeters – with a single sequential ADC up to 200 kSamples/s with 16-bit resolution. Fig-ure 40 shows a schematic diagram of one DAQ channel.
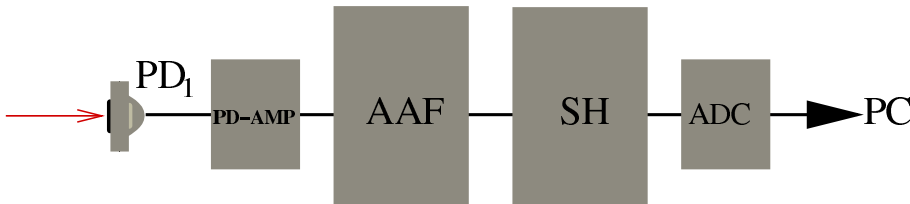
Figure 40: Diagram of a single data acquisition channel.

A self-written C program was used for

Chapter 6

1. controlling the DAQ board[2],

2. splitting the acquired time series in segments of length N_{FFT} after signal digitization,

3. processing these data segments by an efficient FFT routine (FFTW [42]), in order to obtain the measured complex amplitudes $\tilde{c}_n$ mentioned in the previous chapter,

4. applying the fit algorithm explained in Section 5.2.2 for the interferometer phase extraction, and

5. storing the data.

The entire processing time from acquiring N_{FFT} samples to computing one interferometer phase point is of the order of few milliseconds, depending on the chosen parameters.

6.1.3 *Frequency plan*

The sampling rate f_{samp} has been set to 20 kHz per channel for a maximum of 10 functional phasemeter channels.

A survey for convenient parameters was performed, in order to select adequate values to operate the phasemeter. To this end, a short C program was written to evaluate the necessary number of samples N_{FFT} according to the following mathematical relations:

$$f_\varphi \quad = \quad \frac{f_{samp}}{N_{FFT}}, \tag{6.1}$$

$$f_m \quad = \quad bin \cdot f_\varphi, \tag{6.2}$$

where the modulation frequency f_m corresponds to the bin-th frequency component of the Fourier transform, which is arranged to be coherent to the sampling frequency f_{samp} that is the N_{FFT} integer multiple of the frequency resolution, corresponding to the phase computation rate f_φ, as given by Equation 6.1.

The following boundary conditions were chosen as rough guidelines for a targeted evaluation of the N_{FFT} value over a wide range [50 . . . 10000]:

---

2 using COMEDI drivers: www.comedi.org

- The sinusoidal signal used for the phase modulation is obtained from a commercial signal generator. It should be therefore strived for a maximal distance between its frequency f_m and the multiples of the electric network frequency $f_{ENF} = 50\,Hz$, in order to avoid electric cross-talk: $\mathrm{mod}\ \left\{ \frac{f_m}{f_{ENF}} \right\} \neq 0$.

- The modulation frequency f_m has to be chosen such that the highest harmonic $N \cdot f_m$ used in the phase extraction fit algorithm, is well below the AAF cut-off frequency $f_{cut} = 8\,kHz$ to prevent loss of information: $N \cdot f_m \leqslant 4\,kHz$.

- The first useful bin of the Fourier transform – corresponding to f_m – should be far enough from the noisy DC-component for minimal spectral leakage into the harmonics of interest: $\mathrm{bin} \geqslant 10$.

The number of harmonics N to be used in the fit algorithm was set to 10 for the basic test system. From the list of possible values obtained from this survey, the parameters selected as a reasonable compromise were: $N_{FFT} = 1000$, $N = 10$, $f_m = 280\,Hz \rightarrow N \cdot f_m = 2800\,Hz$, $\mathrm{bin} = 14$, and $f_\varphi = 20\,Hz$.

6.2 PHASEMETER FUNCTIONAL AND NOISE INVESTIGATIONS

Upon setup of the data acquisition system for real-time phase measurements at 20 Hz with the parameters mentioned above, functional and noise tests were performed to assess the performance of the phasemeter.

6.2.1 *Preliminary optical testing*

A table-top experiment consisting of a Mach-Zehnder interferometer was set up for this purpose, as shown in the schematic diagram of Figure 41. The modulation signal (sine wave @ 280Hz) was applied to the ring-PZT labelled A.

The first step was a functional test of the phasemeter, in order to ensure correct interferometer phase measurements. A triangular function at a frequency of 300 mHz, coming from an additional signal generator, was injected into the spare modulator (ring-PZT B) to drive the interferometer phase. The photodetectors (RefA and RefB), placed at the two complementary output ports of the beam combiner were connected to the DAQ system as shown in Figure 40. Figure 42 presents the time series of the interferometer phase extracted from a single channel.

Chapter 6
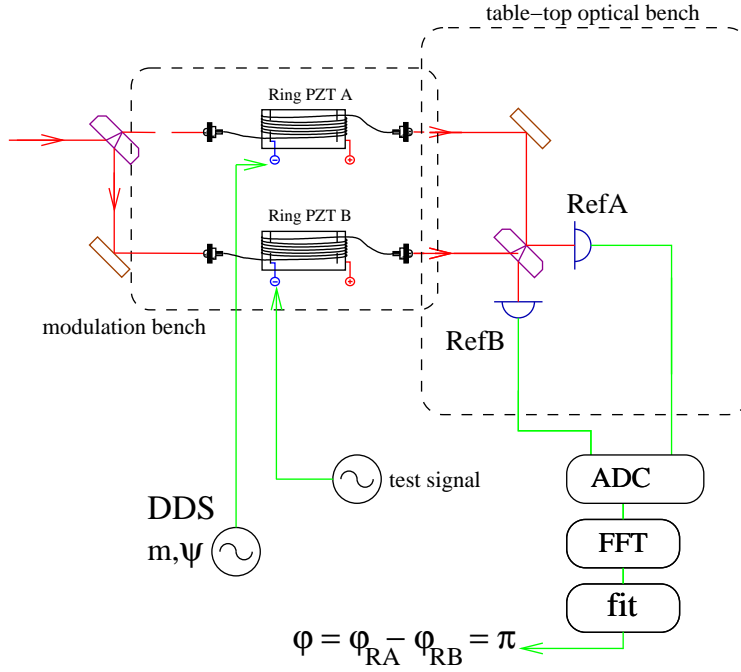
Figure 41: Actual laboratory breadboard implementation.

This verifies proper phasemeter operation, as the measured phase indeed follows the injected test signal. In addition, environmental phase noise can be observed from the shape distortion of the extracted ramp.

In order to determine the phasemeter noise level, the subtraction between the phases φ_A and φ_B measured in both channels was calculated online by the data processing program. The signals emerging from the complementary ports of the beam combiner should be phase-shifted by a constant value of π, and hence their difference does not include real pathlength fluctuations. However, the phasemeter operation is such that the phase of each individual channel is measured separately, and the fluctuations of this phase difference $\varphi_A - \varphi_B$ about its mean value (π) is an indication for the noise level of the PMS with real optical interferometer signals. Figure 43 shows the measured phase difference over a long-term run.
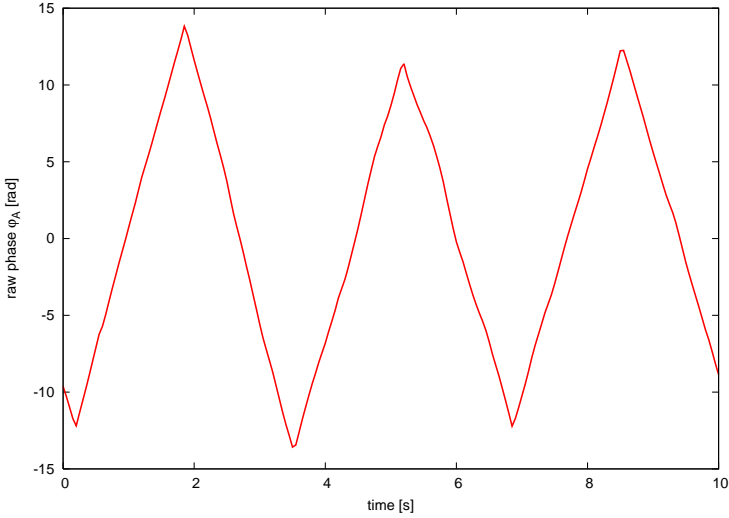
Figure 42: Time series of one raw phase measured at the table-top interferometer that was intentionally ramped over several fringes.

Moreover, the observation band of interest for LISA and LISA Pathfinder is below 100 mHz, and thus the LSD of this time series is computed in order to assess the phasemeter-photodiode noise level in this frequency range. The results are plotted in Figure 44 and indicate a noise level of the measured phase of the order of 10^{-3} rad/$\sqrt{\text{Hz}}$. The solid black traces are included for comparison purposes and point out the required noise budget allocated for the LTP experiment, its optical metrology system, and each individual interferometer noise source, respectively.

The shape of the obtained LSD ("shoulder" beneath 1 Hz) points to a systematic error in the measurement. The experience earned during noise investigations on the LTP interferometry [43] suggests that this spectral pattern is characteristic of a non-linear effect in the phase readout process that is also typified by a periodic dependence between the phase difference $\varphi_A - \varphi_B$ and a single raw phase $\varphi_{A/B}$. This periodic structure for a typical measurement can be recognized in Figure 45.

In LTP, this non-linearity is introduced by spurious sidebands in the RF signals, driving the AOMs responsible for the optical heterodyning [43, 44]. However, this
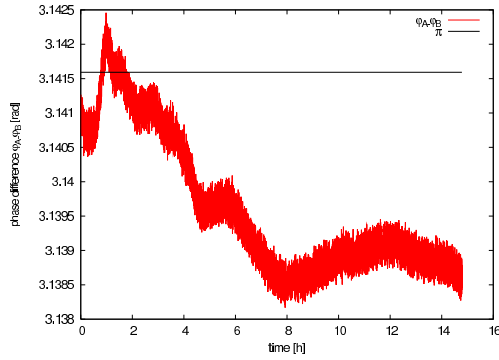
Figure 43: Time series of difference between two phasemeter channels $\varphi_A - \varphi_B$.
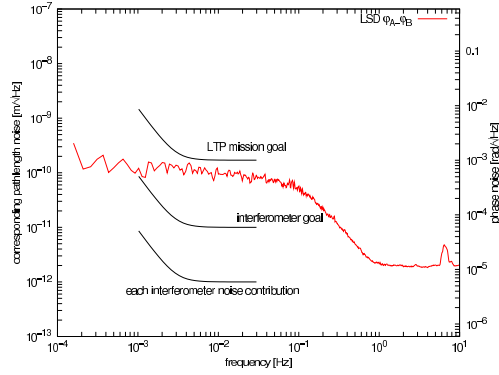
Figure 44: Linear spectral density of the phase difference $\varphi_A - \varphi_B$ that shows the noise level of the phase readout with optical signals.

cannot apply to this case, due to the clear difference in modulation schemes and hardware implementation between the two experiments. For this reason, synthetic data was generated and introduced into the phase extraction algorithm by software simulations, in order to investigate the origin of the noise source encountered here.
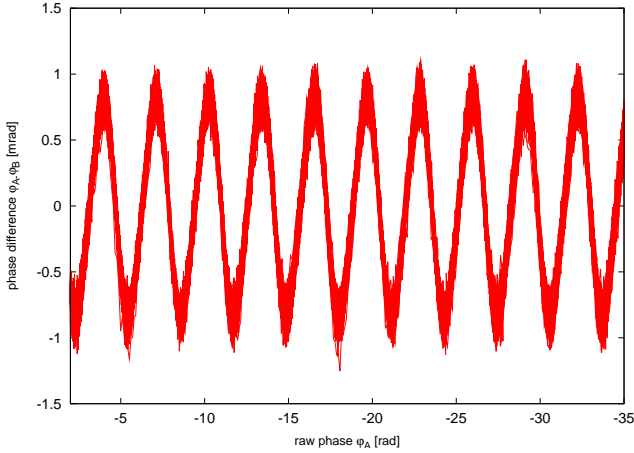
Figure 45: Periodicity between the phase difference $\varphi_A - \varphi_B$ and a single raw phase $\varphi_{A/B}$, characteristic of non-linearities in the phase readout.

6.2.2 *Software simulations*

A software simulation test bench was implemented in order to generate ideal data sets reproducing noise-free signals from a phase-modulated interferometer. This simulation environment reproduces the photodiode signal by generating mock-data sets of N_{FFT} points that are fed into the software processing part of the phasemeter, following the model of Equation 5.3 and rewritten in Equation 6.3:

$$V_n(t) = A \left[1 - c \cos \left(\varphi_{th} + m \cos \left(\omega_m t + \psi \right) \right) \right], \tag{6.3}$$

where the signal amplitude A and the interferometer visibility c were set to 1, and the modulation phase ψ was set to 0.

A check for correct operation of the data generation and the fit algorithm was done by linearly incrementing the preset interferometer phase φ_{th}, upon generation of N_{FFT} mock-data points. This way, a constant value of φ_{th} is ensured over the N_{FFT} samples required by the phasemeter software for the extraction of single phase data point. Figure 46 shows the time series recorded from the simulation for the preset phase φ_{th}, the phase extracted by the fit φ_{meas}, and the error between the two, which is of the order of 10^{-8} rad and can be attributed to the precision of the computation.

Chapter 6

67
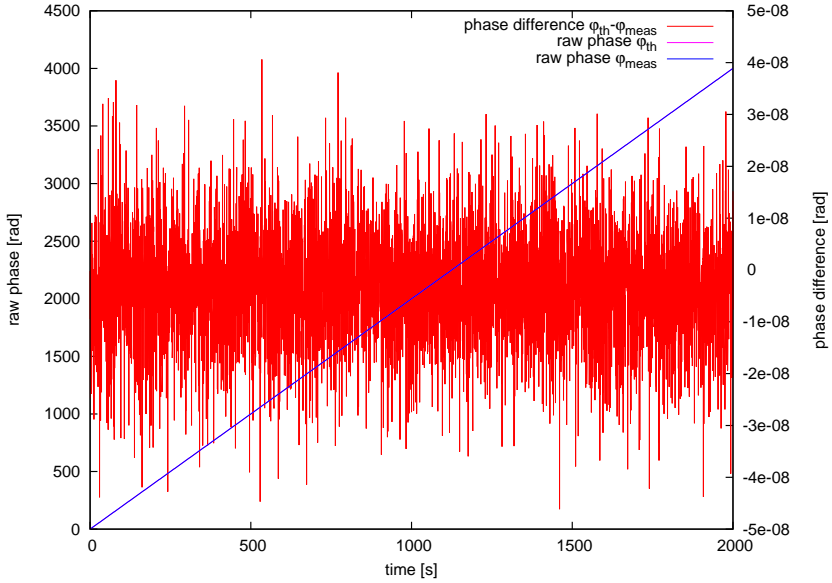
Figure 46: Time series recorded from the simulation for the preset phase φ_{th}, the phase extracted by the fit φ_{meas}, and the error between them that is of the order of 10^{-8} rad.

In addition, the simulation was extended to imitate hardware characteristics of the data acquisition system, such as effects of digitization and frequency response of the DAQ analog electronics (PD-AMP+AAF). Similar runs were performed under the influence of digitization in the data generation, which only delivered a higher flat noise level, as expected. Hence, this effect can be excluded as the cause of the noise shape observed.

However, the origin of this phenomenon was found by accounting for the frequency response of the analog electronics in the simulation. As illustrated in Figure 36, after the photodetector signal has passed through the DAQ analog electronics – hence being altered by its frequency response – and is sampled by the ADC (digitization), the data is Fourier transformed by a FFT routine and the 10 complex amplitudes of interest ($\tilde{c}_1 @ f_m \dots \tilde{c}_{10} @ 10 f_m$) are entered into the

fit algorithm. The following steps were undertaken in order to mimic the effect of the analog electronics:

1. The frequency response of the individual DAQ analog channels (PD-AMP+AAF) was measured and fitted to a model of poles and zeros. Figure 47 shows a Bode plot of the transfer function (TF) measured and fitted for one DAQ analog channel.
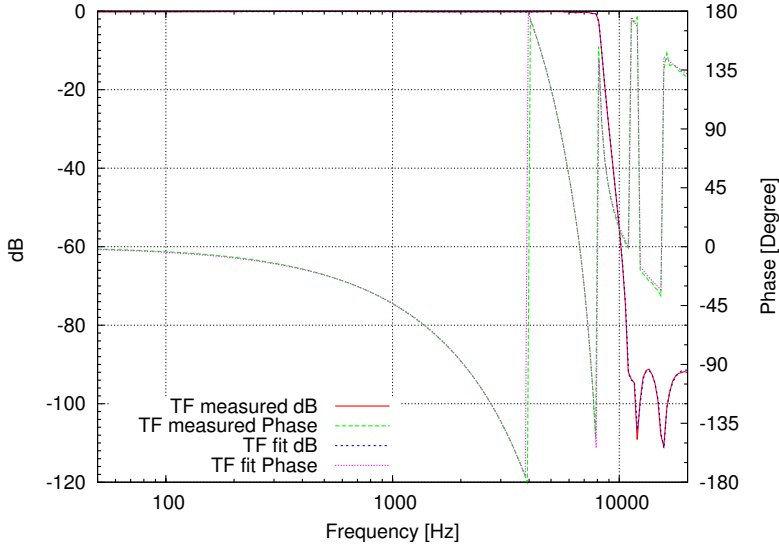
Figure 47: Transfer function of one analog channel of the data acquisition system.

Furthermore, according to the parameters chosen for the modulation and phase measurement systems, the frequency components of interest are only those between 280 Hz and 2800 Hz ($f_m \ldots 10\, f_m$). Figure 48 highlights this frequency range of the transfer function of one analog channel.

2. From the fitted model of this transfer function, the complex values β_n are obtained such that

$$\beta_n = b_n\, e^{i\theta_n}, \tag{6.4}$$

where b_n and θ_n are the magnitude and phase of the transfer function at the frequency n, respectively.

Chapter 6
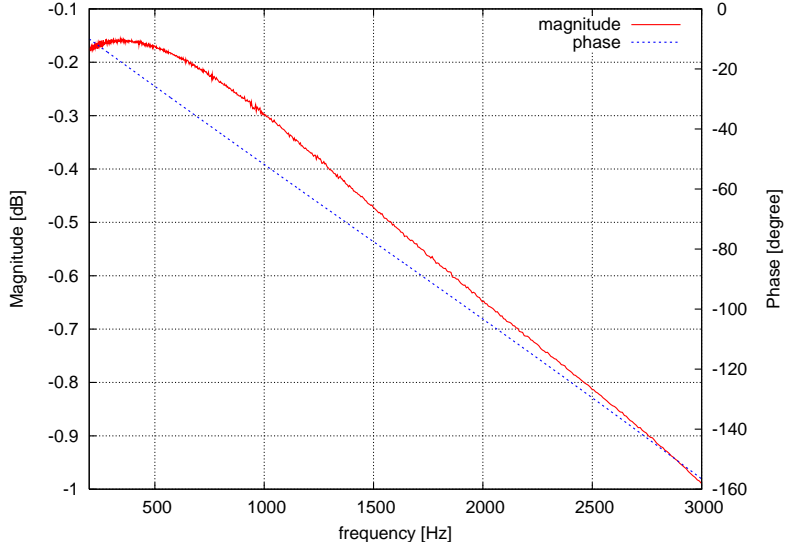
Figure 48: Transfer function of one analog channel of the data acquisition system in the frequency range between 280 Hz and 2800 Hz.

3. The complex amplitudes $\hat{c}_n$ computed by the FFT from the mock-data sets are modified by the simulation as:

$$\hat{c}'_n = \hat{c}_n \cdot \beta_n, \tag{6.5}$$

where $\check{c}_n$ are the complex amplitudes altered to mimic the effect of the DAQ analog electronics that are passed to the fit algorithm. Figure 49 outlines the periodic structure characteristic of a non-linearity in the phase readout $\varphi_{th} - \varphi_{meas}$ against φ_{th}, plotted for mock-data being altered by the transfer function of the DAQ analog electronics (red trace), and for ideal data without any further modification (blue trace). The periodicity of the resulting phase error is the indicator of importance in this plot, since it explains the behavior of the data. The difference in the error amplitude (approximately 10^{-5} to 10^{-3}) is given due to the definition of the transfer function in the program, in addition to the fact that the software produces almost perfect data without additional (real instrument) noise.

As explained in subsection 5.2.2, the desired observable φ containing the information of the test mass motion in a real optical length measurement, is
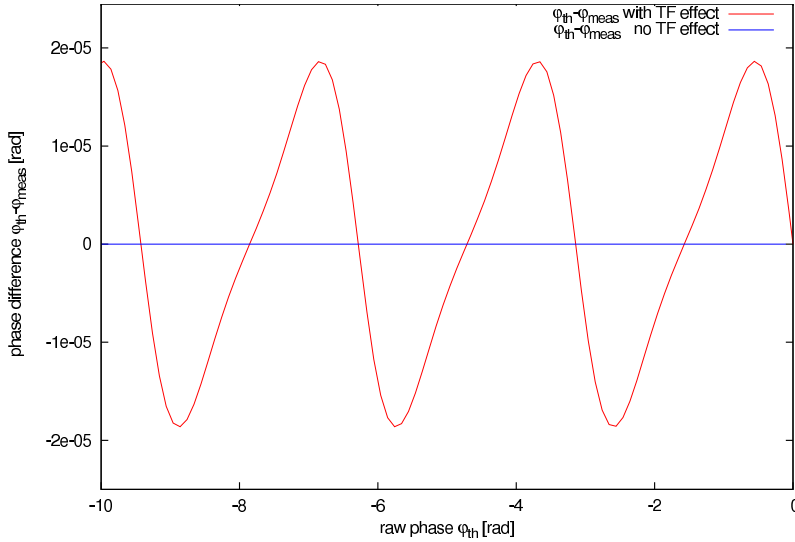
Figure 49: Periodic dependence between the phase difference $\varphi_{th} - \varphi_{meas}$ and a raw phase φ_{th}, characteristic of a non-linearity in the phase readout. Red trace: mock-data being altered by the transfer function of the analog electronics. Blue trace: ideal mock-data without any modification.

determined by fitting the relative measured complex amplitudes $\tilde{c}_n$ to a model of these harmonic components c_n. The ratio of the measured $\tilde{c}_n$ to each other is altered by the frequency-dependent weighting governed by the magnitude of the TF of the DAQ analog electronics, which varies in about 1 dB in the frequency range between 280 Hz and 2800 Hz. Thus, the fit algorithm is disturbed, resulting in a high noise level caused by a non-linearity in the phase readout.

The simulation turned out to be an useful tool to understand the behavior of the system. It was therefore further utilized in additional simulations, aiming to find optimum settings for the modulation and phase measurement systems, by varying their principal parameters in the mock-data generation.

An additional simulation was performed where the modulation depth m was increased linearly and the phase difference between two virtual phasemeter channels that included the effect of the DAQ analog electronics was recorded. The intention was to investigate any dependence of the noise level of the phase

Chapter 6

readout with m. The amplitude of the 10 harmonics and their sum was simultaneously recorded, as well. The results obtained are plotted in Figures 50 and 51, respectively.
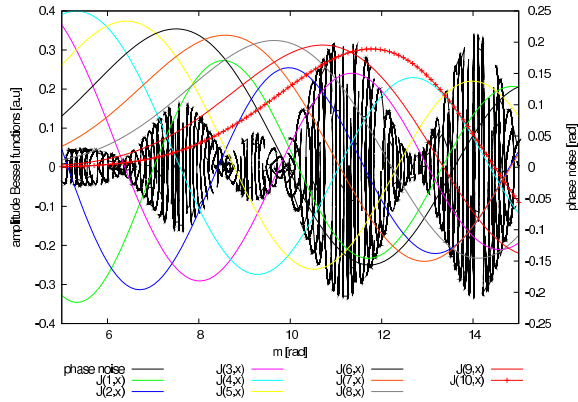
Figure 50: Dependence of the measured phase noise with m.
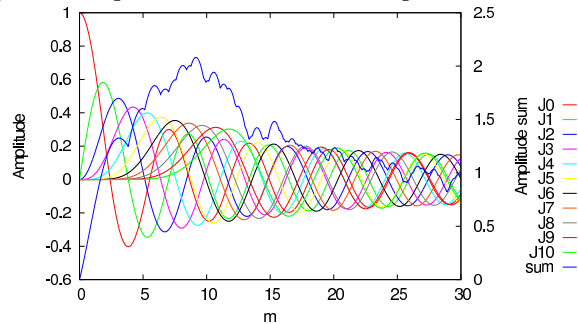
Figure 51: Dependence of the amplitudes of the 10 harmonics used in the fit algorithm with m.

A minimum of the phase noise in Figure 50 can be observed around $m = 9 - 10$, which suggests to set the modulation depth for real optical length measurements within this range, for a minimum phase noise. Similarly, the maximum value of the sum of the 10 harmonic amplitudes is located in this same range of m, indicating that the maximum SNR for the fit is around this operating point of the modulation depth.

On the basis of the results obtained here, which are consistent with the analysis presented in Figure 35, the number of harmonics to be used in the phase extraction fit algorithm was fixed to $N = 10$, and the modulation index for subsequent real optical length measurements was chosen to be $m \approx 9.7$.

6.3 OPTICAL LENGTH AND ATTITUDE MEASUREMENTS

An experiment for length and attitude measurements was assembled, according to the optical setup described in Section 6.1. The engineering model of the LTP optical bench was used as ultra-stable interferometer, and was operated together with the modulation bench (Figure 37) in a vacuum chamber at a typical pressure of 10^{-3} mbar. The settings for the modulation and phase measurement systems are the following:

- modulation: commercial signal generator set to a sine wave output at a frequency $f_m = 280\,Hz$ with an amplitude of approximately $4.5\,V$ that corresponds to a modulation index $m \approx 9.7$.

- phase measurement system:
    - sampling frequency is derived from a $10\,MHz$ clock provided by the signal generator in charge of the modulation. It has been set for each DAQ channel to $f_{samp} = 20\,kHz$.
    - number of samples for the Fourier transform $N_{FFT} = 1000$.
    - effective real-time phase measurement rate $f_\varphi = 20\,Hz$.
    - selected frequency component (bin) chosen to be coherent to the sampling frequency f_{samp} is $bin = 14$.
    - number of harmonics selected for the phase extraction fit algorithm is $N = 10$.

Further debugging and noise hunting was undertaken for these experiments, in order to overcome the effect of supplementary noise sources arising from real pathlength noise. Two effects were studied during these investigations and were determined to be the major limiting factors for the sensitivity of length and attitude measurements: (1) influence of the analog electronics transfer function, and (2) laser frequency noise.

6.3.1 *Transfer function correction*

As presented in Section 6.2, the frequency response of the analog electronics of the data acquisition system was found to cause a non-linearity in the in-

Chapter 6

terferometer phase φ readout, resulting in a high noise level. The approach chosen, in order to prevent this effect is based upon Equations 6.4 and 6.5. After measuring the transfer functions for all phasemeter channels and computing the corresponding complex values β_n for the frequency bins of interest, the measured complex amplitudes $\tilde{c}_n$ were consequently corrected by inverting Equation 6.5:

$$\tilde{c}'_n = \frac{\tilde{c}_n}{\beta_n}, \tag{6.6}$$

Following this transfer function correction in the measured harmonics, the program proceeds to enter the corrected complex amplitudes $\tilde{c}'_n$ into the fit algorithm. Figure 52 shows LSD plots for actual length measurements with (red) trace) and without (blue trace) transfer function correction. The conversion from
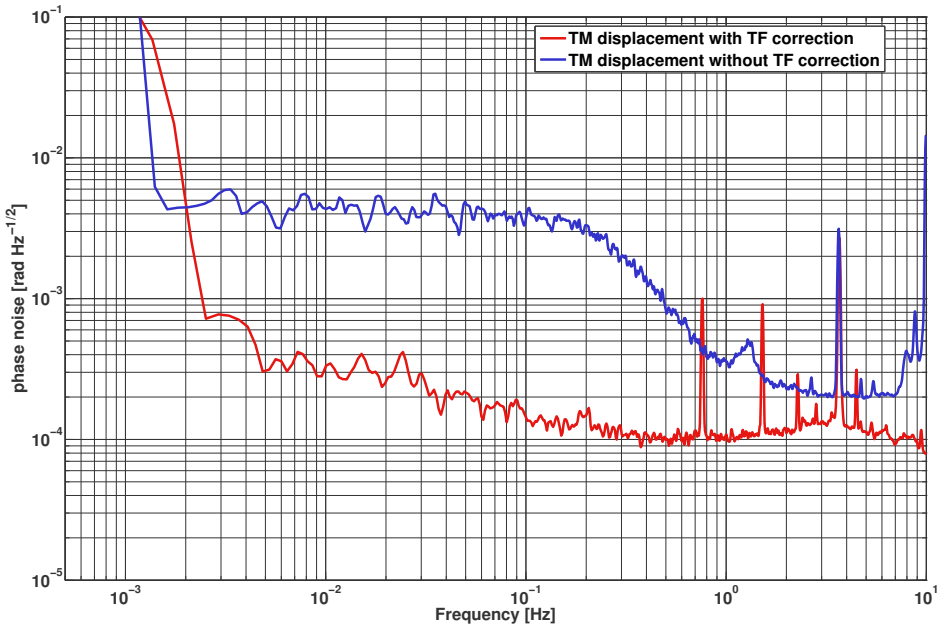
Figure 52: Sensitivity of real optical length measurements with (red) and without (blue) transfer function correction.

phase φ to longitudinal displacement x for the engineering model of the LTP optical bench interferometer (see Figure 68) is given by:

$$x = \frac{\varphi}{4\pi \cos \alpha} \lambda, \tag{6.7}$$

where $\lambda = 1064$ nm is the wavelength of the Nd:YAG laser used, and $\alpha \approx 3.6°$ is the angle of incidence of the laser beam onto the test mass. According to this conversion factor, the pathlength readout sensitivity for measurements without transfer function correction is of the order of $420\,\mathrm{pm}/\sqrt{\mathrm{Hz}}$ at 10mHz ($5\,\mathrm{mrad}/\sqrt{\mathrm{Hz}}$). By applying this correction to the measured amplitude of the harmonics, prior to entering the fit, the pathlength noise level is reduced to $30\,\mathrm{pm}/\sqrt{\mathrm{Hz}}$ 10mHz ($0.3\,\mathrm{mrad}/\sqrt{\mathrm{Hz}}$), showing an improvement close to 1.5 orders of magnitude.

6.3.2 *Laser frequency noise subtraction*

Laser frequency noise translates into phase readout noise in any interferometer, whose pathlength difference Δx between the two interfering beams is not exactly zero. The conversion factor from laser frequency fluctuations $\delta\nu$ into phase fluctuations $\delta\varphi$ is given by the difference in the time of travel of the two beams, introduced by the pathlength mismatch in the interferometer arms. In the case of the LTP EM optical bench, the pathlength difference Δx has been determined to be of the order of 10 mm [41].

As reported in [45], the free-running frequency noise $\delta\nu$ of an unstabilized Nd:YAG NPRO laser at 10 mHz is of the order of $2 \times 10^6\,\mathrm{Hz}/\sqrt{\mathrm{Hz}}$, and its translation into interferometer phase noise is given by

$$\delta\varphi = 2\pi \frac{\Delta x}{c} \delta\nu. \tag{6.8}$$

By evaluating Equation 6.8 with these values, it is possible to estimate the noise level for the phase readout $\delta\varphi$:

$$\delta\varphi = 2\pi \frac{\delta x}{c} \delta\nu = 2\pi \frac{10^{-2}\mathrm{m}}{3 \times 10^8\,\mathrm{m/s}} 2 \times 10^6\,\mathrm{Hz} = 0.4\,\mathrm{mrad}/\sqrt{\mathrm{Hz}}. \tag{6.9}$$

This value is consistent to the measured phase noise with a free-running laser ($0.3\,\mathrm{mrad}/\sqrt{\mathrm{Hz}}$), by applying the TF correction, as shown on Figure 52.

The LTP EM optical bench provides an auxiliary interferometer that has an

Chapter 6

intentionally large pathlength difference ($\approx 38\,\text{cm}$). An independent phase noise measurement of this interferometer – using the same method – is dominated by laser frequency fluctuations. The corresponding coupling factor into the main length measurement was estimated by fitting the time series of the phase measured at this interferometer to the one obtained from the sensitive test mass interferometer by a general least squares algorithm. Furthermore, the frequency fluctuations can be removed from the main length measurement by using this estimated coupling factor to subtract a properly scaled version of the phase data measured at this auxiliary interferometer. A detailed explanation of this noise subtraction fit algorithm is given in Section 9.4 and has been reported in reference [46].

In addition, a commercial iodine frequency stabilized Nd:YAG laser was employed for a supplementary length measurement. Due to the fact that the frequency stability of this laser system is sufficient for this experiment, laser frequency fluctuations were not a limiting factor for the sensitivity of the measurement. Figure 53 shows the LSD of the length measurements conducted with a free-running laser (red trace), after applying the frequency noise subtraction procedure (blue trace), and with the frequency stabilized laser system (green trace).

In spite of the slightly higher noise level measured with the frequency stabilized laser system compared to the measurement with a free-running laser (above 30 mHz) and its corresponding corrected data obtained from the noise subtraction algorithm (above 5 mHz), its flat spectral shape implies no presence of excess frequency noise, but a different circumstantial limiting factor not yet determined.

However, the LSD of the noise subtracted data in the range $2-5\,\text{mHz}$ is in agreement to the noise level measured with the frequency stabilized laser system. This together with the known behavior of laser frequency noise in Nd:YAG laser systems (as shown in [45]), increasing toward lower frequencies with a $1/f$ slope, indicates that the results obtained from the frequency noise subtraction algorithm are correct. This noise subtraction technique is explained in detail in Section 9.4. Thus, the sensitivity of the test mass optical length measurement reached by this technique at the LTP EM optical bench is of the order of $10\,\text{pm}/\sqrt{\text{Hz}}$ at 10 mHz, which is approaching – within one order of magnitude – the performance of the LTP heterodyne interferometry.

Besides laser frequency noise correction/stabilization, it can also be mentioned
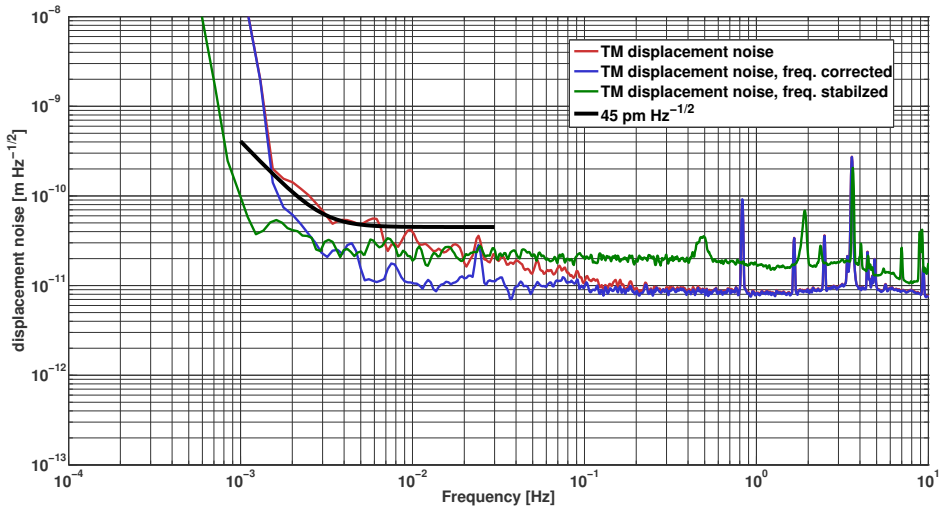
Figure 53: Optical length measurement with a free-running laser (red), after applying a subtraction algorithm to remove laser frequency noise (blue), and with the iodine-stabilized laser system (green). The black curve marks a goal of $45\,\text{pm}/\sqrt{\text{Hz}}$.

that this first prototype system does not yet include any additional noise reduction schemes, for instance, stabilization of the laser power or optical pathlength difference, as are already in-place in LTP. Nevertheless, the system is promising and its sensitivity can possibly be improved by implementing such stabilizations and noise investigations toward understanding the current limiting factors.

6.3.3 *Attitude measurement*

The signals emerging from the two complementary output ports of all four beam combiners on the LTP EM optical bench, are measured by quadrant photodetectors.

An optical measurement of the test mass attitude can be interferometrically done by processing the phase obtained for the individual channels of a QPD with a DWS algorithm, as explained in Section 1.2. Figure 54 shows the LSD of the optical measurement of the test mass attitude in one axis.

Chapter 6

77
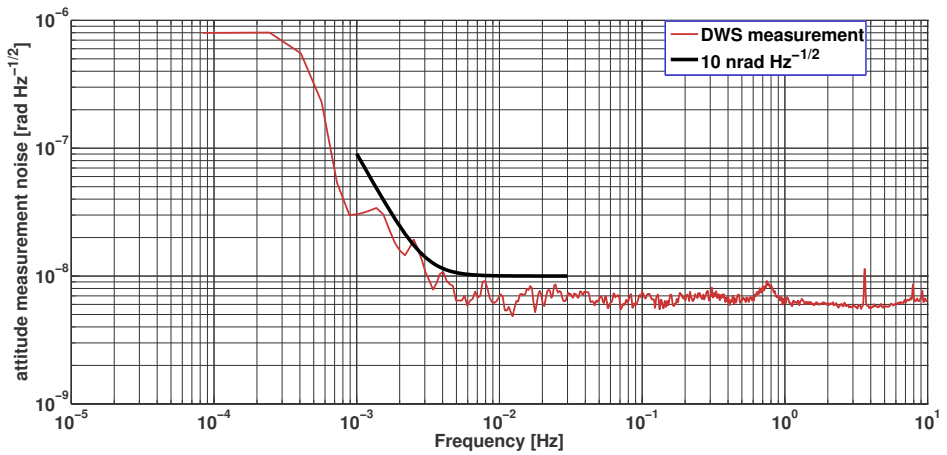
Figure 54: Noise level of the measurement of the test mass attitude by applying a DWS algorithm to the phases obtained by a QPD with this technique.

In this case, the black trace denotes the required sensitivity of $10 \, \text{nrad}/\sqrt{\text{Hz}}$ to the test mass angular jitter measurement in the LTP interferometry. As it can be seen, the performance of this technique for test mass attitude measurements, regarding its functionality and noise floor, is already at the level of the LTP interferometry.

SUMMARY AND OUTLOOK

The research work presented in this part was realized within the context of developing a simple, non-contact metrology system to locally monitor inertial reference sensors (test masses) in space-based gravitational wave experiments.

A laser interferometer based upon a Mach-Zehnder topology and with a so-called deep phase modulation technique, was chosen for this purpose. The laboratory implementation consists of the sinusoidal modulation of one interferometer arm with piezo-electric transducers, driving the interferometer phase over a large excursion range of the order of several fringes. Experiments conducted on the engineering model of the LISA Pathfinder optical bench, achieved a readout sensitivity of the order of $10\,\mathrm{pm}/\sqrt{\mathrm{Hz}}$ for the test mass displacement, and $10\,\mathrm{nrad}/\sqrt{\mathrm{Hz}}$ for attitude measurements in the millihertz observation band. This performance is about an order of magnitude better compared to other similar experiments developed for this same purpose. The results are comparable, within one order of magnitude, to the performance of the interferometry developed for the LISA Technology Package experiment onboard LISA Pathfinder. Moreover and in contrast to the LTP modulation bench, this implementation provides full redundancy for the phase modulators.

Two main effects were identified as limiting factors to the noise level of the instrument. A systematic error originates from the alteration of the relative harmonic amplitudes caused by the frequency response of the analog electronics. A fit algorithm uses the first 10 harmonics of the phase modulation signal to extract the interferometer phase. This limitation was overcome by measuring the transfer function of the analog segment of the data acquisition system, and correcting these complex amplitudes accordingly before entering the fit routine.

The second noise source treated were fluctuations of the laser frequency that proportionally translate as interferometer phase noise. In order to counteract this effect, two methods were applied that worked similarly well. One method considered the stabilization of the laser frequency, where a commercial iodine frequency stabilized laser system was employed for interferometric length measurements. Another alternative method based on a noise subtraction algorithm that estimates the coupling factor of laser frequency noise into the main mea-

surement. The engineering model of the LTP optical bench provides an auxiliary interferometer whose phase is dominated by laser frequency noise, due to an intentionally large armlength mismatch. This enables an independent measurement of laser frequency fluctuations that are then removed from the main data stream by properly scaling them with the coupling factor estimated by a fit algorithm.

In addition, this interferometry technique has proven to be promising, and it is therefore encouraged to further develop the system. The experience gained during this research work, suggests the following aspects to be taken into consideration in forthcoming investigations:

- Design of more appropriate frequency response of the analog electronics, in order to minimize their effect on the amplitudes of the harmonics used by fit algorithm for interferometric phase extraction.

- Implementation of stabilizations to counteract fluctuation in laser power – that may similarly affect the fit routine – and residual optical pathlength difference, as well as variations in the modulation depth applied, due to the shown non-linear coupling into the phase readout.

- Expansion and improvement of the fit routine and its model to account for additional noise sources and non-linearities, such as amplitude noise and hysteresis of piezo-electric transducers, among others. Different fitting techniques can also be considered and tested, such as algorithms working in the time domain.

- Development of an integrated modulation and phase measurement system for higher sampling frequencies and digitization resolution, that also includes a direct digital synthesizer to generate the modulation signal. The board can include digital hardware for the Fast Fourier Transform of the photodetector signal, as for instance in a FPGA, and the fit routine can be programmed, for example, in an onboard digital signal processor (DSP). Such a dedicated system would allow the controlled generation of the modulation signal using the fit output coming from the DSP as feedback. It would also enable to control the optical pathlength difference of the interferometer, by including its stabilization in the signal driving the PZT in charge of the phase modulation. This control signal could also be injected to the spare modulator, if desired.

This optical metrology technique could be useful in many other applications, such as surface profiling or length and attitude measurements with different purposes, besides space-based gravitational wave observation.

Part IV

LISA TECHNOLOGY PACKAGE

7
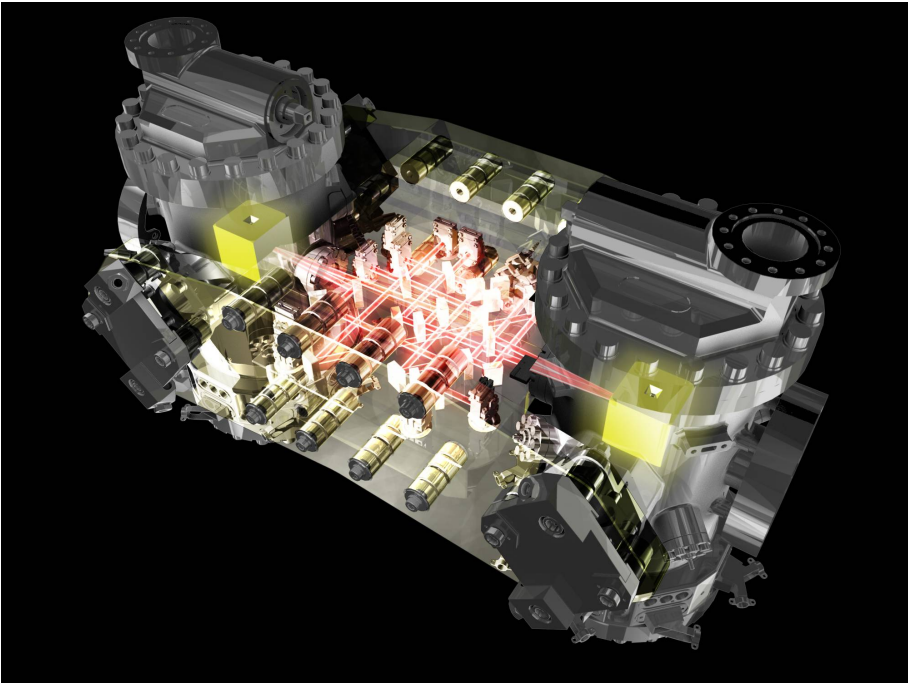
INTERFEROMETRY FOR THE LISA TECHNOLOGY PACKAGE

The first planned gravitational wave observatory in space, LISA, requires various novel technologies that are currently under development and cannot be fully tested on ground. It is therefore that ESA will launch the technology demonstration mission LISA Pathfinder, which consists of a single satellite carrying two payloads: the LISA Technology Package (LTP) provided by ESA, and the DRS from NASA. DRS was unfortunately descoped to a set of thrusters and a computer with software for test mass drag-free control and will not be further considered in this text. LTP [47] consists of a set of experiments designed to test core technology essential for LISA, such as:

1. free-fall motion of a test mass with an acceleration noise level better than $3 \times 10^{-14}\,\mathrm{m\,s^{-2}}/\sqrt{\mathrm{Hz}}$ at 1 mHz,

2. high-precision laser interferometry with a free-falling mirror (LTP test mass) with displacement sensitivity better than $6.3 \times 10^{-12}\,\mathrm{m}/\sqrt{\mathrm{Hz}}$ between 3 mHz and 30 mHz over a wide dynamic range (several microns),

3. satellite position correction via micronewton thrusters to assure a drag-free test mass in closed-loop operation.

4. assess reliability and lifetime of components, such as thrusters, optics, and lasers in space.

The main idea of LTP is to shorten one 5×10^9 m LISA interferometer arm to about 30 cm. A laser interferometer is located between the two LTP test masses and measures fluctuations in their separation with a resolution better than $6.3\,\mathrm{pm}/\sqrt{\mathrm{Hz}}$, as well as their attitude with a sensitivity of $20\,\mathrm{nrad}/\sqrt{\mathrm{Hz}}$, in the frequency band from 3 to 30 mHz.

The LTP interferometry[1] is an effort, resulting from a multinational collaboration of research institutions and industrial partners among Europe that is being extended toward the development of an end-to-end test facility for engineering and flight hardware for units of the LTP optical metrology system (OMS) at the Albert Einstein Institute Hannover.

Laboratory experiments and associated noise investigations have been conducted for testing the measurement principle to its required performance, and for developing algorithms for noise subtraction and data processing, as necessary for actual mission operations.

This chapter gives the status as of May 2009 and an introduction to the functionality and measurement principle of the LTP interferometry, its data processing and phase measurement.

7.1 INTERFEROMETER ARCHITECTURE

The optical metrology developed for the displacement and attitude measurement of a free-floating test mass in LTP is based on the phase detection of a low frequency (few kilohertz) sinusoidal signal generated by heterodyne laser interferometry. The instrument consists of a set of non-polarizing Mach-Zehnder interferometers, and utilizes two AOMs to individually shift the frequency of the beams. The motion of the test mass is proportional to the phase of the beat-note signal, resulting from the interference of the beams, whose frequency difference – heterodyne frequency – is between 500 and 2000 Hz. Two main sections constitute the LTP interferometer [48]: the modulation bench and the optical bench.

7.1.1 *Modulation bench*

The modulation bench consists of one Nd:YAG NPRO laser system that generates a single laser beam at a wavelength of 1064 nm. This beam is divided by a beamsplitter in two laser beams that are subsequently frequency-shifted by AOMs to obtain a frequency difference of about 1 kHz between them. Figure 55 shows a schematic diagram of the modulation bench.

The AOMs are driven by RF signals at approximately 80 MHz and the frequency-

---

1 The development of the LTP interferometry is long-term research project involving the full LTP team at AEI and collaborations with other research institutions and industrial partners.
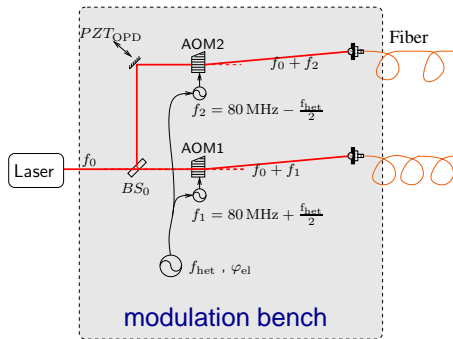
Figure 55: Schematic diagram of the LTP modulation bench.

shifted beams are coupled into fiber optics to be transferred to the optical bench. A PZT element is employed as actuator for active OPD stabilization, which is needed to suppress excess noise emerging from a non-linear effect in the phase readout produced by electromagnetic pick-up between the AOM RF signals [43, 44].

A breadboard implementation for laboratory experiments is described in Chapter 8. In addition, space-qualifiable engineering models of this modulation bench have been manufactured by industrial partners and are being currently tested at laboratories of the AEI. This effort will be introduced in Chapter 8, as well.

7.1.2 *Optical bench engineering model*

The LTP optical bench consists of a set of four non-polarizing heterodyne Mach-Zehnder interferometers that can be described as follows together with a schematic diagram of their optical paths:

- The TM 1 – TM 2 interferometer (labelled "12") measures fluctuations in the distance between the two drag-free test masses. Beam 1 and Beam 2 overlap at the beam combiner BS10, and the interference signal is obtained from the redundant quadrant photodiodes PD12A and PD12B.

- The TM 1 interferometer (labelled "1") monitors the position of test mass 1 with respect to the optical bench. Both beams recombine at the beamsplitter BS8, and the interference signal is obtained from the redundant
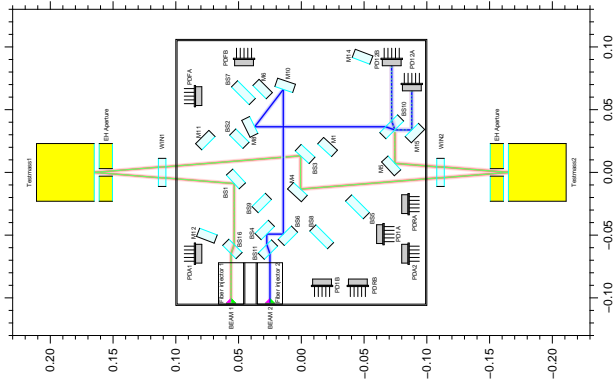
Figure 56: Optical layout of the TM 1 – TM 2 interferometer.

quadrant photodiodes PD1A and PD1B.

- The reference interferometer (R) operates within the optical bench only, detecting disturbances common to all interferometers that couple into the measurement in the more unstable part (modulation bench and fiber optics), such that they can be subtracted from 12 and 1. The recombination beamsplitter for this interferometer is BS5 and the readout photodetectors are PDRA and PDRB.

- The frequency stabilization interferometer (F) has an intentionally large OPD of approximately 38 cm, in order to sense laser frequency fluctuations such that its output signal can be used for active stabilization. The two beams overlap at BS7 and the input signal for the control loop is obtained from the photodetectors PDFA and PDFB.

The optical bench also has two photodiodes PDA1 and PDA2 as power monitors of the injected laser beams, which are stabilized by feeding back their signal to a control loop in the AOM driver electronics.

An engineering model (EM) of this optical bench was manufactured by attaching the fused-silica optical components onto a Zerodur® baseplate, using a technique known as hydroxide-catalysis bonding [19]. This work was conducted

in 2004 at Rutherford Appleton Laboratories in collaboration with the AEI and the University of Glasgow.

Due to its rigidness and the low CTE of Zerodur® (about 10^{-7}/K), this bonding procedure provides high mechanical and thermal stability, essential for precision interferometry at millihertz frequencies.
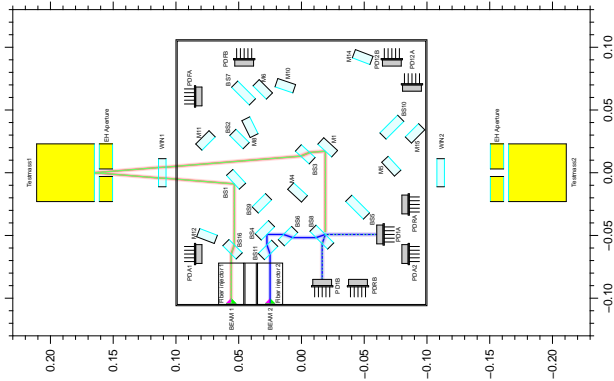
Figure 57: Optical layout of the TM 1 interferometer.
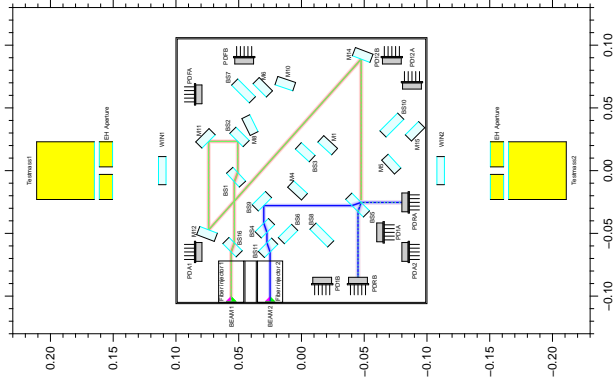
Figure 58: Optical layout of the reference interferometer.

The LTP EM optical bench has successfully undergone the required ESA space qualification process [49], demonstrated the required metrology performance, and has been used since then for further investigations at the AEI laboratories.

Chapter 7

89

Figure 60 is a photograph of the space-qualified engineering model of the LTP optical bench [41] and points out the location and mounting of test mirrors that simulate the LTP test masses in the experimental setup.
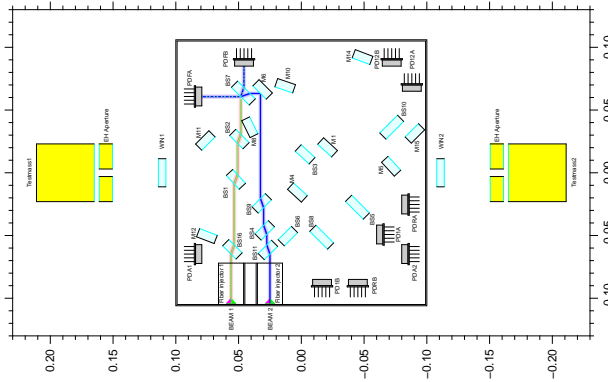
Figure 59: Optical layout of the frequency interferometer.
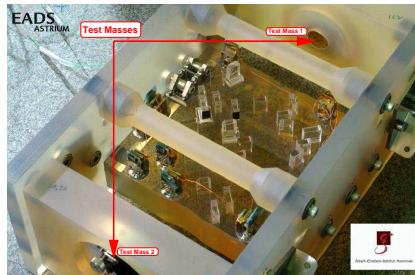
Figure 60: Space-qualified engineering model of the LTP optical bench. Note the expected location of the LTP test masses and the mounting of the test mirrors that simulate them.

Most of the results presented in this and the following chapters have been measured at this prototype[2]. A detailed description of the laboratory test bed setup for the performed investigations is given in Chapter 8.

2 Most of the measurements and results presented in Chapters 7 and 8 are the result of team work in the AEI LTP group: G. Heinzel, A. García, F. Guzmán, F. Steier, J. Reiche, and V. Wand.

7.1.3 *Modified design: optical bench flight model*

The original optical layout presented above in Section 7.1.2 defines the nominal positions of optical components at engineering model level. After successful manufacture and space qualification of the LTP OB EM, subsequent studies at system level concerning integration of LTP units and interaction of the OB with the test masses, resulted in tighter alignment tolerances and supplementary requirements for the OB FM.

As part of a comprehensive review of the OB EM construction and considering the additional requirements to the OB FM, it was judged that novel quasi-monolithic fiber injectors and some modifications to the optical layout were needed, aiming an improvement in mechanical stability, manufacturability and beam clearances at critical points.

Fiber injector optical subassembly

The EM OB was manufactured with commercial fiber injectors, aligned on the OB using a system of v-blocks and shims, as shown in Figure 61.
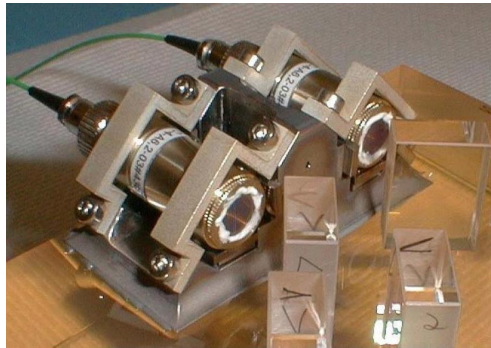
Figure 61: Photograph of the commercial fiber injectors used at the LTP OB EM.

However, these commercial devices are not well specified in terms of beam quality, mechanical stability and robustness of the optical assembly over the mission time-line, as well as cleanliness due to outgassing. Moreover, the tight requirements on adjusting the laser beam onto the nominal test mass reflection point within a 100 µm-side uncertainty cube demand high precision positioning

Chapter 7

of the fiber injectors and high stability of the final alignment.

A novel design for a fiber injector optical subassembly (FIOS) that meets the FM requirements has been developed and is currently under manufacture and space qualification at the University of Glasgow [50], in charge of delivering the LTP OB FM.

The main concept is to produce a quasi-monolithic unit that can be bonded onto the optical bench. The FIOS design consists of a fiber in a glass ferrule that is glued inside a fused-silica block. A single aspherical lens glued on a fused-silica carrier piece is used to collimate the beam. The lens carrier and fiber block are catalysis bonded to a small fused-silica baseplate with a very accurate separation, aiming for the desired beam parameters. A polarizing beamsplitter is glued to the baseplate at the output of the lens, in order to inject light with the correct s polarization into the OB.

Upon manufacturing two fiber injectors, these are bonded to a fused-silica post for precise adjustment of beam height and angle. Figure 62 shows a photograph[3] of the first FIOS prototype bonded to a OB FM-like baseplate used for the space-qualification process.
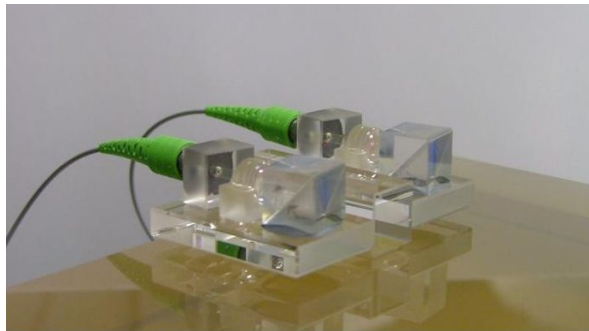
Figure 62: Photograph of the first FIOS prototype, bonded onto a LTP OB FM-like baseplate for space-qualification tests.

A wavefront detector [9] was used to measure the beam profile expected to be obtained from the FIOS at the main interference points. These results are presented in Chapter 9.

---

3 courtesy of the University of Glasgow

Modified optical layout

As a result of a detailed study of the OB EM layout some areas of potential difficulty were identified in the design, concerning clearance about beam clipping and component positioning for bonding. These areas are highlighted in Figure 63.
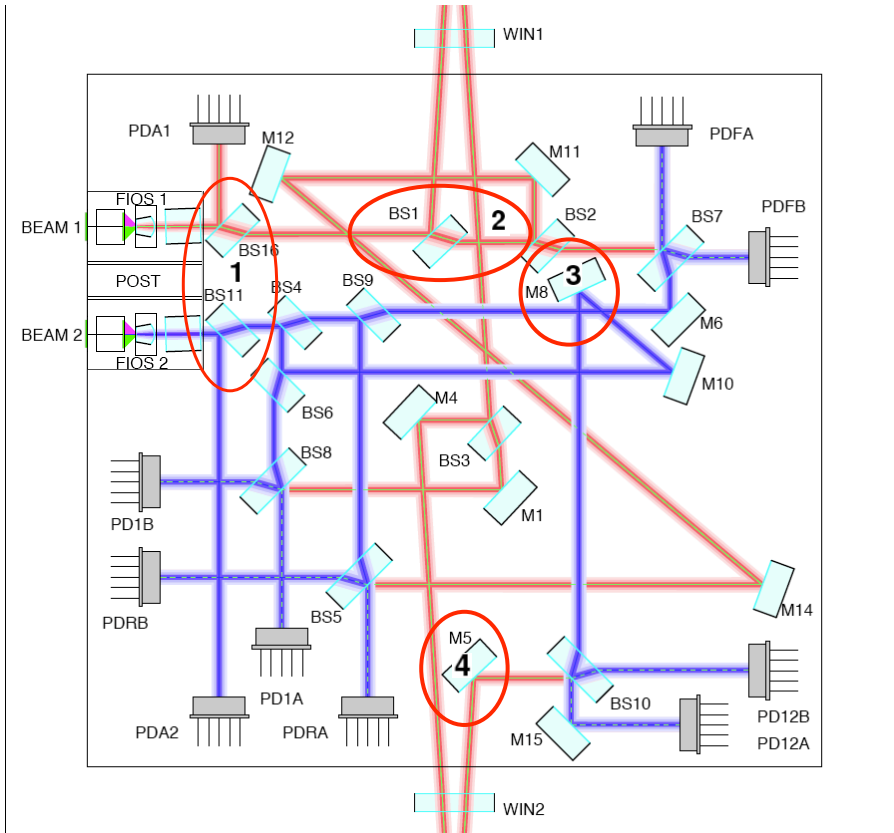
Figure 63: Areas of potential difficulty in the OB EM design.

It was necessary to relocate some optical components in order to achieve sufficient clearance to place the FIOS onto the optical bench, avoid beam clipping, and unfavorable locations of optical components. These changes induced additional

Chapter 7

93

component rearrangements, in order to re-equalize the optical pathlengths of the main interferometers (R, TM1, and TM1-TM2). The main modifications were:

- clearance to locate FIOS(1): Move BS16 and BS11 3 mm toward the OB center.

- beam clearance:
    - BS1(2) and M5(4): the angle of incidence of Beam 1 onto the test masses was increased from 3.6° to 4.5°, reducing potential clipping issues at these components.

    - M8(3): this component was shifted toward the recombination beam-splitter BS10. Beam 2 was then deflected in a different way over M8, M10, and M15 to the recombination point BS10. This modification prevents chamfers on M8 (back side, and reflective side) that were needed at EM manufacturing to avoid clipping.

- further modifications to adjust the OPD in the main interferometers:
    - M14 was shifted toward the OB center, due to relocation of M8 and M15.

    - BS5 was shifted toward BS9, due to relocation of M14. BS2 and M11 were moved closer to BS7 to match the optical path length of the reference interferometer.

    - BS8, BS3 and M1 were shifted toward test mass 2, due to relocation of BS5 and M14, as well as to match the optical path length of the TM1 interferometer.

    - M4 was relocated to deflect the overlapped beams at the output of the TM1 interferometer to PD1A. Beam 1 is being deflected to TM2 by BS3.

    - The photodiodes were relocated properly for the modified optical layout.

These modifications to the layout do not change the measurement principle of the interferometer. Moreover, no optical components were neither added to, nor removed from the optical bench.

For comparison purposes, Figure 64 outlines the layouts of the EM and FM

optical designs.
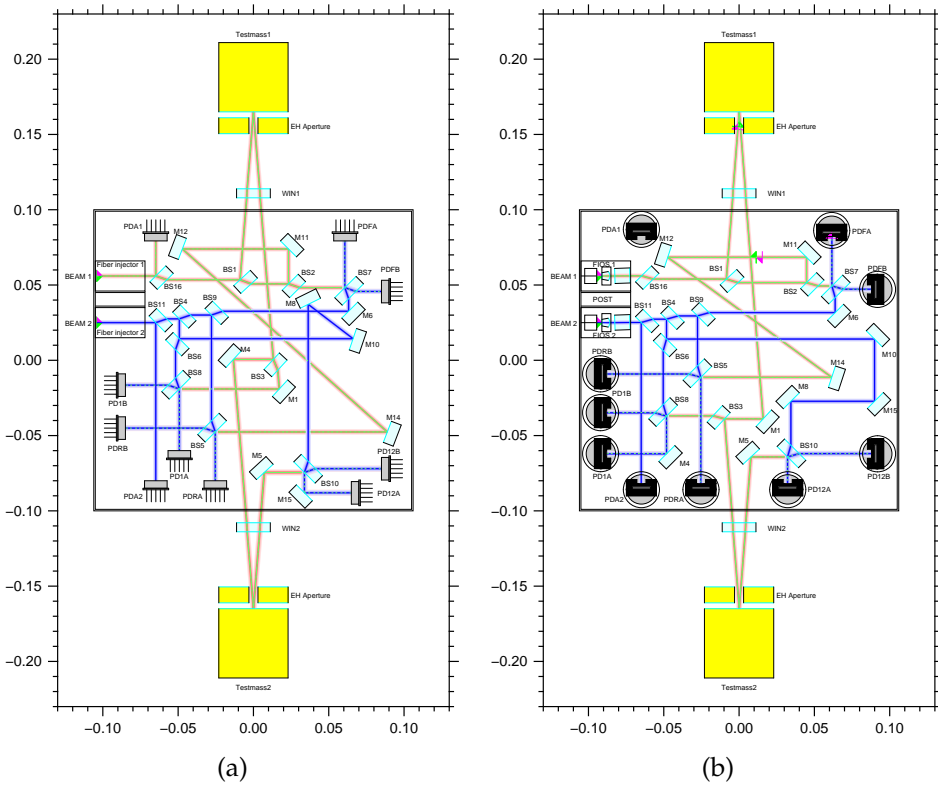
Figure 64: (a) Layout of the LTP OB EM optical design. (b) Layout of the LTP OB FM optical design.

The following Section 7.2 describes the phase measurement system designed to readout the interferometers presented here, and the defined data processing chain to obtain the corresponding test mass displacement and attitude in the LTP experiment.

7.2 PHASE MEASUREMENT SYSTEM AND DATA PROCESSING

7.2.1 *Phase computation and phasemeter*

The signal measured at each individual channel n of the QPDs on the LTP optical bench can be expressed as:

$$V_{PD}(t) = A \left[1 - c \cos \left(\omega_{het} \, t + \psi_n \right) \right], \tag{7.1}$$

where

- ψ_n is the interferometric phase measured at quadrant n,

- $\omega_{het} = 2\pi \, f_{het}$ is the heterodyne frequency of the order of $1\,\text{kHz}$,

- A is the amplitude of the signal, and

- c is the contrast or visibility of the interferometer.

The phase measurement is based upon a single-bin discrete Fourier Transform (SBFT) [45] at the heterodyne frequency. The signal from each channel n is sampled by an dedicated ADC, and split into consecutive segments of length N_{SBFT}. The data is processed in digital hardware by means of FPGAs where the SBFT is computed by multiplying the sampled amplitude data streams I with two sets of coefficients in orthogonal quadratures a and b (cosine and sine tables, respectively):

$$d = \sum_{i=0}^{N_{SBFT}} \left(\mid a_i \mid + \mid b_i \mid \right) I_i, \tag{7.2}$$

$$z = \sum_{i=0}^{N_{SBFT}} a_i \, I_i, \tag{7.3}$$

$$y = \sum_{i=0}^{N_{SBFT}} b_i \, I_i, \tag{7.4}$$

where d is the DC level of each channel, z and y are the real and imaginary part obtained from the SBFT, respectively.

The phase ψ_n of the signal at channel n can be computed as the argument of the complex number $F = z + i\,y$:

$$\psi_n = \arg(F) = \arctan \left(\frac{y}{z} \right). \tag{7.5}$$

For correct behavior in all four quadrants of the complex plane the $\text{atan2}(x, y)$ function must be used in the software.

A laboratory prototype phasemeter[4] with 20 input channels has been developed at AEI (see Figure 65).
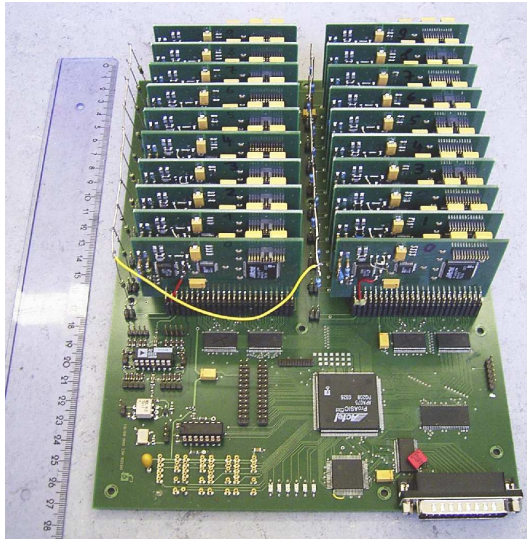
Figure 65: Photograph of the laboratory phasemeter prototype developed at AEI.

A single input channel consist of a low-noise transimpedance amplifier to convert the photocurrent to a voltage, an 18-bit ADC running at a sampling frequency $f_{samp} = 800\,\text{kHz}$, and one FPGA for the SBFT computation. The ADCs in all input channels are triggered by the same master clock for synchronous sampling. The phasemeter has been equipped with a parallel port interface, in order to transfer the SBFT output to a PC for phase computation and further processing.

The setting parameters of the phasemeter for typical operation in laboratory experiments are:

- heterodyne frequency $f_{het} = \frac{10\,\text{MHz}}{6160} \approx 1623.38\,\text{Hz}$.

---

4 developed by G. Heinzel

- sampling frequency $f_{samp} = 800$ kHz.

- length of sampled data sets for SBFT, $N_{SBFT} = 24640$.

- frequency component corresponding to f_{het}, bin $= 50$.

- effective real-time phase measurement rate $f_\varphi = 32.47$ Hz.

This instrument allows to conduct laboratory experiments with LTP-representative hardware, since its design is comparable to the LTP flight phasemeter, which mainly differs by the following characteristics:

- the usage of space-compatible hardware.

- 16 input channels with 16-bit ADCs and space-qualified FPGAs.

- nominal heterodyne frequency $f_{het} = 1$ kHz.

- nominal sampling frequency $f_{samp} = 50$ kHz.

- nominal SBFT length $N_{SBFT} = 500$.

- nominal bin $= 10$.

- effective real-time phase measurement rate $f_\varphi = 100$ Hz.

- communication over a MIL-STD-1553 interface (MIL-BUS standard IEEE 1553) with other LTP units, including the DMU, which is the computer in charge of the phase computation and interferometric signal processing.

The latter point is of importance in the setup of a test facility at AEI for engineering and flight hardware of the LTP units, as presented in Chapter 8. For redundancy purposes, LTP is equipped with two of these phasemeters, enabling the processing of 32 channels in total.

7.2.2 *Data processing*

The optical bench contains redundant quadrant photodiodes at the two complementary output ports – A and B – of each interferometer. The following convention has been defined to identify the output of the two redundant phasemeters:

$$W_{i,j,k} \, , \tag{7.6}$$

where $i = \{1, 12, R, F\}$ refers to the respective interferometer (TM 1, TM 1-TM 2, Reference, Frequency), $j = \{A, B, C, D\}$ designates the single channels of a QPD as in Figure 66, and $k = \{A, B\}$ identifies the corresponding phasemeter where the data $W = \{d, z, y\}$ is coming from, according to Equations 7.2–7.4.
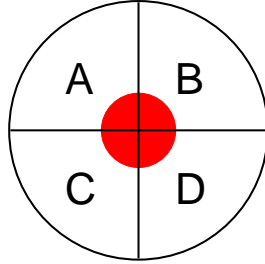
Figure 66: Label convention of QPD channels.

The interferometric data processing has been defined such that in nominal operation, the signals from all channels in a single interferometer are used to compute the longitudinal and angular measurements [51]. This means, that according to the convention defined in Equation 7.6, redundant quadrants are combined to average their signals for the calculations. However, redundant quadrants must be carefully selected for this averaging, as for instance, depending on the precise optical layout of each interferometer, left (A,C) and right (B,D) side of the QPDs may be swapped (see Figure 67) due to an additional reflection at the recombination beamsplitter.

The following intermediate quantities are obtained per interferometer i:

- total DC level Σ_i:

$$\Sigma_i = \sum_j \frac{1}{2} \left(d_{i,j,A} + d_{i,j,B} \right) \tag{7.7}$$

- total complex amplitude F_i:

$$F_i = \sum_j \frac{1}{2} \left(F_{i,j,A} + F_{i,j,B} \right) \tag{7.8}$$
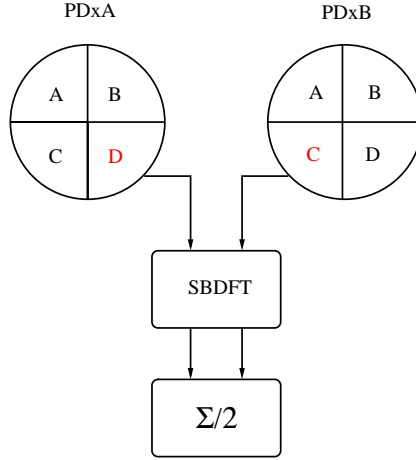
Figure 67: Illustration of an example of averaging signals from redundant QPD channels.

- left side DC level Σ_i^{left} and complex amplitude F_i^{left}:

$$\Sigma_i^{\text{left}} \quad = \quad \sum_k \left(d_{i,A,k} + d_{i,C,k} \right) \tag{7.9}$$

$$F_i^{\text{left}} \quad = \quad \sum_k \left(F_{i,A,k} + F_{i,C,k} \right) \tag{7.10}$$

- right side DC level Σ_i^{right} and complex amplitude F_i^{right}:

$$\Sigma_i^{\text{right}} \quad = \quad \sum_k \left(d_{i,B,k} + d_{i,D,k} \right) \tag{7.11}$$

$$F_i^{\text{right}} \quad = \quad \sum_k \left(F_{i,B,k} + F_{i,D,k} \right) \tag{7.12}$$

- upper side DC level Σ_i^{up} and complex amplitude F_i^{up}:

$$\Sigma_i^{\text{up}} \quad = \quad \sum_k \left(d_{i,A,k} + d_{i,B,k} \right) \tag{7.13}$$

$$F_i^{\text{up}} \quad = \quad \sum_k \left(F_{i,A,k} + F_{i,B,k} \right) \tag{7.14}$$

- lower side DC level Σ_i^{down} and complex amplitude F_i^{down}:

$$\Sigma_i^{down} = \sum_k \left(d_{i,C,k} + d_{i,D,k} \right) \tag{7.15}$$

$$F_i^{down} = \sum_k \left(F_{i,C,k} + F_{i,D,k} \right) \tag{7.16}$$

As explained in Section 7.1.2, the reference interferometer (R) is mainly used to detect common environmental noise that is sensed by all interferometers and can be subtracted from their data streams, to achieve a higher sensitivity in the main test mass measurements. Accordingly, the longitudinal phase Ψ for the single interferometers is computed as

$$\Psi_1 = PT\left(\arg\left(F_1 \right) - \arg\left(F_R \right) \right) \tag{7.17}$$

$$\Psi_{12} = PT\left(\arg\left(F_{12} \right) - \arg\left(F_R \right) \right) \tag{7.18}$$

$$\Psi_R = PT\left(\arg\left(F_R \right) \right) \tag{7.19}$$

$$\Psi_F = PT\left(\arg\left(F_F \right) - \arg\left(F_R \right) \right), \tag{7.20}$$

where the function $PT(\Psi)$ represents a phase unwrapping algorithm in order to prevent phase jumps in the time series.

The interferometer alignment is also calculated twice with DC signals and by applying a DWS algorithm, as mentioned in Section 1.2. The measurements at the TM 1 and TM 1-TM 2 interferometers provide information about the horizontal φ and vertical η test mass angular orientation:

$$\varphi_i^{DC} = \frac{\Sigma_i^{left} - \Sigma_i^{right}}{\Sigma_i} \kappa_\varphi^{DC} \tag{7.21}$$

$$\eta_i^{DC} = \frac{\Sigma_i^{up} - \Sigma_i^{down}}{\Sigma_i} \kappa_\eta^{DC} \tag{7.22}$$

$$\varphi_i^{DWS} = \arg\left(\frac{F_i^{left}}{F_i^{right}} \right) \kappa_\varphi^{DWS} \tag{7.23}$$

$$\eta_i^{DWS} = \arg\left(\frac{F_i^{up}}{F_i^{down}} \right) \kappa_\eta^{DWS}, \tag{7.24}$$

where the constants κ are the measured calibration factors from the DC and DWS measurements to real test mass angles, as presented in Section 1.2.

Chapter 7

The total optical path s covered by the laser beam is proportional to the interferometric phase Ψ as:

$$s = \frac{\lambda}{2\pi}\Psi, \tag{7.25}$$

where $\lambda = 1064\,\text{nm}$ is the wavelength of the laser.

In order to compute the conversion of measured interferometric phase Ψ in test mass displacement x, it is necessary to consider the specific LTP OB geometry, which is depicted in Figure 68.
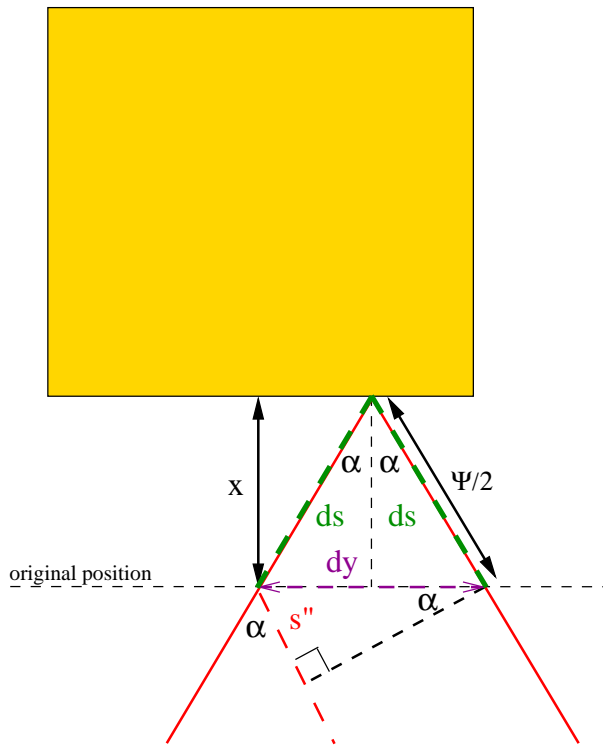
Figure 68: Conversion of test mass displacement into interferometric phase measurement.

The following mathematical relations can be obtained from this geometry:

$$ds = \frac{x}{\cos\alpha}$$
$$dy = 2\,ds\,\sin\alpha$$
$$s'' = dy\,\sin\alpha = 2\,\frac{\sin^2\alpha}{\cos\alpha}$$
$$s = 2\,ds + s'' = 2\,x\,\frac{1-\sin^2\alpha}{\cos\alpha} = 2\,x\,\cos\alpha$$

Hence,

$$x = \frac{s}{2\cos\alpha} \tag{7.26}$$

Finally, from Equations 7.25 and 7.26, the displacement x of test masses 1 and 2 can be obtained from the measured longitudinal phases $\Psi_{1/12}$ as:

$$x_1 = \frac{\lambda}{4\pi\cos\alpha}\Psi_1, \tag{7.27}$$

$$x_{12} = x_1 - x_2 = \frac{\lambda}{4\pi\cos\alpha}\Psi_{12}, \tag{7.28}$$

where $\lambda = 1064\,\text{nm}$ is the wavelength of the Nd:YAG laser used, and α is the angle of incidence of beam onto the test masses, which is $3.6°$ in the EM and $4.5°$ in the FM.

The processing of the phasemeter output (d, z, and y) as described here corresponds to the baseline to be implemented on the flight DMU, and has been programmed in a laboratory PC to operate the LTP OMS test facility at AEI.

A detailed description of the LTP OMS facilities set up at AEI for laboratory experiments and tests of engineering and flight models is provided in Chapter 8.

Chapter 7

8

TEST FACILITIES

An experimental setup for further LTP interferometry investigations has been assembled to operate the engineering model of the optical bench with supporting laboratory equipment, as a prototype of the LTP optical metrology system. Some of these investigations are presented in Chapter 9.

This setup has been extended for verification of functionality and noise level of industrial engineering models, starting with the RLU and LMU (modulation bench Section 7.1.1), and forthcoming flight model tests.

8.1 LABORATORY EXPERIMENTAL TEST BED

The experimental setup consists of a breadboard modulation bench and the LTP OB EM.

The breadboard modulation bench shown in Figure 69, has been assembled with a commercial Nd:YAG NPRO laser, and optics for optimal adjustment of the required s polarization.

After passing the AOMs, the frequency-shifted beams are coupled into fiber optics, and a mirror mounted on a PZT element is used as actuator for an OPD stabilization. The beams are injected into the optical bench, residing in a vacuum tank (via optical feed-throughs) (see Figure 70) typically operated at a pressure of the order of 10^{-3} mbar.

The vacuum tank is equipped with optical and electrical feed-throughs to inject the beam inside the tank and to transfer the photocurrents measured at the QPDs to the FPGA-based phasemeter.
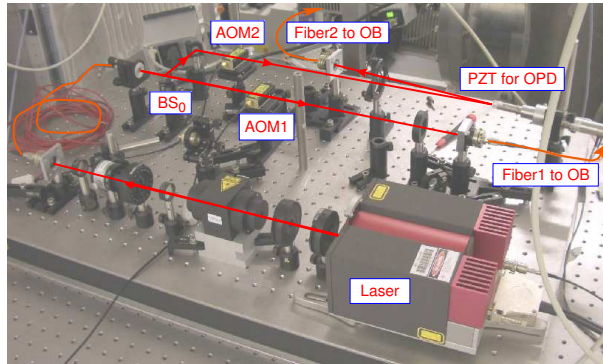
Figure 69: Photograph of the breadboard modulation bench for laboratory experiments.

The modulation electronics consist mainly of two oscillators for generation of RF signals (see Figure 71 (a)[1]). Each temperature compensated voltage-controlled crystal oscillator (TCVCXO) runs at a frequency of approximately 80 MHz which is steered by a phase-locked loop (PLL) (see Figure 71 (b)[1]) to a difference heterodyne frequency of about 1.6 kHz between the two.

An electric heterodyne signal is extracted from the mixer output, and is used to stabilize the TCVCXO frequencies. This signal is compared to the optical heterodyne signal, measured at the reference interferometer, in order to set up an OPD stabilization, which is explained in Section 8.2.2 and 8.4.2. Furthermore, the power of the TCVCXO signals is increased by HV amplifiers to drive the AOMs. The AOM drivers are equipped with an additional input that can be used to regulate the amplitude of the RF output signals, which enables the power stabilization of the individual laser beams. An additional control loop can be established by mixing down the heterodyne signals measured at the reference and frequency interferometers, in order to stabilize the laser frequency.

These three stabilization systems for laser power, OPD, and laser frequency are necessary to achieve the required LTP longitudinal measurement accuracy of $6.3 \times 10^{-12}\,\mathrm{m}/\sqrt{\mathrm{Hz}}$ between 3 mHz and 30 mHz. Their laboratory implementation is presented in the following Section 8.2.

---

1 developed by G. Heinzel

Figure 70: Photograph of the vacuum tank containing the OB EM in the LTP laboratory at AEI.

(a)
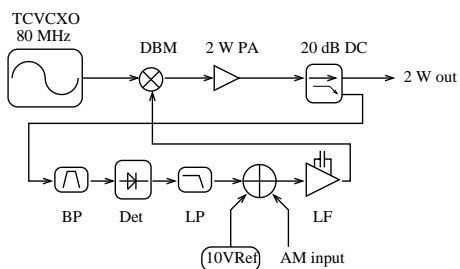
TCVCXO = Temp. compens. VCXO
DBM = double balanced mixer (used as attenuator)
PA = Power Amplifier
DC = Directional Coupler
BP = 80 MHz Bandpass
Det = Schottky Detector
LP = 10 MHz Lowpass
LF = Loop Filter
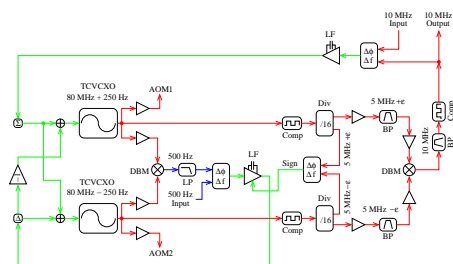
(b)

TCVCXO = temperature compensated voltage controlled crystal oscillator   Comp = comparator to generate logic level signals
LP = lowpass filter   Div = digital frequency divider
BP = bandpass filter   DBM = double balanced mixer
LF = loop filter   Δφ/Δf = digital phase/frequency detector

Figure 71: (a) Block-diagram of the PLL. (b) Block-diagram of the AOM drivers.

107

Chapter 8

8.2 stabilization systems

8.2.1 *Laser power stabilization*

Fluctuations of the laser power corresponding to the heterodyne frequency f_{het}, couple directly into the phase measurement (Equations 7.3–7.5). Moreover, slower power variations of the measurement beam (Beam 1) in the frequency range of $3 - 30$ mHz exert spurious forces on the test masses, disturbing their motion by radiation pressure noise [45].

For interferometry experiments, an AC-coupled analog control loop has been implemented to stabilize the laser power, in order to suppress fluctuations around the heterodyne frequency that may affect the phase measurement. A fraction of the beam light is picked up individually by the photodiodes PDA1 and PDA2. Their signals are fed into the associated circuitry to produce a control signal that is injected into an additional input at the corresponding AOM drivers for amplitude regulation of the first diffraction order beams emerging from the AOMs.

Figure 72 shows the measured OLG of the analog servos for the power stabilizations of the measurement (MB) (a) and reference (RB) (b) beams.

(a)   (b)
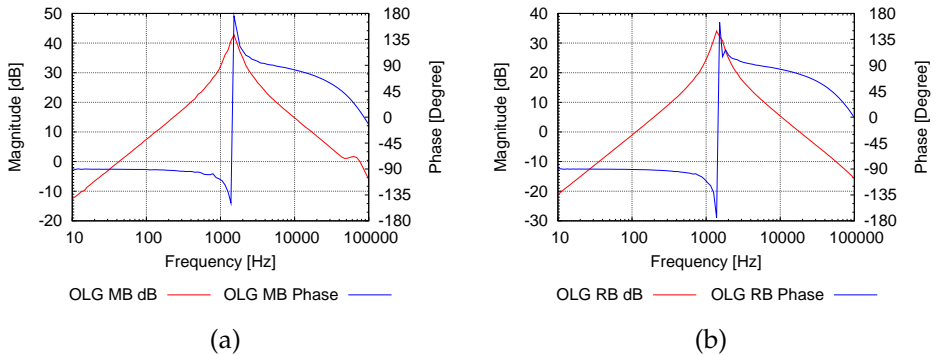
Figure 72: (a) OLG of the measurement beam power stabilization. (b) OLG of the reference beam power stabilization.

8.2.2 *Stabilization of optical pathlength difference*

The reference interferometer depicted in Figure 58 is mainly used to sense common-mode phase fluctuations caused by environmental noise, such as fluctuations in the modulation bench and fiber optics that couple into all four interferometers. This common-mode phase noise has to be subtracted from the other three interferometers (TM 1, TM 1-TM 2, frequency stabilization) in order to increase their sensitivity. However, non-linear excess noise, which originates from electromagnetic cross-coupling between the RF signals driving the AOMs, dominates the phase data streams at the milliradian level. This effect generates sidebands in the optical signals that interfere at the photodetector, producing beats at the heterodyne frequency [44]. The phase of this spurious contribution to the main signal is unstable and induces phase fluctuations in the net measured carrier at the milliradian level [44]. In order to mitigate this excess noise, an active stabilization of the optical pathlength difference has been implemented, by comparing the phase of the reference interferometer to the phase of the electric heterodyne signal – obtained from the modulation electronics (PLL) – and controlling this difference to be held constant by a servo. A free-beam actuator has been implemented within the modulation bench in the laboratory test bed, by mounting a mirror on a PZT element as shown on Figure 69. The PZT is driven by the control loop to correct the optical path, in order to compensate these phase fluctuations. Figure 73 shows the OLG measured for the OPD control loop, which reaches a bandwidth of 60 Hz.
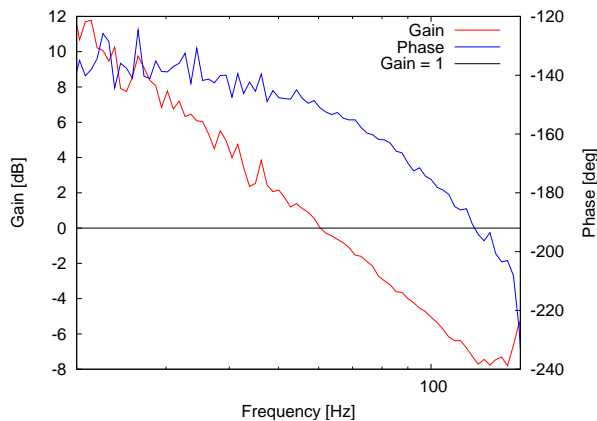
Figure 73: Measured OLG of the OPD stabilization.

Chapter 8

109

8.2.3 *Laser frequency stabilization*

As mentioned in Section 6.3.2, laser frequency fluctuations δν proportionally translate to phase fluctuations Δφ by the length mismatch between the interferometer arms δx:

$$\delta\varphi = 2\pi\frac{\Delta x}{c}\delta\nu. \tag{8.1}$$

The armlength mismatch Δx has been measured to be of the order of 10 mm [41] in the main interferometers (TM 1, TM 1-TM 2, reference) and is intentionally increased to 38 cm in the frequency interferometer in order to increase its sensitivity to fluctuations of the laser frequency. In order to stabilize the laser frequency, the difference between the phases measured at the frequency and reference interferometers is held constant, by using a split control signal driving two actuators: the PZT element and the temperature controller, both acting on the laser crystal [45].

Figure 74 shows the OLG measured for the control loop implemented in the laboratory to stabilize the laser frequency.
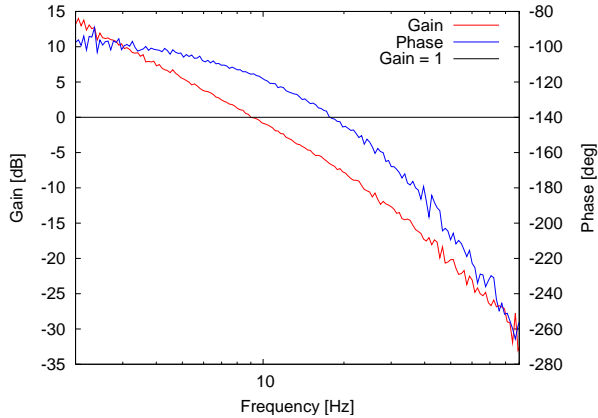
Figure 74: Measured OLG of the laser frequency stabilization.

8.3 INTERFEROMETER LENGTH AND ANGULAR SENSITIVITY

The experimental setup described in Section 8.1 was used to conduct long-term interferometric measurements of the test mass displacement. Figure 75 shows the results obtained from two different runs: one case (red trace) was conducted in free-running mode, with no operative stabilizations, and a second one was performed in fully stabilized condition (blue trace).
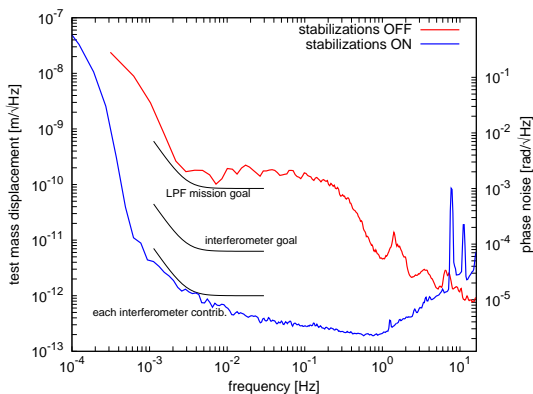
Figure 75: Measured OLG of the laser frequency stabilization.

It can be seen that the sensitivity of interferometric length measurements conducted with laboratory equipment can be improved by over a factor 200 with fully operational control loops, described above.

As mentioned before, the LTP OB is equipped with QPDs at the interferometer outputs, in order to measure the test mass attitude and interferometer alignment signals. To this end, the phase data measured at the channels of a QPD are processed with a DWS algorithm, as explained in Section 1.2, by the LTP interferometric data processing according to Equations 7.23 and 7.24. Figure 76 shows the LSD of the DWS measurements in the horizontal (φ) and vertical (η) axes for the two test mirrors used as test masses in the laboratory.

It can be seen that the noise levels of the interferometric length and angular measurements meet with margin the required budgets of $6.3\,\mathrm{pm}/\sqrt{\mathrm{Hz}}$ and $20\,\mathrm{nrad}/\sqrt{\mathrm{Hz}}$ in the frequency range of $3-30\,\mathrm{mHz}$.

Chapter 8

111
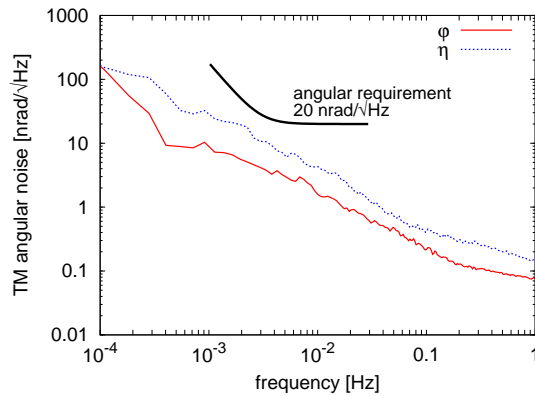
Figure 76: Noise level of the DWS angular measurement of the test mass.

The following section introduces the modifications made to the test bed for testing engineering models of the RLU and LMU, and the performance and interferometric sensitivity achieved with these units.

8.4 test facility for engineering and flight models

A facility for testing of engineering and flight hardware of LTP OMS units has been setup, starting with engineering models of the optical bench (OB) and modulation bench, which consists of the reference laser unit (RLU), and laser modulator unit (LMU). This test facility will be expanded upon availability of additional units and is intended for the assessment of the functionality and noise level during long-term measurement runs.

The breadboard modulation bench for laboratory experiments (see Figure 69) was replaced by the RLU and LMU engineering models shown in Figure 77.

In order to operate these units, Kayser-Threde Munich (KTM) – the industrial partner in charge – provided the necessary electrical ground support equipment (EGSE) (Figure 78), consisting of an electronics rack and a PC equipped with the appropriate interfaces to drive the equipment, in particular a MIL-STD-1553 card running the standard communication protocol defined for LISA Pathfinder.

(a)   (b)
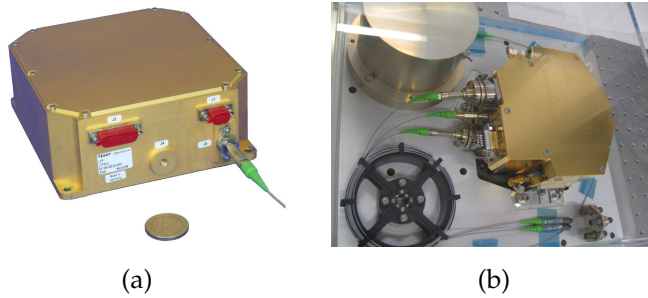
Figure 77: (a) Photograph of the LTP reference laser unit (RLU) engineering model.
(b) Photograph of the LTP laser modulator unit (LMU) engineering model.

Upon testing functionality of the units, the main aim was to conduct a long-term interferometric length measurement with operating control loops for OPD, laser power and frequency stabilizations, in order to reach the required readout sensitivity in the TM 1 and TM 1-TM 2 interferometers [52]. To this end, an additional vacuum vessel was procured for proper handling of the EM units (see Figure 79).

Fiber optics are used as interface between the tanks to transfer the two frequency-shifted beams obtained from the LMU into the OB. In LTP, these stabilizations use the phase measured at the reference and frequency interferometers obtained from the phasemeters, whose output data is processed by the DMU to compute the digital control signals, as illustrated on Figure 80.

The corresponding actuators are integrated in the EM and FM units such that they can only be driven over a digital-to-analog converter (DAC) that responds to the digital commands sent by the DMU through the MIL-STD-1553 interface. Due to the fact that a DMU prototype was not available at the moment, AEI and KTM with support of the Technische Universität München (TUM) implemented a workaround solution in the test setup by replacing the DMU with the AEI FPGA-based phasemeter prototype, and analog phasemeters (electronic mixers) to obtain the phase information (Ψ_R and Ψ_F in Equations 7.19 and 7.20, respectively) at higher rates ($\gtrsim 100\,\mathrm{Hz}$) as input signals for digital closed-loop controls running in a real-time signal processing system in charge of commanding the actuators in the laser assembly (LA) – RLU and LMU – over the MIL-STD-1553 interface.

Chapter 8

113
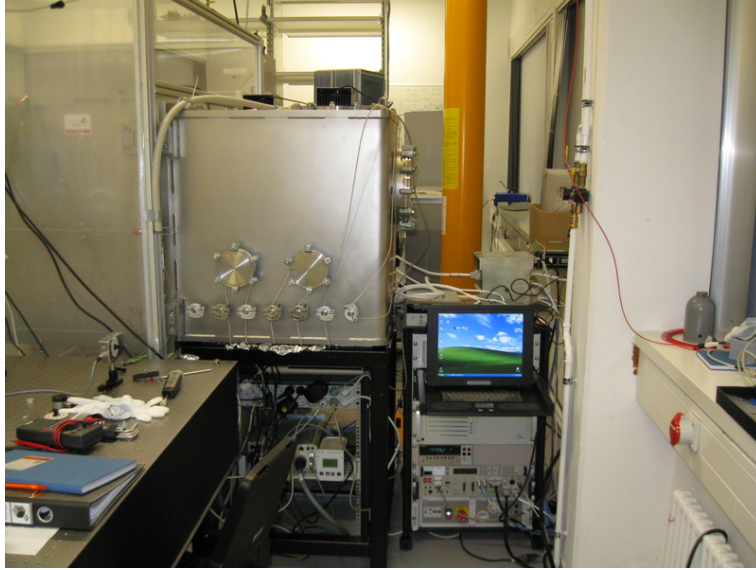
Figure 78: Photograph of the electronics rack and computer to operate the RLU and LMU engineering models.

A simplified functional description of this setup is given by the scheme in Figure 81.

Due to the modular implementation of the actuators in the LA units, the stabilizations treated here have been split in four separate digital filters:

- OPD stabilization: uses as input the phase signal Ψ_R and consists of one digital filter and DAC commanding a free-beam PZT-mounted mirror.

- Laser frequency stabilization: uses as input the phase signal Ψ_F and is split in two filters

    - Slow frequency: one filter controlling the temperature of the laser crystal.
    - Fast frequency: one filter driven a PZT acting on the laser crystal to correct faster fluctuations.

- Laser power: uses as input the signals from the photodetectors PDA1 and PDA2. One additional digital filter is used to suppress ***slow power***
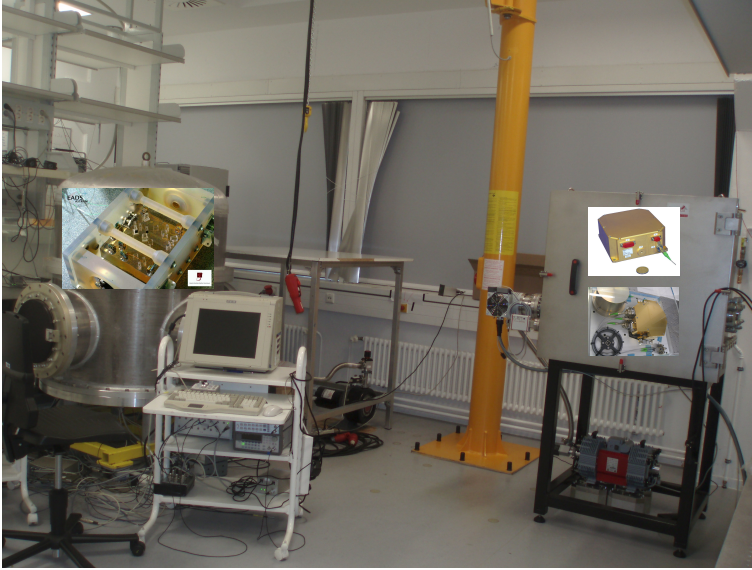
Figure 79: Test facility for engineering and flight hardware in the LTP laboratory at AEI.
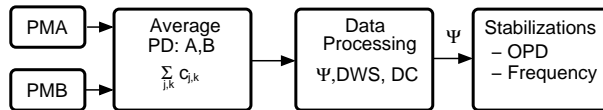
Figure 80: Phasemeter output data processing chain in the DMU.

variations in the millihertz range. As mentioned in Section 8.2.1, laser power noise around the heterodyne frequency (~ 1 kHz) would also affect the phase measurement. In order to stabilize these fast fluctuations, it is necessary to run an analog control loop, similar to the one previously presented in Figure 72.

Chapter 8
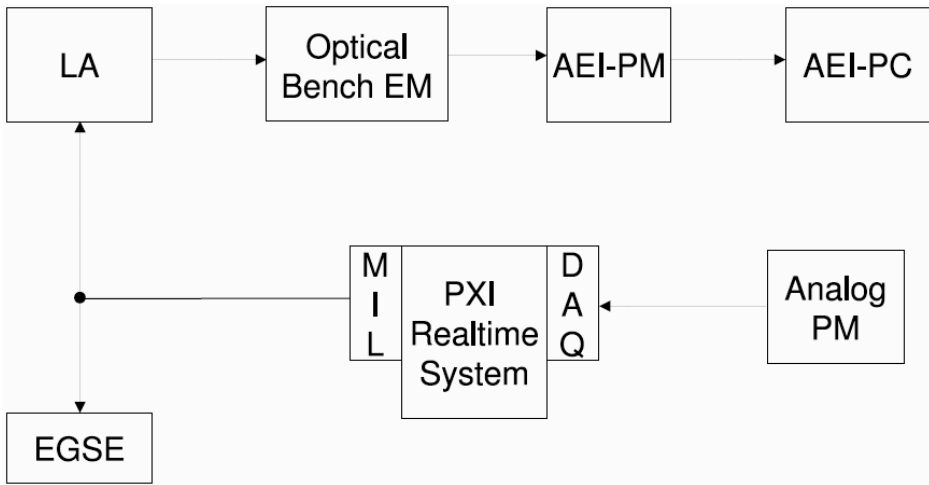
Figure 81: Simplified functional description of the laboratory set-up for closed-loop control tests with the RLU and LMU EMs. LA: Laser assembly engineering model. AEI-PM: AEI FPGA-based phasemeter prototype. AEI-PC: computer in the AEI LTP laboratory. AP: analog phasemeter. EGSE: electrical ground support equipment computer. DAQ: data acquisition system sampling the output of the analog phasemeters. MIL: MIL-STD-1553 interface card to LA and EGSE

8.4.1 *Definition and implementation of digital control loops*

Each of the four digital LTP OMS control loops (fast frequency, slow frequency, OPD and slow power) is implemented as a digital infinite impulse response (IIR) filter, which can be generically described by the following equation:

$$y_i = a_0 \, (x_i + \Delta x) + a_1 \, (x_{i-1} + \Delta x) + \cdots$$

$$b_1 \, (y_{i-1}) + b_2 \, (y_{i-2}) + \cdots \tag{8.2}$$

which means that the output y_i can be iteratively computed from the present and previous inputs (x_i, x_{i-1}, ...) and outputs (y_{i-1}, y_{i-2}, ...). Δx is a programmable offset to the error point resulting in a shift of the stabilized error point. The coefficients a_i and b_i determine the filter response. The output y_i is typically a floating number, which has to be scaled to integer values for the DACs driving the actuators.

The integer conversion of the floating number filter outputs is scaled, according to the following equation:

$$i_i = \alpha + \beta y_i \tag{8.3}$$

The digital control loop is fully characterized by these coefficients a_i, b_i, α, β, Δx, which are precomputed on ground and stored in the DMU for the LTP onboard implementation.

The coefficients α and β are chosen for an optimal utilization of the DAC dynamic range. The controller processes the corresponding input error signal (Ψ_R, Ψ_F, or PDA1/2) with an IIR filter to a digital feedback signal that is finally sent to the actuators in the LA.

The frequency plan in LTP has been designed such that the DMU computes the interferometric phase data (Ψ_R, Ψ_F) and the digital feedback signals for the LA stabilizations at a rate of 100 Hz. The absence of a DMU or similar individual equipment capable of the phasemeter back-end processing and communication with the LA units via the MIL-STD-1553 interface, forced a workaround strategy that includes the interaction of the AEI prototype phasemeter with a set of electronic mixers – working as analog phasemeters –, whose outputs are sampled by an ADC integrated into a real-time signal processing system. The four IIR filters for the digital control loops were programmed into the real-time system, which

Chapter 8

is also equipped with a MIL-STD-1553 interface to command the DACs, driving the actuators in the LA.

Figure 82 illustrates the complete setup with analog phasemeters and digital control loops implemented as IIR filters in the real-time system software, according to the DMU software specifications [51].
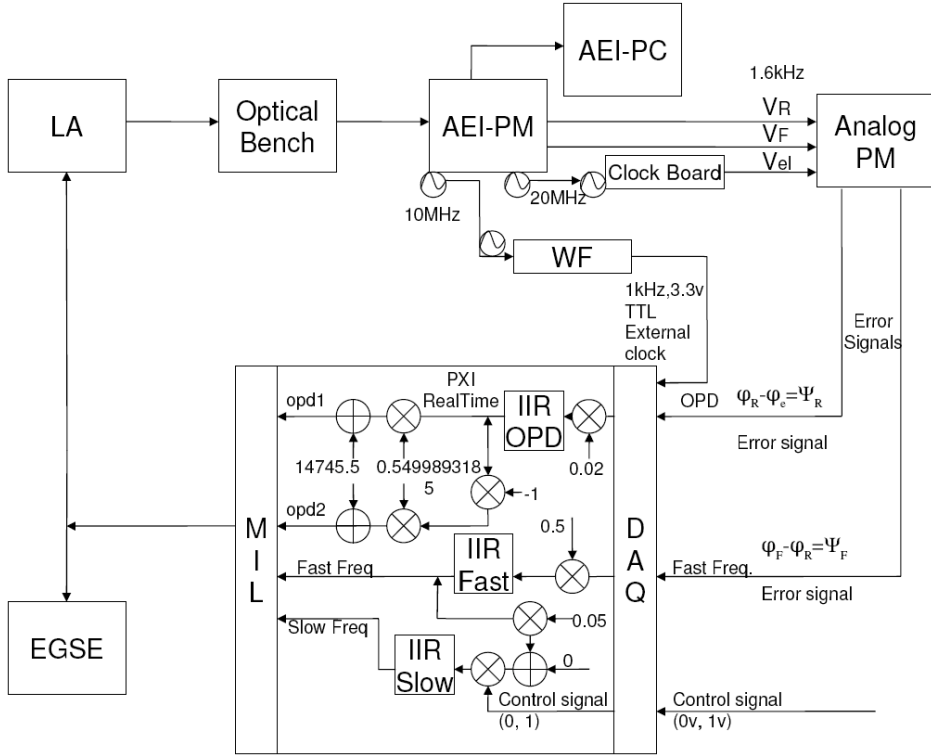
Figure 82: Complete functional description of the laboratory set-up with analog phasemeter and control loops.

8.4.2 OPD digital filter design

Initially, the available information about the system is limited, and therefore a conservative non-optimal controller is designed to ensure lock acquisition. Once

this is achieved, the OLG can be measured in order to characterize the complete control loop and improve its design for optimal noise suppression and stability.

Figure 83 presents the initial controller design and the associated IIR filter, obtained as the result of fitting the filter coefficients to the preset transfer function, using the software tool LISO [53].
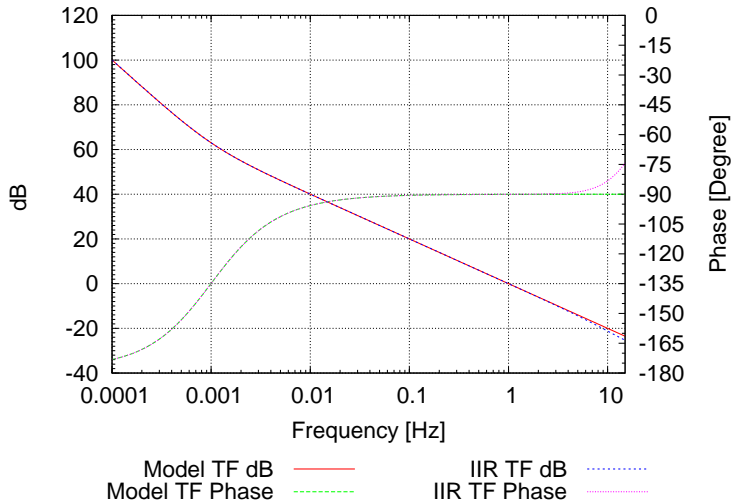
Figure 83: OPD initial filter design and corresponding IIR filter with matching frequency response.

In order to measure the OPD OLG, the analog error signal in the setup is used as depicted in Figure 84, maintaining the closed-loop control and injecting a sinusoidal excitation over one input of an adder to obtain the transfer function between its output and second input.

Figure 85 shows the measured OLG with the system locked using the controller from Figure 83.

Once the behavior of the closed-loop system was characterized, it was possible to do a targeted optimization of the IIR filter design, which is shown in Figure 86.

Chapter 8
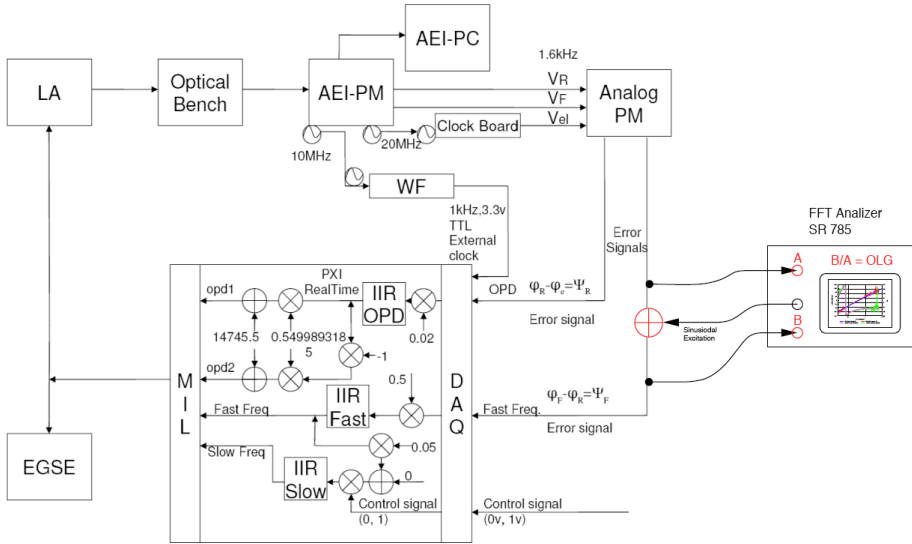
Figure 84: Method to measure the OLG in the present setup using analog signals (Note that the measurement of the frequency loop OLG is depicted for clarity).
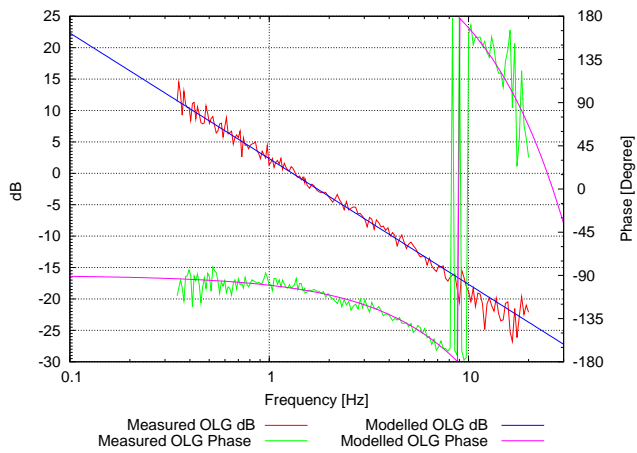
Figure 85: OPD OLG measurement once the system is locked with the initial filter design.

Figure 87 shows the measured OLG of the optimized OPD control loop that evidences a higher gain and bandwidth.
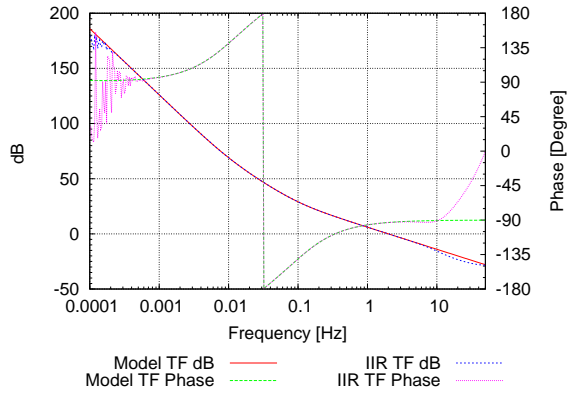
Figure 86: OPD optimized filter design and corresponding IIR filter with matching frequency response
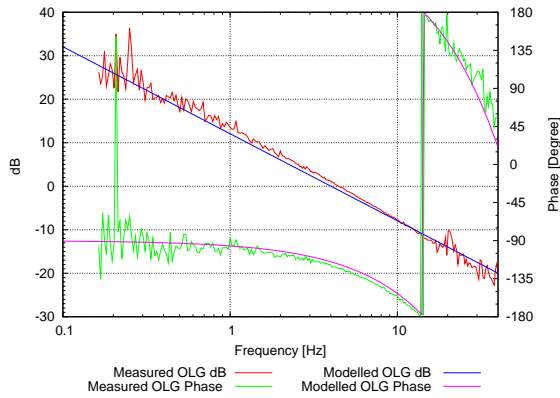
Figure 87: OPD OLG measurement with the optimized filter design.

8.4.3 *Frequency control loop*

A similar procedure was followed to design the controllers for the fast and slow frequency loops.

The transfer function of the controller designed for the fast frequency control loop and the frequency response of its associated fitted IIR filter implemented in the real-time system are shown in Figure 88.
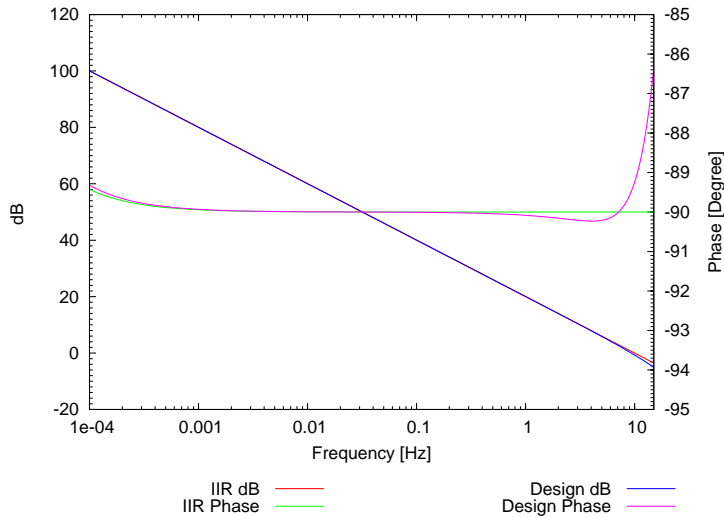
Figure 88: Fast frequency filter design and corresponding IIR filter with matching frequency response

Figure 89 shows the transfer function of the designed filter for the slow frequency loop and the matching transfer function of the IIR filter.

According to the method of Figure 84, the OLG transfer function of the total laser frequency control loop with optimized parameters was measured. The result is shown in Figure 90.

Again for this case, the IIR filter coefficients were also fitted to the designed OLG, by using the software tool LISO for the computation.
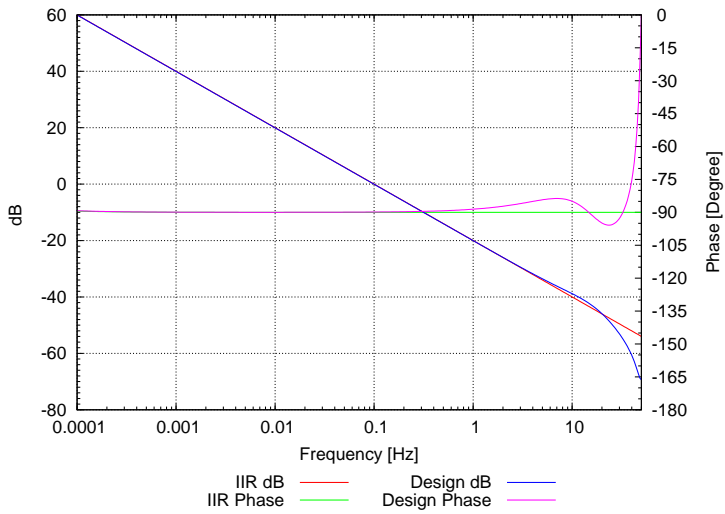
Figure 89: Slow frequency filter design and corresponding IIR filter with matching frequency response
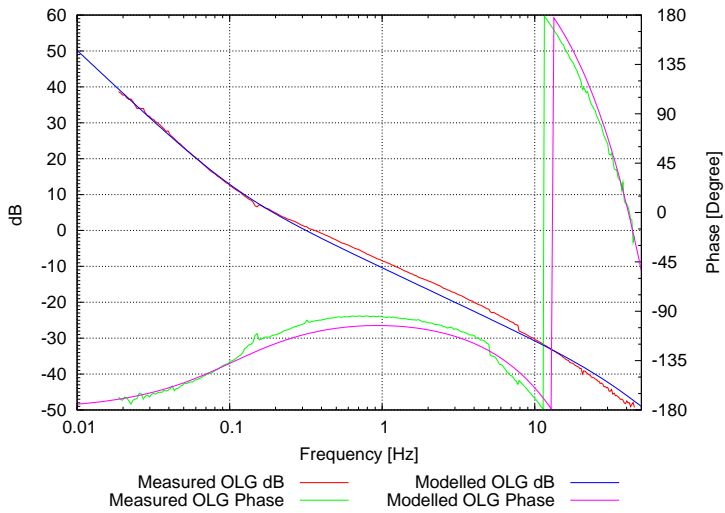
Figure 90: Frequency loop OLG measurement with the optimized filter design. Also plotted is the model for the OLG.

8.4.4 *Slow power loop*

In a similar way, the controller used for the slow power stabilization and its associated IIR filter were designed and implemented. The corresponding frequency response is shown in Figure 91. Once again, the functionality of the controller design was demonstrated by successful lock acquisition.
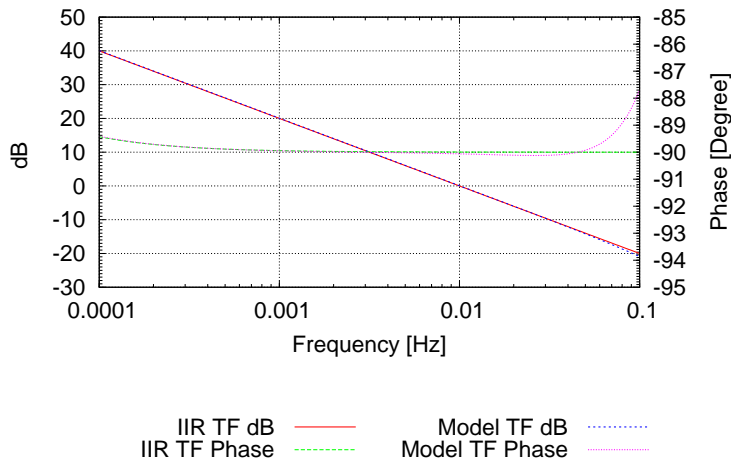
Figure 91: Frequency response of the controller design and corresponding IIR filter for the slow power loop.

8.5 LONG TERM PERFORMANCE

Once lock was acquired in all stabilizations and the noise suppression was optimized, the setup described in Figure 81 was used to conduct long-term measurements. The high precision phase readout from the AEI phasemeter was processed and recorded with the PC. These phase data streams were analyzed with the LTP data analysis tool (LTPDA) [54, 55], which is the official LISA Pathfinder mission analysis software. Figure 92 shows the LSD of the OMS sensitivity to position fluctuations of the dummy test mirrors that act as test

masses in the interferometric setup. The required interferometric sensitivity of $6.3\,\text{pm}/\sqrt{\text{Hz}}$ has been demonstrated using the engineering models of the LA and OB, operating with back-end processing driving the digital stabilizations.
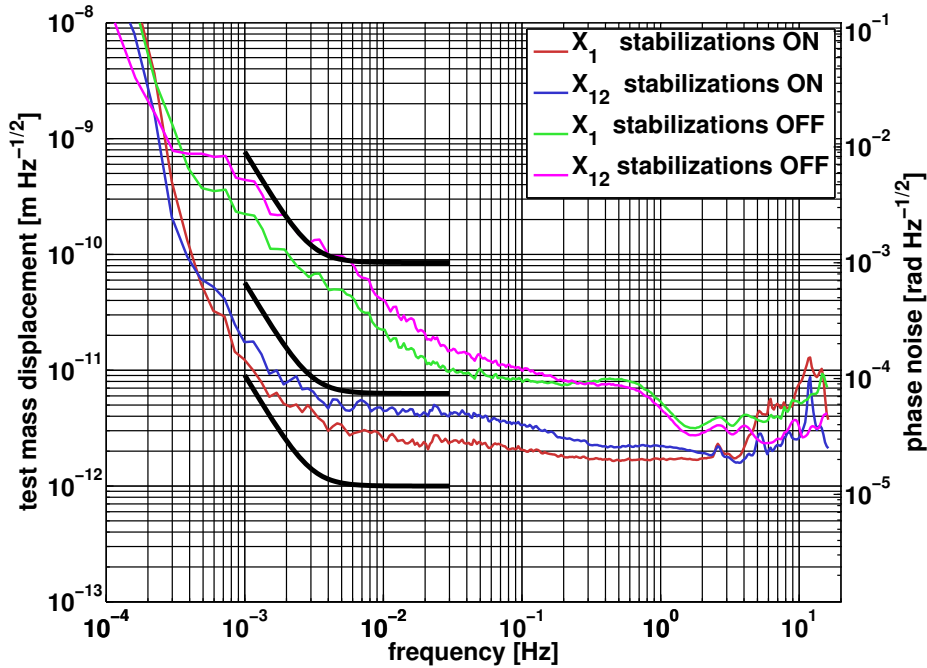
Figure 92: Sensitivity to test masses position fluctuations demonstrated with the LA EM.

An alternative data analysis method to correct excess noise in the phase measured at the interferometers TM 1 and TM 1-TM 2, which results from laser frequency and non-linear OPD fluctuations is presented in Chapter 9.

9

PERFORMANCE INVESTIGATIONS

This chapter presents the results of various experiments and analysis performed on the functionality and noise behavior of the LISA Technology Package (LTP) interferometry. Many of these techniques and results will also be applicable to LISA.

One of the investigated topics is the cross-talk between angular and displacement degrees of freedom, coming from test mass jitter due to the limited gain in their drag-free control system. This effect was simulated in hardware by movable test masses and it was possible to subtract the introduced excess noise in the longitudinal measurement by data analysis.

Further noise subtraction algorithms have been developed to correct for noise contributions in the interferometer generated by fluctuations of the laser frequency and optical pathlength difference.

Test samples of the LTP optical window, which is at the interface between optical bench and test masses, were interferometrically measured to assess the effect of different coatings on the interferometer performance.

A real-time wavefront detector, developed to help adequate beam preparation and evaluation of components [9, 10], has been utilized in the design and manufacture of the quasi-monolithic fiber injectors FIOS for the LTP optical bench and characterization of the LTP optical window. This device will also be employed in forthcoming investigations of key LISA components, such as the telescope and the initial acquisition sensor.

127

9.1 APPLICATION OF THE REAL-TIME WAVEFRONT DETECTOR

As shortly introduced in Chapter 2, an instrument capable of conducting a spatially resolving measurement in real-time of the differential wavefront resulting from the overlap of two laser beams has been developed[1] [9, 10] and has been subsequently applied for the characterization of key optical components on the LTP optical bench, such as the quasi-monolithic fiber injectors FIOS and the LTP optical window. The measurements presented here are the result of and were conducted as part of a unique research collaboration between AEI and the Institute for Gravitational Research (IGR) at University of Glasgow, which is the institution in charge of the development and manufacture of the LTP OB and FIOS flight models.

9.1.1 Characterization of the LTP fiber injectors

During the development of the FIOS, a series of measurements were conducted on test pieces with the aim of evaluating the obtained beam quality in a real optical setup, in order to fix the design. Part of the tests conducted was to measure the resulting phasefront in an interferometer, by using prototype lenses of similar optical properties to the specified for the FIOS FM.

The armlengths on the OB differ by approximately 35 cm on the main measurement interferometers ("1", "12", and R). This mismatch is compensated by the length of the fiber, delivering the frequency-shifted beams from the modulation bench into the optical bench. However, the parameters of the interfering beams are determined by the fiber injectors, and the curvature of their wavefront depends on the distance covered from the FIOS output to the interference point. In order to match the curvature of the two wavefronts, each fiber injector has to be custom-built, due to interferometer armlength difference. The baseline design [56] specifies the following characteristics fiber injectors

A table top interferometer with unequal armlengths similar to the LTP OB was setup, in order to measure the resulting phasefront from the interference of the beams. A schematic diagram of the test setup is shown in Figure 93[2].

The phasefront measured at this setup is shown on Figure 94. This measurement gives the resulting difference in geometry between the two interfering wave-

---

1 This instrument was developed by the author in his Master's thesis.
2 courtesy of the University of Glasgow

FIOS	radius of curvature of the lens	fiber-lens interspacing
1	14.58 mm	3.40 mm
2	14.58 mm	3.38 mm

Table 2: Baseline design for the LTP fiber injectors with a single lens.

(a)

(b)
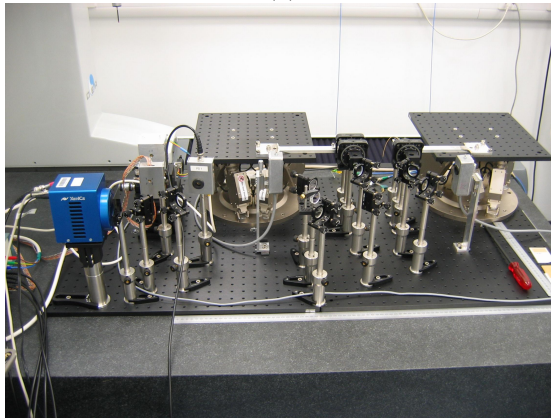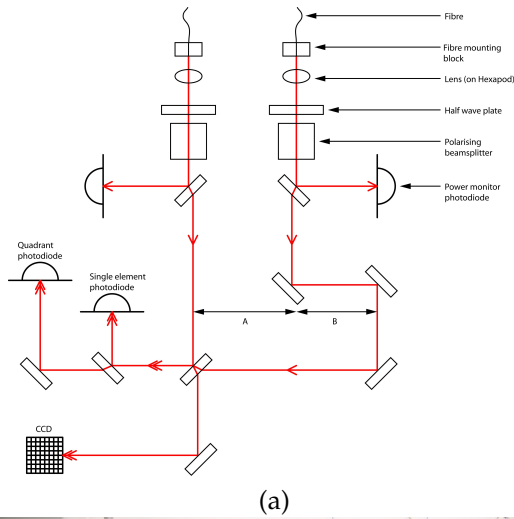
Figure 93: (a) Schematic diagram of the table top interferometer setup for the phasefront measurement with FIOS prototype test pieces. (b) Photograph of the setup.

129

Chapter 9

fronts for the nominal beam parameters and beam propagations in the optical bench.
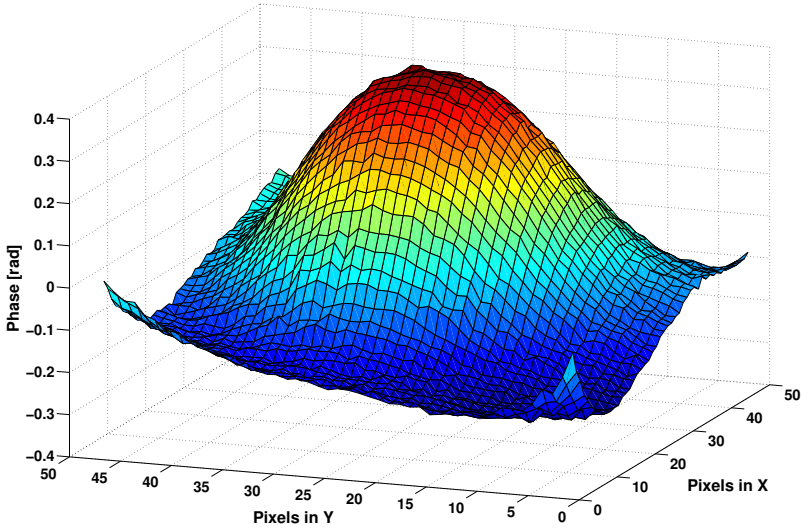
Figure 94: Measured phasefront at an interferometer with unequal armlengths and test pieces of similar optical properties to the specifications of the FIOS.

The table top setup was rebuilt for an interferometer with matched armlengths, in order to measure the phasefront characteristics for beams covering a similar distance. The result is shown on Figure 95.

A similar measurement was previously conducted at the frequency interferometer of LTP OB EM [9, 10] which has a small armlength difference on the optical bench of about 1 cm. Figure 96 shows the measured phasefront in this case as a comparison to the results obtained with a laboratory prototype configuration of the LTP FIOS FM.

The results shown on Figures 95 and 96 help to compare the beam quality between the LTP OB EM and the one expected on the LTP OB FM, since they were both measured at interferometers with arms of similar length.

The larger spatial inhomogeneities measured on the LTP OB EM can be attributed
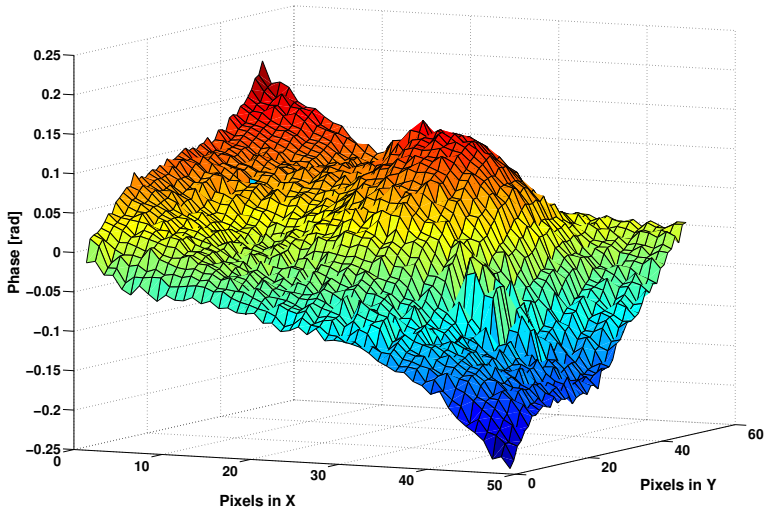
Figure 95: Measured phasefront at an interferometer with matched armlengths, using the same fiber injector configuration.
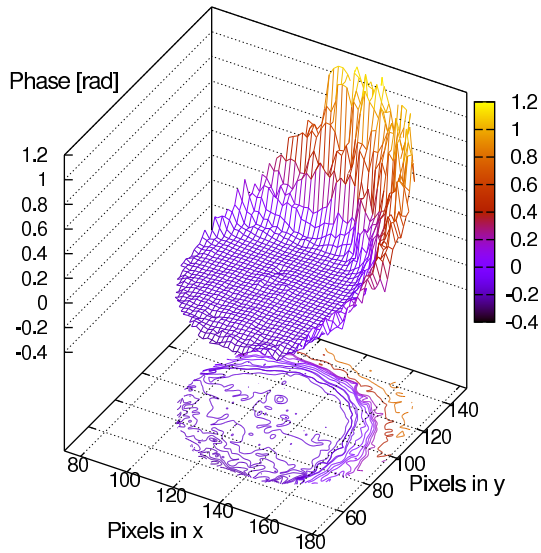
Figure 96: Phasefront measured at the frequency interferometer of the engineering model of the optical bench for LTP.

131

to non-optimal adjustment of the lenses in the two fiber injectors. During its manufacture, the beam quality was not so carefully considered as it is the case in the design and manufacture of the flight model optical bench. Large variations in the spatial distribution of the measured phase at the beam interference points, especially under the effect of beam pointing, due to angular test mass jitter, could significantly contribute to the noise level of the interferometric measurement. Thus, the availability of such a measurement device and the adequate measurement procedure to characterize these inhomogeneities is of importance for proper beam preparation in the manufacturing process of the LTP OB FM.

9.1.2 *Measurement of the LTP optical window*

The real-time wavefront instrument was also utilized to measure the optical window with high spatial resolution. The aim of this investigation was to quantify the effect of potential inhomogeneities in the material on the measured phase under the presence of beam jitter across the window. To this end, three samples made of the same material and with the same dimensions, were measured with the only difference on their optical coating properties: one of the samples was uncoated (pure substrate), a dielectric anti-reflection (AR) coating was applied on the second sample, and the third sample was prepared with a conductive Indium-Tin Oxide (ITO) coating additional to the dielectric AR coating. While it is very common to use AR-coatings in optics, in order to minimize spurious reflections and maximize transmission, conductive coatings usually degrade the optical properties. The reason for considering such a coating in the LTP interferometer is the fact that the window will experience electrostatic charging from the space environment, which could eventually compromise the operation of the LPF inertial sensors (test masses and electrode housing) by electrostatic interactions. The window is at the optical interface between the optical bench and the test masses and is rigidly attached to the vacuum enclosure, as shown in Figure 97.

In order to measure inhomogeneities of the optical window with high spatial resolution, a series of phasefront measurements[3] were conducted on these three window samples, by inserting them (one after the other) into one arm of the interferometer (see Figure 98).

---

3 The measurements were conducted in collaboration with the University of Glasgow, who had available the sample windows and the wavefront detector. The raw data were taken by J. Bogenstahl in Glasgow while the processing was done by the author.
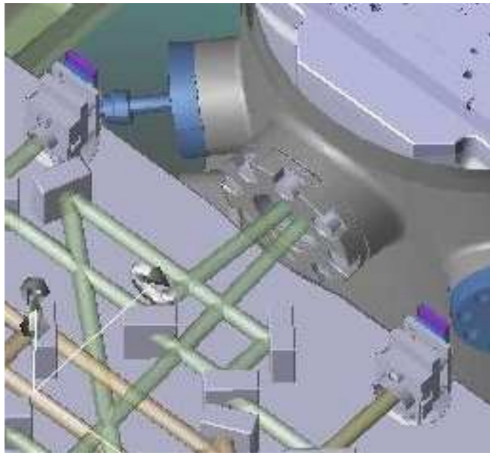
Figure 97: CAD model pointing out the location of the window in the optical path of the LTP interferometer.
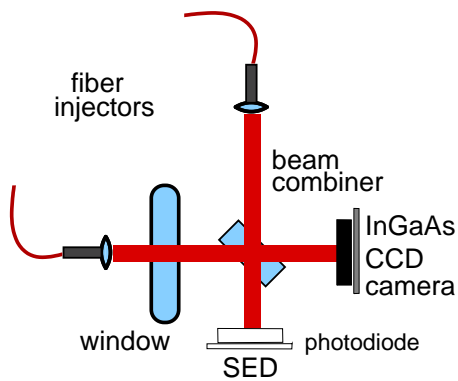
Figure 98: Interferometer setup for the spatially resolving measurement of the optical window by using the real-time wavefront detector.

133

A first null measurement was conducted on this interferometer prior to inserting a window sample, in order to obtain a reference phasefront that can be subtracted as background from the window measurements. Figure 99 shows the obtained reference phasefront. The results obtained from measuring the three
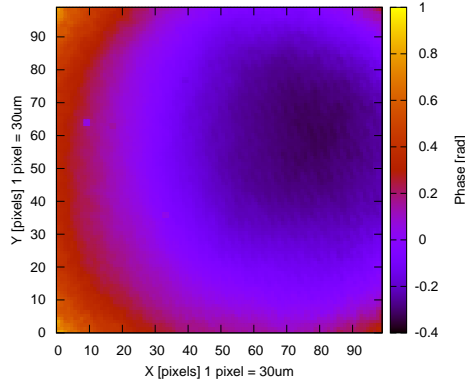
Figure 99: Reference phasefront obtained for the optical window measurements.

sample windows after subtracting the reference phasefront of Figure 99 are presented in Figure 100. The phasefront differences obtained from these mea-
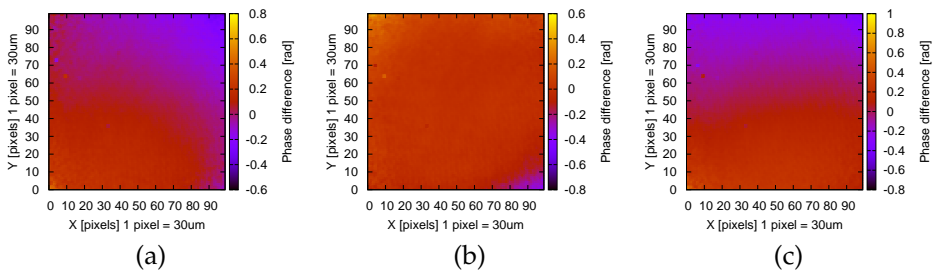
Figure 100: (a) Phase difference measured at the window substrate. (b) Phase difference measured at the AR-coated window. (c) Phase difference measured at the ITO+AR-coated window.

surements represent the spatially resolved effect of the inhomogeneities in the window and its corresponding coating on the phase measurement. However, it is necessary to properly weight this phase information with the correct Gaussian

intensity distribution of the laser beam passing through the window. To this end, the measured phase difference distributions have to be processed by the two-dimensional convolution of each phasefront with the adequate two-dimensional Gaussian filter kernel. This two-dimensional filtering method is also known in image processing as Gaussian blur filter. The Gaussian filter kernel is given by the parameters of the beam passing through the window, which in the case of the LTP OB FM design corresponds to a beam radius $\sigma = 554\,\mu$m at the second optical window (WIN 2) in front of test mass 2 (see Figure 64 (b)). This window has been taken as reference point in the interferometer, because beam pointing onto WIN 2 caused by residual angular noise from test mass 1, will produce the strongest effect due to the long lever arm of approximately 30 cm (optical path) between TM 1 and WIN 2. The filter kernel has been normalized to a total power of 1 and can be computed as

$$\Gamma(x,y) = \frac{1}{2\pi\sigma^2}\, e^{-\frac{(x-x_o)^2+(y-y_o)^2}{2\sigma^2}}, \tag{9.1}$$

where the coordinates (x_o, y_o) denote the center of the Gaussian distribution, and σ corresponds to the beam radius at the WIN 2. Figure 101 shows the generated kernel for this analysis.
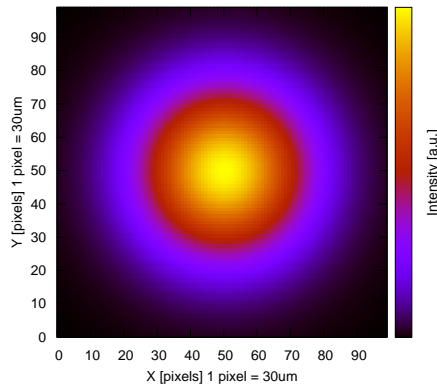
Figure 101: Computed kernel for the two-dimensional Gauss blur filter.

The Gauss blur filter can be applied to the measured phase differences by com-

135

puting the discrete two-dimensional convolution between each phase difference distribution and the Gaussian filter kernel, an can be obtained as

$$\Lambda(x,y) = \sum_{i}^{nx} \sum_{j}^{ny} \Phi(i,j) \cdot \Gamma(x-i, y-j) \,, \tag{9.2}$$

where $\Lambda(x,y)$ is the result obtained from filtering the image $\Phi(i,j)$ of $nx \times ny$ pixels corresponding to the measured phasefront distributions shown in Figure 100. Figure 102 shows the obtained filtered phasefronts for the three window samples.
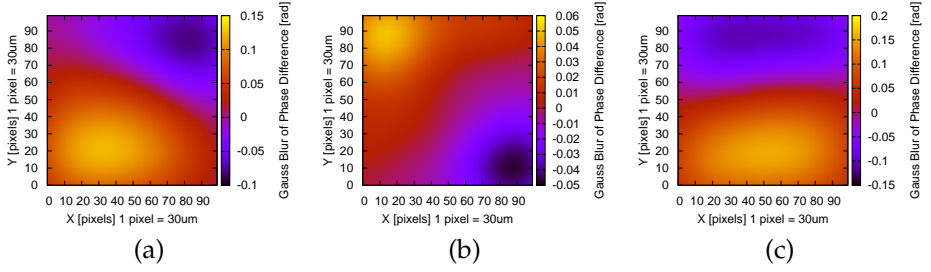
Figure 102: (a) Gauss blur of the phasefront measured at the window substrate. (b) Gauss blur of the phasefront measured at the AR-coated window. (c) Gauss blur of the phasefront measured at the ITO+AR-coated window.

In addition, the maximum $\Theta(x,y)$ of the two-dimensional gradient (∇_x, ∇_y) of the filtered phasefronts is computed, in order to determine the maximum spatial phase fluctuations obtained in each of the three measured sample windows.

$$\Theta(x,y) = \sqrt{\nabla_x^2(x,y) + \nabla_y^2(x,y)} \,, \tag{9.3}$$

where

$$\nabla_x(x,y) = \frac{\Lambda(x+1,y) - \Lambda(x-1,y)}{2h} \tag{9.4}$$

$$\nabla_y(x,y) = \frac{\Lambda(x,y+1) - \Lambda(x,y-1)}{2h} \tag{9.5}$$

$$\tag{9.6}$$

are the corresponding directional derivatives in the horizontal x and vertical y axes, and $h = 30\,\mu m$ is the pixel pitch of the spatially resolving photodetector

(CCD camera). Figure 103 presents the resulting phase gradient distributions $\Theta(x, y)$. Assuming that the spatial inhomogeneities of the windows are station-
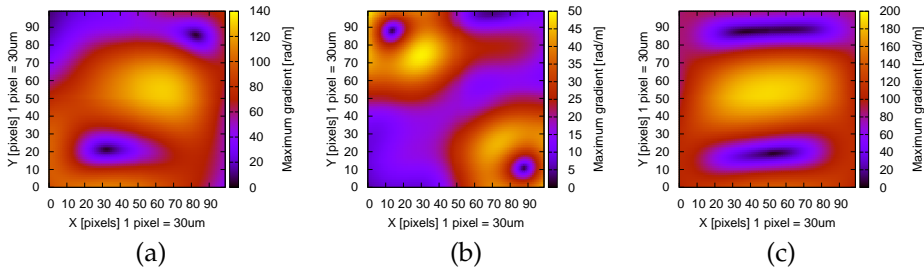
Figure 103: (a) Gradient of the filtered phasefront measured at the window substrate.
(b) Gradient of the filtered phasefront measured at the AR-coated window.
(c) Gradient of the filtered phasefront measured at the ITO+AR-coated window.

ary and the position of the laser beam on the optical window does not change in time, the net effect of the measured phasefront distortions would only be a constant phase shift in the longitudinal phase measurement of the test masses, which does not contribute to the noise level of the measurement. However, limited gain in the LTP drag-free and attitude control system (DFACS) results in residual test mass angular noise that produces excursions of the beam over the surface of the optical window, due to this beam pointing, and additionally generated excess noise in the longitudinal phase measurement due to the cross-coupling between the longitudinal and angular degrees of freedom. The latter point is discussed in detail in Section 9.2.

It is possible to estimate the maximum effect on the longitudinal phase caused by phasefront distortions introduced by inhomogeneities of the material and coatings of the optical window under the presence of beam pointing. To this end, the expected test mass residual angular noise [57] (see Figure 110) was scaled by the lever arm of approximately 30 cm (optical path) between TM 1 and WIN 2 in order to project the maximum value of the phase gradient distribution Θ_{max} as a noise contribution on the measured longitudinal phase. The estimated values of Θ_{max} for each of the three cases are listed in Table 3. The noise projections for the windows are the lower three plotted curves on Figure 105. In addition, a direct experimental investigation of the influence of test mass jitter in conjunction

137

Chapter 9

Optical Window	$\Theta_{\max}$ [rad/m]
substrate	130.4
AR-coating	49.1
ITO+AR-coating	189.5

Table 3: Maximum phase gradients obtained for each of the three samples of the LTP optical window.

with coated windows was performed. A sample of an optical window with ITO+AR-coating, which was additionally exposed to γ-radiation[4] at the level of 30 krad, was introduced in the LTP OB EM interferometer (see Figure 104) for test mass readout sensitivity measurements (similar to the measurements presented in Chapter 8).
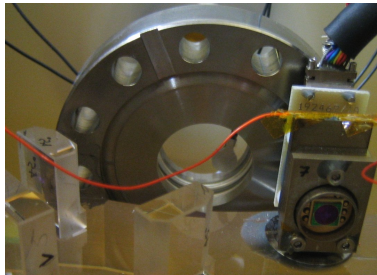
Figure 104: Optical window sample with ITO+AR-coating inserted in the LTP OB EM for interferometric test mass readout sensitivity measurements.

For this measurement, the expected residual test mass angular noise was injected into PZT-actuated test masses, replacing the Zerodur® static mirrors used for previous measurements. The injection of angular noise into the PZT-actuated test masses, the cross-coupling of angular and displacement degrees of freedom, and a noise subtraction technique to counteract its effect are described in detail in Section 9.2. Figure 105 shows the noise projections of the estimated inhomogeneity effects of the three sample windows analyzed in this section. The interferometric measurement of the irradiated ITO+AR-coated window is also included in the

4 The sample window was irradiated using a ^{60}Co γ source at ESA-ESTEC thanks to Zoran Sodnik.

plot together with the corresponding corrected LSD trace, where the coupling of the angular noise into the longitudinal measurement was subtracted. It can
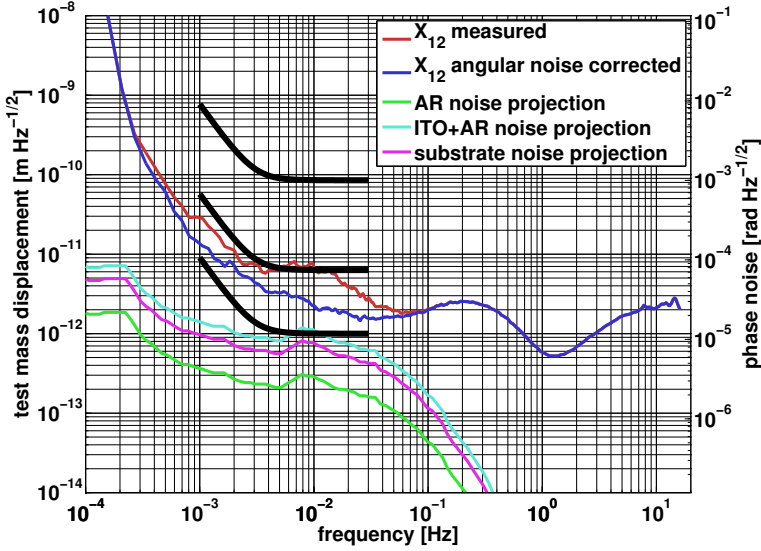
Figure 105: Red: sensitivity of the longitudinal phase readout when injecting TM angular noise. Blue: sensitivity of the corrected longitudinal phase after the angular noise subtraction. Green: projection of phase noise estimated from phasefront distortions at the AR-coated window. Cyan: phase noise projection for the ITO+AR-coated window. Magenta: phase noise projection for the window substrate.

be seen from this plot that the estimated phase noise contributions from the inhomogeneities in the window (traces green, cyan, and magenta) are in the worst case at approximately $1\,\mathrm{pm}/\sqrt{\mathrm{Hz}}$. The real interferometric measurement under the influence of test mass jitter (red trace) evidences excess noise that has been determined to come from the cross-coupling between angular and displacement degrees of freedom, and can be corrected (blue trace) by the angular noise subtraction algorithm that is presented in Section 9.2. Hence, material and coating inhomogeneities measured at representative prototypes of the LTP optical window are not expected to be a limiting factor to the interferometer sensitivity, also in the case of the recently defined baseline configuration of the conductive ITO+AR coating.

139

9.2 RESIDUAL TEST MASS ANGULAR NOISE

In order to investigate the effect of test mass residual angular noise into the longitudinal measurement, the Zerodur$^{®}$ static mirrors were substituted by PZT actuated mirrors, which are shown in Figure 106.

Figure 106: Comparison between PZT actuated mirrors (left) and static test mirrors (right).

Figure 107 illustrates the mounting of the static mirrors (a) and the PZT-actuated mirrors on the optical bench.

(a)   (b)
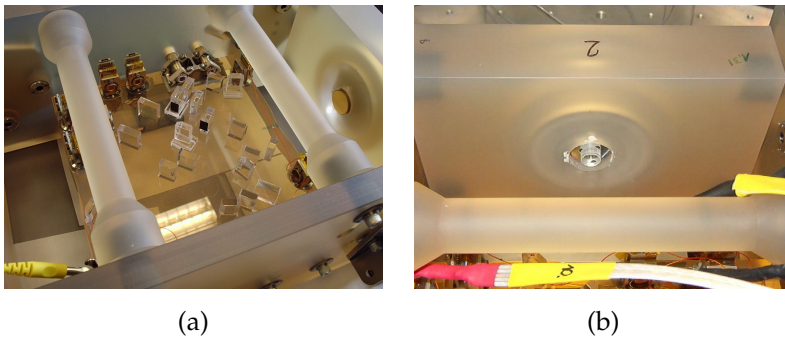
Figure 107: (a) Mounting of static test mirrors on the optical bench. (b) Mounting of PZT-actuated mirrors on the optical bench.

In particular, the mechanical stability of the PZT elements together with the mirrors glued on them was of importance for this investigation that relied on it being similar to the the static mirrors in order avoid excess noise that would prevent this assembly to meet the LTP longitudinal and angular requirements.

Figure 108 shows a comparison between the sensitivity spectra measured for the longitudinal TM displacement Ψ_1 and Ψ_{12} with Zerodur® static mirrors and with forward-biased PZT-actuated mirrors in static condition (applied DC voltage of about $3-5\,\mathrm{V}$).
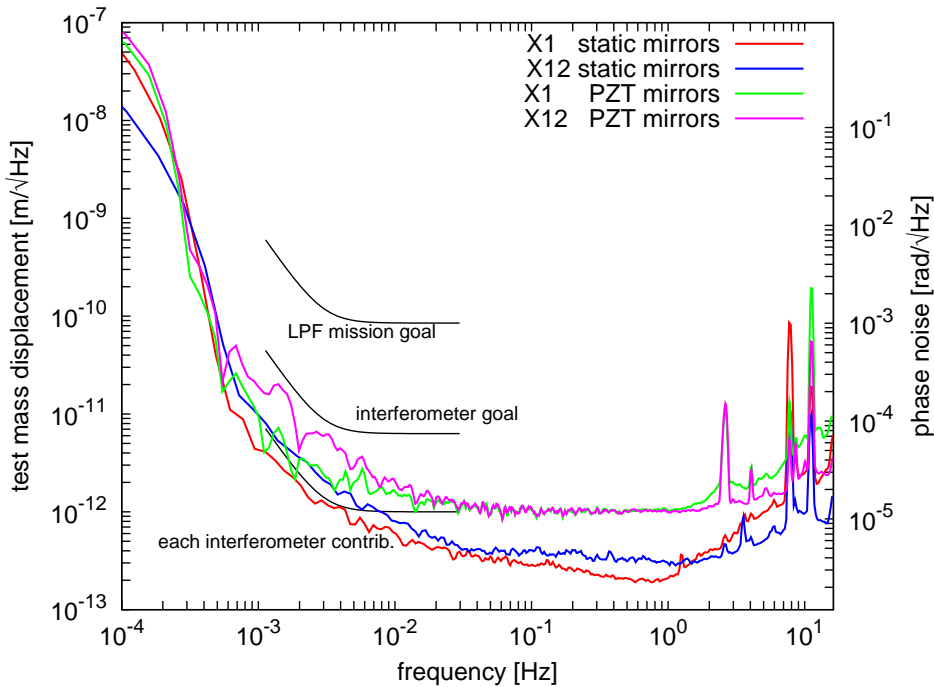
Figure 108: Sensitivity spectra of longitudinal phase measurements performed with static test mirrors and with PZT actuated mirrors.

It can be seen that all sensitivity curves remain below the required $6.3\,\mathrm{pm}/\sqrt{\mathrm{Hz}}$ in the measurement band (interferometer budget). Figure 109 shows the horizontal ($\varphi_{1,12}$) and vertical ($\eta_{1,12}$) angular resolution spectra achieved with forward biased PZT mirrors in static condition, which is better than the required

$20\,\mathrm{nrad}/\sqrt{\mathrm{Hz}}$ TM jitter in the measurement band.
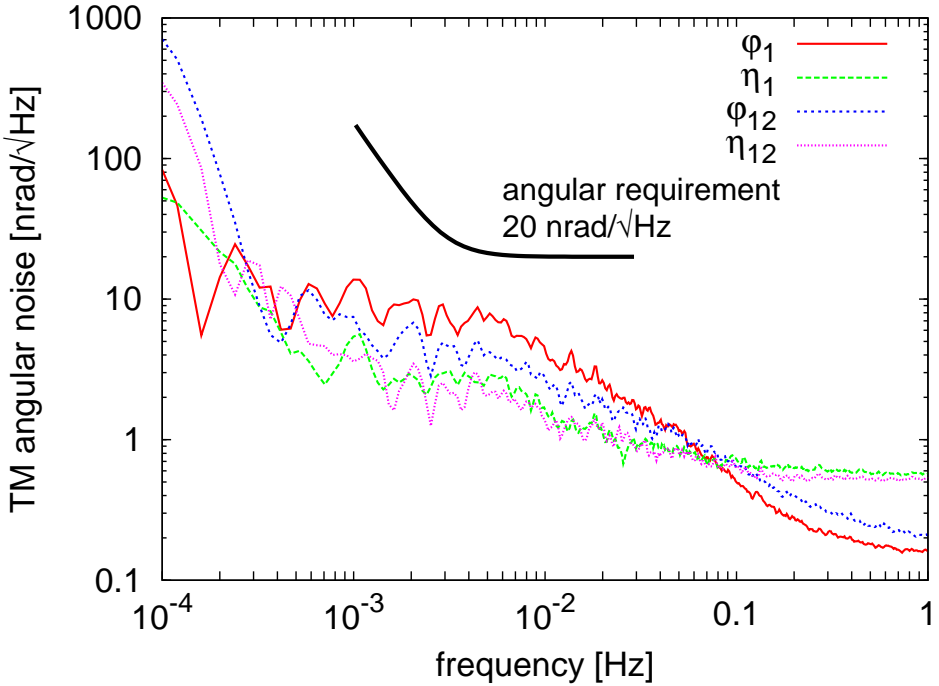
Figure 109: Sensitivity spectra of angular measurements with PZT actuated mirrors.

Simulations conducted on the TM dynamics under the currently designed DFACS control led to spectral predictions of the residual TM angular noise [57] that can be expected in orbit, during high sensitivity science mode operations in the LISA Pathfinder mission.

From this information, time series that matches this spectral behavior were generated with a numerical method [58] and injected into the PZT actuated mirrors via a DAC. Figure 110 shows the simulated angular noise spectra ($\varphi_{1,12}$ and $\eta_{1,12}$), and the corresponding TM angular noise spectra read out by the interferometer DWS signals.

Due to limited accuracy alignment of the laser beam onto the TM center of
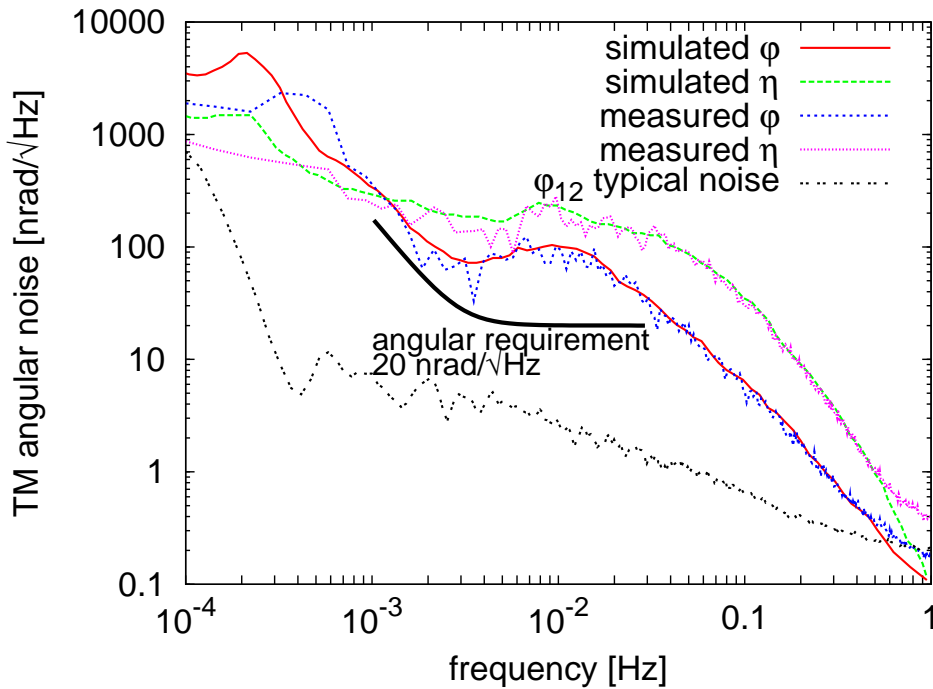
Figure 110: Expected injected residual TM angular noise for on-orbit operation and interferometric measured angular noise of the test masses.

rotation, the resulting cross-coupling from TM angular noise into the TM longitudinal displacement readout introduces excess noise into the measurement of TM position fluctuations, thus spoiling the sensitivity of the optical readout.

The aim of this investigation was to characterize this cross-coupling and to determine the corresponding coupling factors that translate this angular motion of the TM into an apparent longitudinal TM displacement. This was done by fitting the DWS measurements to the longitudinal time series with a linear least squares algorithm, as described below.

Once these coupling factors have been estimated, the excessive noise can be subtracted from the main longitudinal data stream.

143

9.2.1 *Fit algorithm*

The longitudinal raw measurements Ψ_1 and Ψ_{12} depend on the TM angular motion $\varphi_{1,12}$ and $\eta_{1,12}$

$$
\begin{aligned}
\Psi_1^{meas} &= \Psi_1^{true}(t) + \Psi_1^{comp}\left(\varphi_1, \eta_1\right) & (9.7) \\
\Psi_{12}^{meas} &= \Psi_{12}^{true}(t) + \Psi_{12}^{comp}\left(\varphi_1, \eta_1, \varphi_{12}, \eta_{12}\right). & (9.8)
\end{aligned}
$$

As it can be seen in Figure 110, the SNR of the measured DWS signals motion is much higher within the LTP observation band ($3\,\text{mHz} - 30\,\text{mHz}$) than at higher frequencies.

Under normal laboratory conditions, the effect of fast electronic and mechanical noise in the higher frequency band (approximately above $100\,\text{mHz}$), as well as long-term thermal drifts at frequencies below $1\,\text{mHz}$ dominate the time evolution and behavior of the longitudinal and angular interferometric signals. Hence, the information of the TM angular noise vanishes in the noise level of the measured time series. A significant correlation exists only in a limited frequency band.

In order to overcome this limitation, a second order band-pass filter in the frequency rage[5] $3\,\text{mHz} - 30\,\text{mHz}$ was applied to each longitudinal (Ψ_1^{bp} and Ψ_{12}^{bp}) and angular ($\varphi_1^{bp}, \eta_1^{bp}$ and $\varphi_{12}^{bp}, \eta_{12}^{bp}$) time series within the LTP observation band. This way, it is possible to precisely characterize the cross-coupling process of the TM angular motion into the longitudinal interferometric readout.

The dependence of the filtered longitudinal measurements Ψ^{bp} with respect to the filtered angular signals φ^{bp}, η^{bp} can be rephrased as

$$
\begin{aligned}
\Psi_1^{bp} &= \Psi_1\left(\varphi_1^{bp}, \eta_1^{bp}\right) & (9.9) \\
\Psi_{12}^{bp} &= \Psi_{12}\left(\varphi_1^{bp}, \eta_1^{bp}, \varphi_{12}^{bp}, \eta_{12}^{bp}\right). & (9.10)
\end{aligned}
$$

Detailed optical simulations [59] indicate a nonlinear coupling mechanism of parabolic type, but have also shown that for the noise levels occurring in our

---

5 This frequency range was later on expanded to $0.4\,\text{mHz} - 500\,\text{mHz}$ that copes with the noise subtraction technique presented in Section 9.4.

experiment, a linear model is sufficient. A general model for this approach can be described by the following linear system of equations:

$$\Theta \cdot \kappa = \Psi, \tag{9.11}$$

where Θ is the design matrix for our fitting problem (angular data φ^{bp}, η^{bp}), κ is a vector containing the coupling factors we are looking for, and Ψ is a vector corresponding to the time series of our target function (longitudinal TM data Ψ^{bp}).

The dimensions of Θ are $N \times m$, where N is the length of the time series and m is the number of input time series to be used. In the case of the TM 1 interferometer $m = 2$ ($\varphi_1^{bp}, \eta_1^{bp}$), and for the TM 1-TM 2 interferometer $m = 4$ ($\varphi_1^{bp}, \eta_1^{bp}, \varphi_{12}^{bp}, \eta_{12}^{bp}$). κ is a vector with dimensions $m \times 1$, and Ψ is a vector with dimensions $N \times 1$.

In this specific case, the following system of equations is obtained for the TM 1 interferometer:

$$\Psi_{N \times 1}^1 = \Theta_{N \times 2}^1 \cdot \kappa_{2 \times 1}^1, \tag{9.12}$$

with

$$\Theta^1 = \left(\begin{array}{cc} \varphi_1^{bp} & \eta_1^{bp} \end{array} \right) \text{ and } \kappa^1 = \left(\begin{array}{c} \kappa_0^1 \\ \kappa_1^1 \end{array} \right). \tag{9.13}$$

The system of equations for the TM 1-TM 2 interferometer can be expressed as:

$$\Psi_{N \times 1}^{12} = \Theta_{N \times 4}^{12} \cdot \kappa_{4 \times 1}^{12}, \tag{9.14}$$

with

$$\Theta^{12} = \left(\begin{array}{cccc} \varphi_1^{bp} & \eta_1^{bp} & \varphi_{12}^{bp} & \eta_{12}^{bp} \end{array} \right) \text{ and } \kappa^{12} = \left(\begin{array}{c} \kappa_0^{12} \\ \kappa_1^{12} \\ \kappa_2^{12} \\ \kappa_3^{12} \end{array} \right). \tag{9.15}$$

145

The fit can be performed by a general linear least squares algorithm. This linear system of equations can be solved by applying different algorithms such as the Cholesky decomposition, the use of normal equations, or the singular value decomposition, among others.

The proper selection of the solving method usually depends on the topology of the design matrix Θ. This way, the set of coupling coefficients κ^1 and κ^{12} of the TM angular noise into the longitudinal TM displacement readout can be obtained.

9.2.2 *Test mass angular noise subtraction*

The band-pass filtered data Ψ^{bp} and φ^{bp}, η^{bp} are utilized to obtain the coupling coefficients κ. For example, typical fitted values for κ^1 are

$$\kappa^1 \; [m/rad] = \begin{pmatrix} -4.38 \times 10^{-6} \\ -2.19 \times 10^{-5} \end{pmatrix}. \tag{9.16}$$

Once they have been estimated, it is possible to subtract the TM angular noise from the original (unfiltered) measured longitudinal TM data as follows:

$$\Psi^1_{new} \;\; = \;\; \Psi_1 - \begin{pmatrix} \varphi_1 & \eta_1 \end{pmatrix} \cdot \kappa^1, \text{ and} \tag{9.17}$$

$$\Psi^{12}_{new} \;\; = \;\; \Psi_{12} - \begin{pmatrix} \varphi_{12} & \eta_{12} \end{pmatrix} \cdot \kappa^{12}. \tag{9.18}$$

The entire procedure to subtract the TM angular noise from the longitudinal interferometric signal is outlined by Figure 111.

Figure 112 presents the results obtained from this noise subtraction.

The solid red curve is the sensitivity reached by the longitudinal phase readout Ψ when introducing TM angular noise, which exceeds the required noise budget of $6.3 \, pm/\sqrt{Hz}$. The dashed green curve for Ψ_{new} is the sensitivity achieved after subtracting the fitted angular noise to the data of the solid curve. The blue dashed curve with crosses is the sensitivity obtained from an independent measurement where no angular noise was injected to the test masses (PZT actuated
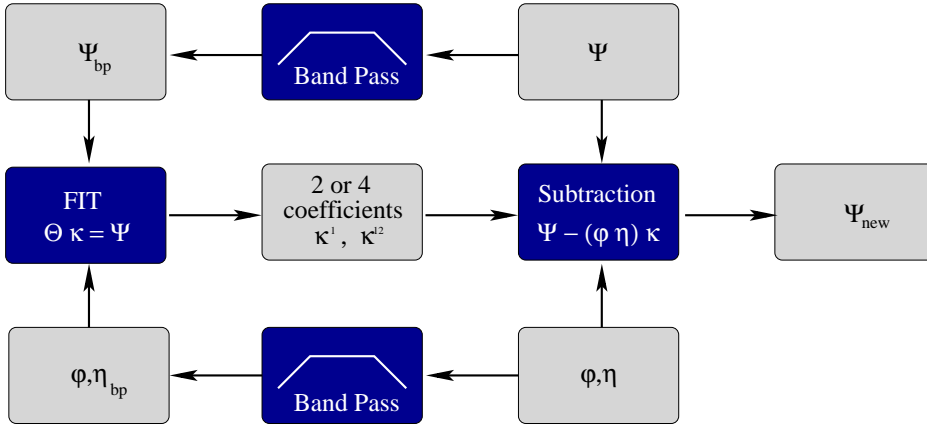
Figure 111: Flow diagram of the procedure to subtract the TM angular noise from the longitudinal phase data stream.

mirrors).

In general, noise subtraction procedures have to be performed very carefully, since there is a non-vanishing probability to corrupt the data.

In this case, the longitudinal and angular degrees of freedom are sufficiently orthogonal, such that the cross-coupling between them can be very well quantitatively characterized. The linear transformation between these two reference systems has been experimentally measured and can be expressed, for example for TM 1, as

$$
\begin{pmatrix} \Psi \ [\mathrm{m}] \\ \varphi \ [\mathrm{rad}] \\ \eta \ [\mathrm{rad}] \end{pmatrix}^{\mathrm{OB}} = \Lambda \cdot \begin{pmatrix} \Psi \ [\mathrm{m}] \\ \varphi \ [\mathrm{rad}] \\ \eta \ [\mathrm{rad}] \end{pmatrix}^{\mathrm{TM}} ,
\tag{9.19}
$$

147
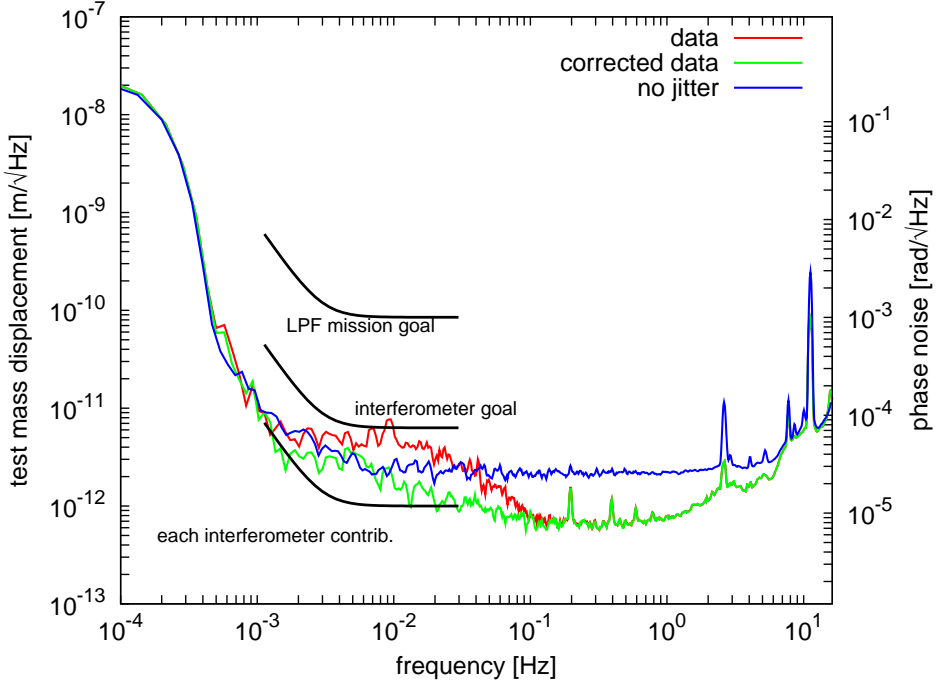
Figure 112: Red: sensitivity of the longitudinal phase readout when injecting TM angular noise. Green: sensitivity of the corrected longitudinal phase after the angular noise subtraction. Blue: independent reference measurement with no injected angular noise.

where

$$
\Lambda \;=\; \begin{pmatrix} \dfrac{\partial \Psi^{OB}}{\partial \Psi^{TM}} & \dfrac{\partial \Psi^{OB}}{\partial \varphi^{TM}} & \dfrac{\partial \Psi^{OB}}{\partial \eta^{TM}} \\[2.5ex] \dfrac{\partial \varphi^{OB}}{\partial \Psi^{TM}} & \dfrac{\partial \varphi^{OB}}{\partial \varphi^{TM}} & \dfrac{\partial \varphi^{OB}}{\partial \eta^{TM}} \\[2.5ex] \dfrac{\partial \eta^{OB}}{\partial \Psi^{TM}} & \dfrac{\partial \eta^{OB}}{\partial \varphi^{TM}} & \dfrac{\partial \eta^{OB}}{\partial \eta^{TM}} \end{pmatrix} \tag{9.20}
$$

$$
=\; \begin{pmatrix} 1 & -4.38 \times 10^{-6} & -2.19 \times 10^{-5} \\ 0.6 & 1 & 5.2 \times 10^{-4} \\ 0.4 & 7.0 \times 10^{-3} & 1 \end{pmatrix}. \tag{9.21}
$$

An example of a problematic situation where noise subtraction would be expected to corrupt the signal is if Ψ couples into φ, and φ back again into Ψ, with factors such that,

$$\frac{\partial \Psi}{\partial \varphi} \cdot \frac{\partial \varphi}{\partial \Psi} \approx 1. \tag{9.22}$$

In our case, however, this product is of the order of 10^{-6} such that no real signal Ψ is subtracted.

Typical values for the TM motion are of the order of

$$\begin{pmatrix} \Psi \\ \varphi \\ \eta \end{pmatrix}^{TM} = \begin{pmatrix} 6.3 \times 10^{-12} \, \text{m}_{\text{rms}} \\ 1 \times 10^{-7} \, \text{rad}_{\text{rms}} \\ 3 \times 10^{-7} \, \text{rad}_{\text{rms}} \end{pmatrix}. \tag{9.23}$$

As it can be seen in Figure 112, the corrected data reaches the same level of the reference measurement where no angular noise was applied, which indicates that the complete cross-coupling effect from the TM angular noise into the longitudinal measurement was fitted and extracted without corrupting the data.

Hence, the residual TM jitter due to the limited DFACS gain is not a limiting factor to the sensitivity of the interferometric longitudinal TM position measurement in LTP, if suitable angular data are available and used in post-processing.

These results are of relevance for LISA as well, since a similar cross-coupling effect can also be expected. Further characterization of noise sources and noise subtraction techniques are presented in Section 9.4.

9.3 ELECTRODE-HOUSING APERTURE

The position and attitude of the LTP test masses is measured in all six degrees of freedom by capacitive sensors, located at the inner walls of an electrode housing (EH), where the test mass resides (see Figure 113).

In order to obtain a higher sensitivity in the main TM longitudinal and angular degrees of freedom, the LTP OB interferometer is employed to measure the position and attitude of the test masses, which requires an appropriate aperture in

149

Chapter 9
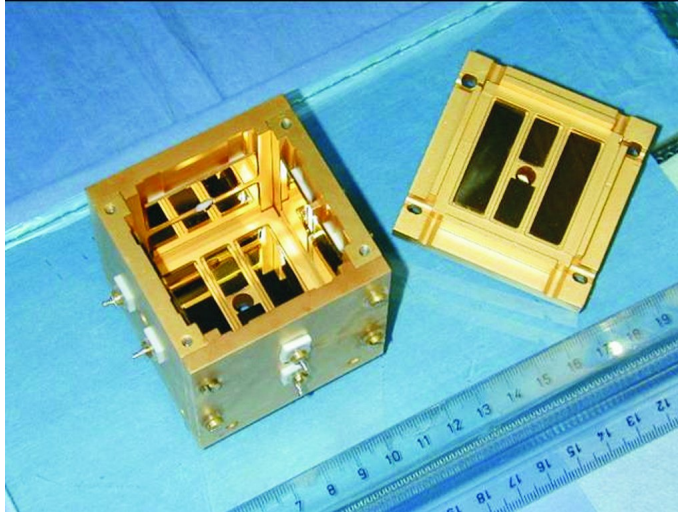
Figure 113: Photograph of the LTP electrode housing prototype.

the EH for the laser beam to reach the test mass. Depending on the dimensions of this aperture, the laser beam parameters and the fact that the LTP interferometer is operated with Gaussian beams, beam clipping effects at the EH aperture are expected, and need to be assessed. This point is illustrated by Figure 114, which is obtained by inserting into the LTP optical model, a corresponding aperture with dimensions, according to the current design.

It can be seen from the optical model that beam clipping at the level of three beam radii ($3\,\omega_o$) can be expected at the edges of this aperture, which can produce deformations of the beam profile (intensity and phase spatial distribution) and generate stray light, which is a common and well-known noise source in interferometers, often responsible for performance limitations.

In LTP, stray light that originates and remains within the optical bench itself, will mostly contribute to the phase measurement as a constant offset, due to the high mechanical and thermal stability of bench itself and its optical components. However, this is not the case for stray light originating at the EH aperture, especially under the influence of residual TM angular noise, as presented in Section 9.2.
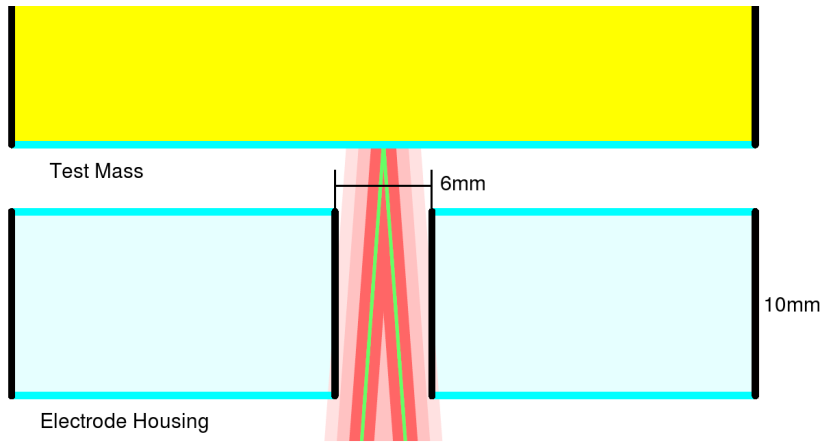
Figure 114: Illustration of beam clipping in the LTP optical model. The red shades indicate one, two, and three times the Gaussian beam radius.

Therefore, experimental investigations on this topic were conducted at the EM optical bench. The PZT-actuated mirrors presented above were used to simulate in hardware the residual TM angular noise, and a reflective golden plate with several apertures of different dimension was manufactured to simulate beam clipping effects of the EH.

9.3.1 *Experimental Setup*

In order to simulate the EH aperture in the laboratory interferometer setup, a brass plate with four different apertures was manufactured in-house. This plate was polished and coated with a reflecting gold layer to obtain similar optical properties as the expected from the EH. The laser beam width was measured at the positions of TM 1 and TM 2 with a beam analyzer, in order to design the aperture dimensions for the corresponding beam clipping levels in terms of the beam radius. In the LTP OB EM, the radius of the beam at the positions of TM 1 and TM 2 was measured to be

$$\omega_1 = 646\,\mu m$$
$$\omega_2 = 846\,\mu m.$$

The dimensions of the four apertures were designed such that the smallest one would produce beam clipping at $2\,\omega_o$ at TM 1 and $1.6\,\omega_o$ at TM 2, and the largest one at $5.2\,\omega_o$ and $4\,\omega_o$, respectively. Figure 115 shows a photograph of the golden plate, pointing out the size of the apertures in term of the beam radius at the top and bottom of the picture, for TM 1 and TM 2, respectively.

Figure 115: Golden plate with four different apertures. The numbers in top and bottom correspond to the aperture size in beam radii for TM 1 and TM 2, respectively.

In order to mount the golden plate in front of the PZT-actuated mirrors at the optical bench, an aluminum *balcony* (see Figure 116) was designed to be fixed at the Zerodur® walls, where the PZT-mirrors are mechanically attached.

9.3.2 *Interferometer sensitivity measurements*

In order to avoid excess coupling from test mass jitter, the pivot point on the test mass was calibrated with the interferometer signals by the linear electronic matrix in the PZT driver circuitry. This corresponds to a rotation of the test
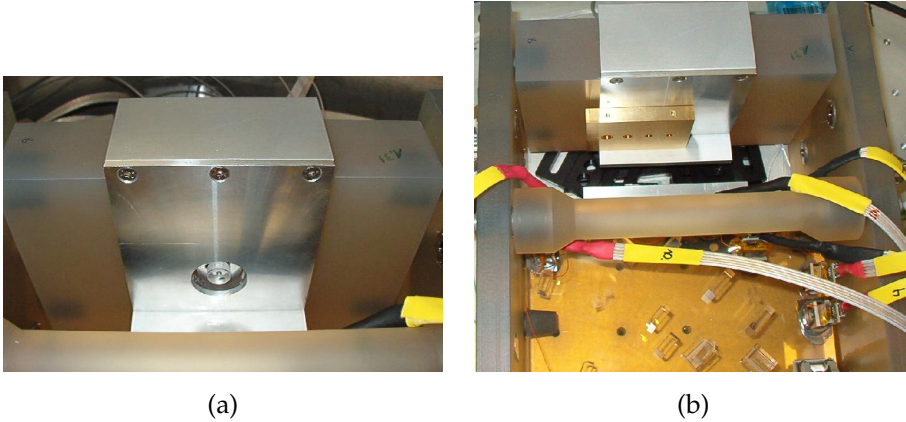
Figure 116: (a) Balcony in front of TM 2 with inserted PZT-mirror. (b) Photograph of the golden plate mounted on the balcony.

masses around the laser beam reflection point, but not around their center of mass.

The measurements presented here were focused on the smallest aperture in front of both test masses. Due to the long lever arm of the beam being reflected on TM 1, beam clipping effects were expected to be more severe at the area of TM 2 and readout of TM 1-TM 2 interferometer. Angular noise was injected into both PZT-mirrors (TM 1 and TM 2), and similarly to the measurements of Section 9.2, the DWS measurements readout in each case were used to apply the angular noise subtraction technique presented above.

Figure 117 presents the sensitivity of the interferometers, by placing the smallest aperture in front of TM 1, which corresponds to a beam clipping level of the order of $2\,\omega_0$ at this point.

Figure 118 presents the sensitivity if the interferometers, by placing the smallest aperture in front of TM 2, corresponding to a beam clipping of $1.6\,\omega_0$.

153

Chapter 9

LSD of the longitudinal measurement at the TM 1 interferometer
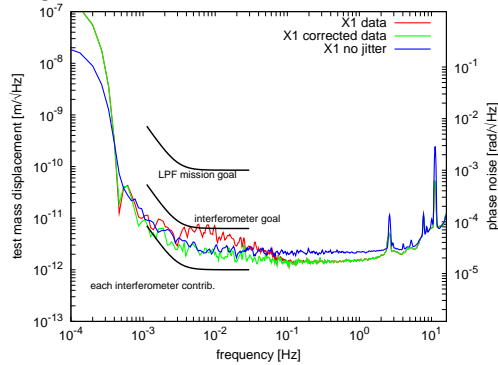
LSD of the longitudinal measurement at the TM 1-TM 2 interferometer
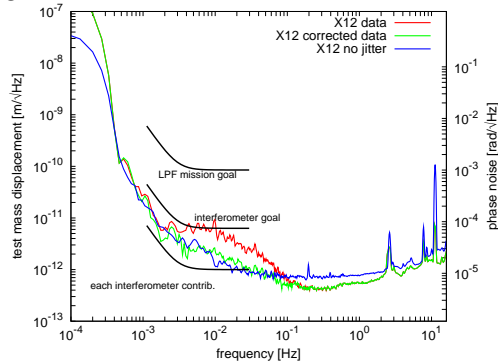
Figure 117: Smallest aperture inserted in front of TM 1. Angular noise subtraction successfully applied to both interferometers.

The results obtained from these measurements show an increase in the noise level of the interferometric TM displacement readout, mainly due to the injected angular noise. An additional significant contribution due to beam clipping effects could not finally be observed. However, by applying the angular noise subtraction technique, it was possible in all cases to eliminate the excess noise contribution that would prevent the interferometric test mass readout from achieving its required sensitivity.

LSD of the longitudinal measurement at the TM 1 interferometer
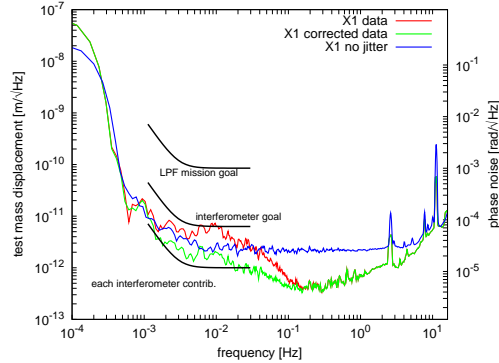
LSD of the longitudinal measurement at the TM 1-TM 2 interferometer
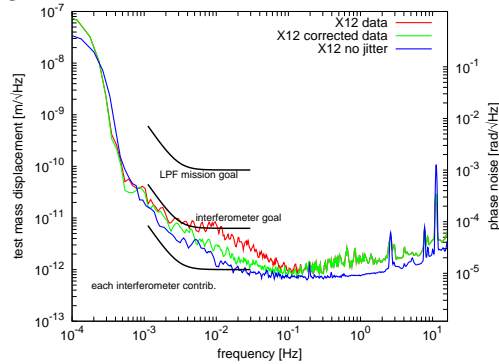
Figure 118: Smallest aperture inserted in front of TM 2. Angular noise subtraction successfully applied to both interferometers.

9.4 NOISE SUBTRACTION TECHNIQUES

A series of investigations has been conducted to identify and model the limiting noise sources in the optical test mass readout sensitivity of the LTP interferometer [43, 44], which are laser frequency fluctuations and residual non-linear noise of the optical pathlength difference (OPD).

The baseline strategy to suppress these noise sources is to actively stabilize the laser frequency and the OPD, in order to minimize their effect in the main phase readout of the TM 1 and TM 1-TM 2 interferometers, as described in Chap-

ter 8.

This section presents a noise subtraction technique based on the linear fitting of the coupling coefficients of the measured information on these noise sources obtained from the interferometer – Ψ_F and Ψ_R – onto the main phase measurements – Ψ_1 and Ψ_{12} –. This technique enables the purification of these latter phase data starting from time-series measured under free-running noise conditions (no operative stabilizations).

Furthermore, in case of malfunction or non-optimal noise suppression of the respective control loop, this technique can be also applied to remove the remaining excess noise from the main signals.

Considering that all necessary data will be available during mission operations at the LTP DMU output and transfered to the LPF onboard computer (OBC), the noise subtraction procedure could also be included in the onboard data processing, as a fall-back strategy to purify the interferometric signals used for DFACS TM control, in the presence of excess noise or failure of the interferometer stabilizations.

The analyses presented here were computed with LTPDA [54, 55], which is the dedicated software toolbox developed for the data analysis of the LISA Pathfinder mission.

The noise subtraction algorithm is based on a time-domain linear fit that sequentially estimates the coupling coefficients of each noise contribution, within the frequency bandwidth where they become a limiting factor to the interferometer sensitivity. The time evolution of the data directly measured from the interferometer is dominated by slow drifts at very low frequencies ($\lesssim 1\,\mathrm{mHz}$), mainly driven by temperature variations, and fast electronic and mechanic fluctuations at higher frequencies ($\gtrsim 1\,\mathrm{Hz}$).

In order to distinguish the behavior of the data in the frequency range of interest ($3 - 30\,\mathrm{mHz}$ for LPF), the time series are band-pass filtered in software for a better estimation of the noise coupling coefficients. The band-pass filter used for the data analysis has been designed as a second order IIR filter in the frequency range of $0.4 - 500\,\mathrm{mHz}$.

For this investigation, the following noise sources have been taken into account:

- laser frequency fluctuations, and

- OPD fluctuations that can be separated in two contributions:
    - a Doppler shift induced by fast OPD changes, and
    - dominant at lower frequencies appears non-linear excess OPD noise caused by the beat of spurious sidebands in the optical signals, originated at the AOM drivers [43, 44, 60].

In order to describe this noise subtraction technique, the correction of the free-running measurement (stabilizations off) of the interferometer TM 1-TM 2 (X_{12}) obtained with the engineering models of the LA and OB (Figure 92), is presented step by step as an example.

9.4.1 *Correction of Doppler shift*

As explained in Section 7.2.1, the phase measurement is based on a single-bin discrete Fourier Transform (SBFT) which relies on the heterodyne signal to remain centered in the bin chosen. High frequency phase shifts such as the effects introduce by fast OPD fluctuations produce apparent fluctuations of the heterodyne frequency f_{het} within the bin that resembles a Doppler shift[6].

The contribution of this effect on the measured raw phase φ can be computed as:

$$\Delta\varphi_i^{Doppler} = -\frac{1}{2\,bin}\,\gamma(n)\,\sin(2\varphi_i) + \frac{1}{4\,bin^2}\,\gamma^2(n)\,\sin(2\varphi_i) + \frac{1}{8\,bin^2}\,\gamma^2(n)\,\sin(4\varphi_i),$$

$$(9.24)$$

where

$$\gamma(n) = \frac{\varphi_{n+1} - \varphi_{n-1}}{4\pi} \qquad (9.25)$$

is a scaled numerical estimate of the frequency shift at the n-th point of the time series φ_i, and $\varphi_i^{Doppler}$ is the Doppler contribution to the raw phase φ_i measured at the interferometer $i = \{1, 12, F, R\}$, and bin is the frequency component of the Fourier Transform corresponding to the heterodyne frequency [61].

---

6 Although not necessarily a real velocity is involved, the term "Doppler shift" has become customary in the AEI LPF group to describe this error coming from a frequency deviation.

157

Chapter 9

After computation of the Doppler contribution, this can be subtracted from the original raw phase as

$$\varphi_i^{noDoppler} = \varphi_i - \Delta\varphi_i^{Doppler} \tag{9.26}$$

Similarly, the Doppler shift can be subtracted from the difference phases $\Psi_i = \varphi_i - \varphi_R$ as

$$\Psi_i^{noDoppler} = \varphi_i^{noDoppler} - \varphi_R^{noDoppler} \tag{9.27}$$

As an example, Figure 119 shows the LSDs of the original difference phase Ψ_{12}, the Doppler-corrected phase $\Psi_{12}^{noDoppler}$, and the corresponding Doppler contribution $\Psi_{12}^{Doppler}$. It can be seen that the Doppler shift has a significant
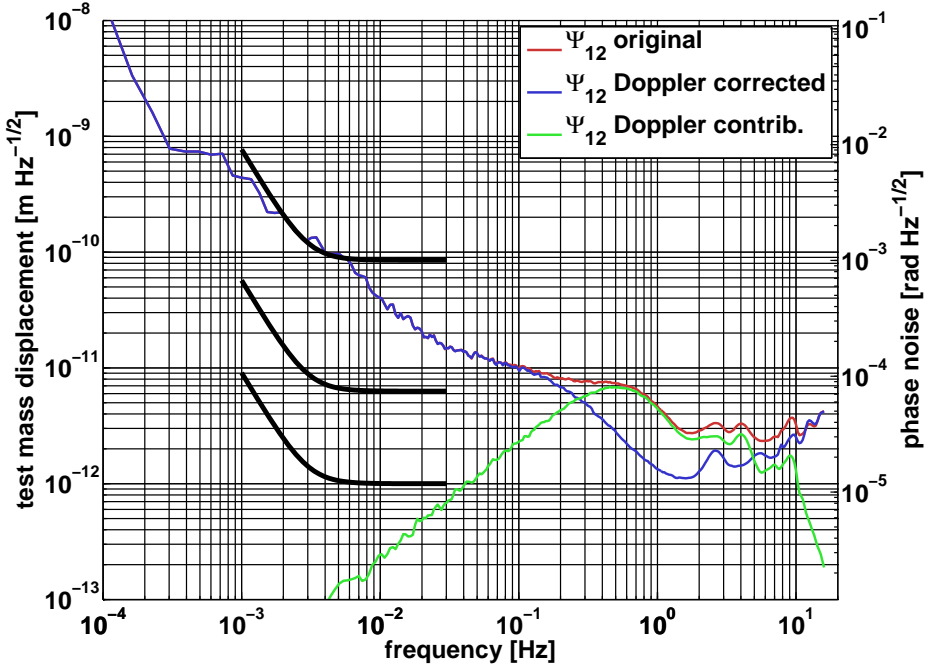
Figure 119: Red: linear spectral densities of the originally measured free-running Ψ_{12}. Blue: obtained Doppled-corrected phase $\Psi_{12}^{noDoppler}$. Green: corresponding Doppler contribution $\Psi_{12}^{Doppler}$.

effect on the measurement, and limits the sensitivity of the interferometer at

frequencies above 300 mHz.

For subsequent noise coupling estimations and subtraction, Doppler-corrected phases $\Psi_i^{noDoppler}$ are used as starting point of the algorithm.

9.4.2 *Correction of non-linear OPD noise*

During investigations on the noise sources of the LTP interferometer [43, 44], it was found that electromagnetic cross-talk between the AOM drivers produce spurious sidebands on the optical signals that interfere at the photodetector, generating beats of unstable phase at the heterodyne frequency f_{het}. This effect results in a non-linearity in the phase readout that, according to the mentioned investigations, can be analytically described as

$$\Psi_i^{OPD} = \left(k_{ia} \sin\left(\frac{\varphi_i + \varphi_R}{2} \right) + k_{ib} \cos\left(\frac{\varphi_i + \varphi_R}{2} \right) \right) \sin\left(\frac{\varphi_i - \varphi_R}{2} \right)$$

$$+ \left(k_{ic} \sin\left(\varphi_i + \varphi_R \right) + k_{id} \cos\left(\varphi_i + \varphi_R \right) \right) \sin\left(\varphi_i - \varphi_R \right), \quad (9.28)$$

where $\varphi_i - \varphi_R$ represents the slowly varying test mass motion, and $\frac{\varphi_i + \varphi_R}{2}$ describes the much larger common-mode phase fluctuations caused by OPD variations. This expression can be rephrased as

$$\Delta \Psi_i^{OPD} = \mathbf{k}_i \cdot \mathbf{OPD}(\varphi_i, \varphi_R), \quad (9.29)$$

where

$$\mathbf{k}_i = \left(\begin{array}{cccc} k_{ia} & k_{ib} & k_{ic} & k_{id} \end{array} \right) \quad (9.30)$$

is the vector of coupling coefficients, and the vector

$$\mathbf{OPD}(\varphi_i, \varphi_R) = \left(\begin{array}{c} \sin\left(\frac{\varphi_i + \varphi_R}{2} \right) \sin\left(\frac{\varphi_i - \varphi_R}{2} \right) \\ \cos\left(\frac{\varphi_i + \varphi_R}{2} \right) \sin\left(\frac{\varphi_i - \varphi_R}{2} \right) \\ \sin\left(\varphi_i + \varphi_R \right) \sin\left(\varphi_i - \varphi_R \right) \\ \cos\left(\varphi_i + \varphi_R \right) \sin\left(\varphi_i - \varphi_R \right) \end{array} \right) \quad (9.31)$$

contains the non-linear OPD terms. Upon computation of the non-linear terms $\mathbf{OPD}(\varphi_i, \varphi_R)$ from the analytic model, a linear fit algorithm can be applied to estimate the coupling coefficients $\mathbf{k}_i$ onto the measurand Ψ_i. It is important to remark that the measured data φ_i and φ_R should be Doppler-corrected prior to the computation of the terms $\mathbf{OPD}(\varphi_i, \varphi_R)$, as explained in Section 9.4.1.

159

Chapter 9

As mentioned above, the measured time series are dominated at higher frequencies by fast electronic and mechanic noise and slow drifts at lower frequencies, mainly driven by temperature fluctuations. Therefore, a band-pass filter between $0.4 - 500$ mHz is applied to the measured time series and to the computed terms $\mathbf{OPD}(\varphi_i, \varphi_R)$, in order to eliminate these additional noise contributions. The band-pass filtered data Ψ_i^{bp} and $\mathbf{OPD}^{bp}(\varphi_i, \varphi_R)$ is used to estimate the coupling coefficients $\mathbf{k}_i$ by a linear least squares algorithm. However, the noise subtraction applies the estimated coefficients to the original unfiltered data

$$\Psi_{i_{opdns}} = \Psi_i - \Psi_i^{OPD} = \Psi_i - \mathbf{k}_i \cdot \mathbf{OPD}(\varphi_i, \varphi_R) \tag{9.32}$$

Figure 120 illustrates with a diagram the noise subtraction algorithm.
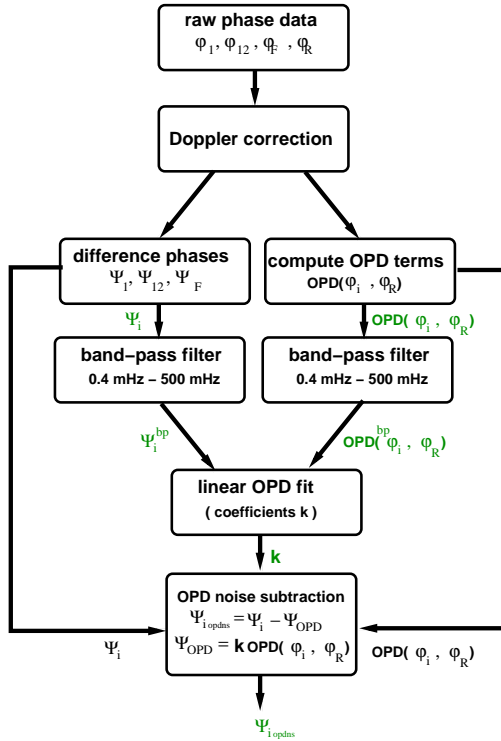
Figure 120: Flow diagram of the OPD noise subtraction algorithm.

This technique was used to correct non-linear OPD noise in real interferometric

data, and as the example applied for Ψ_{12}, Figure 121 shows the obtained LSDs for the Doppler-corrected phase $\Psi_{12}^{noDoppler}$, the phase $\Psi_{i_{opdns}}$ obtained from the OPD noise subtraction, and the corresponding non-linear OPD noise contribution Ψ_{12}^{OPD}.
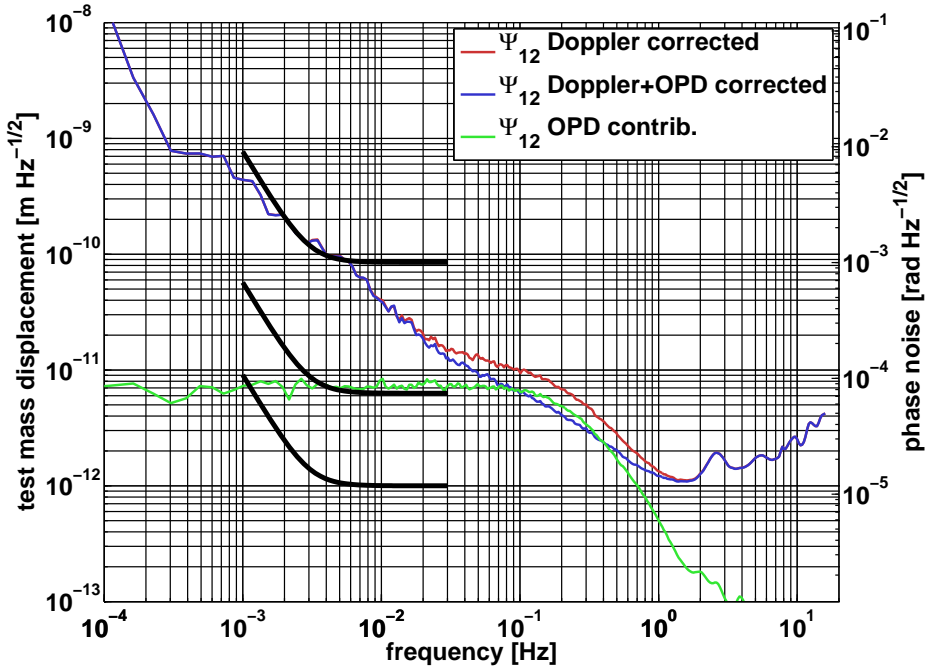
Figure 121: Red: linear spectral densities of the Doppled-corrected phase $\Psi_{12}^{noDoppler}$. Blue: the phase $\Psi_{i_{opdns}}$ obtained from the OPD noise subtraction. Green: corresponding non-linear OPD noise contribution Ψ_{12}^{OPD}.

The blue trace, which is the OPD-corrected LSD, evidences the characteristic $1/f$ shape of laser frequency noise that will be corrected in the next step. Assuming that laser frequency noise was not the dominant factor in this plot, the non-linear OPD contribution (green trace) would limit the interferometer sensitivity at the level of $7\,\mathrm{pm}/\sqrt{\mathrm{Hz}}$ below $100\,\mathrm{mHz}$, in terms of test mass displacement.

161

The coefficients obtained from the linear fit are

$$\mathbf{k}_{12}[\text{rad}] = \left(\ 7.59 \times 10^{-5} \quad -1.93 \times 10^{-5} \quad -1.88 \times 10^{-5} \quad -1.63 \times 10^{-5}\ \right)$$

with their corresponding errors

$$\delta\mathbf{k}_{12}[\text{rad}] = \left(\ 3.88 \times 10^{-7} \quad 3.87 \times 10^{-7} \quad 2.61 \times 10^{-7} \quad 2.61 \times 10^{-7}\ \right).$$

The maximum error obtained is of the order of 2% and is a good indicator of the convergence and precision of the coefficient estimations.

For the subsequent laser frequency noise subtraction, the corrected phases $\Psi_{i_{\text{opdns}}}$ are used as input for the algorithm.

9.4.3 Correction of laser frequency noise

As described in sections 6.3.2 and 8.2.3, laser frequency fluctuations $\delta\nu$ proportionally translate to phase noise $\delta\varphi$ in interferometers by its armlength mismatch ΔL as

$$\delta\varphi = 2\pi\frac{\Delta L}{c}\delta\nu. \tag{9.33}$$

In the case of the frequency interferometer on the LTP optical bench, the armlength mismatch is by design approximately 38 cm. Hence, the difference phase Ψ_F obtained from this interferometer gives an indirect measurement of laser frequency fluctuations, where they are the dominant effect.

The measured time series Ψ_F can be used to estimate the coupling factors of laser frequency fluctuations on the main measurements Ψ_1 and Ψ_{12}.

The linear fit algorithm uses as input the band-pass filtered OPD-corrected time series $\Psi_{i_{\text{opdns}}}^{\text{bp}}$ ($i = \{1, 12\}$) and $\Psi_{F_{\text{opdns}}}^{\text{bp}}$ that were previously obtained from the OPD noise subtraction (Section 9.4.2), in order to obtain the coupling coefficients $\mathbf{c}_i$. Similarly to the case of the OPD noise, although the coefficients have been obtained with band-pass filtered data, the laser frequency noise subtraction is applied to unfiltered data that has been previously OPD corrected

$$\Psi_{i_{\text{freqns}}} = \Psi_{i_{\text{opdns}}} - \mathbf{c}_i\Psi_{F_{\text{opdns}}} \tag{9.34}$$

Figure 122 shows the flow diagram of the laser frequency noise subtraction algorithm.
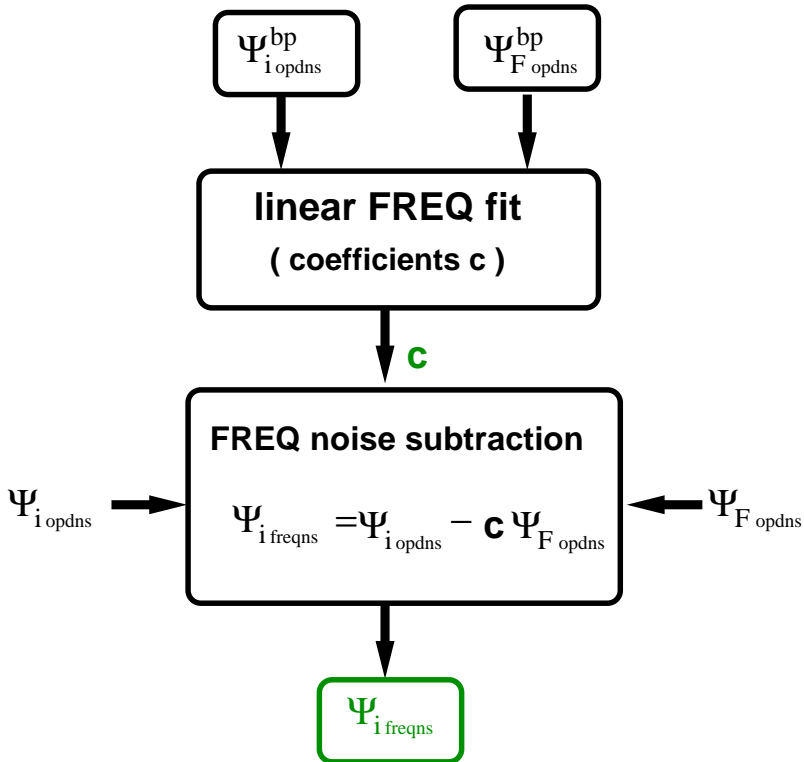
Figure 122: Flow diagram of the laser frequency noise subtraction algorithm.

The LSD of the results obtained by applying this technique are shown in Figure 123.

The blue trace is the LSD of data obtained after the noise complete noise subtraction algorithm, which can be corrected from the level of $400\,\mathrm{pm}/\sqrt{\mathrm{Hz}}$ to $20\,\mathrm{pm}/\sqrt{\mathrm{Hz}}$ at $1\,\mathrm{mHz}$ and thus meet the required sensitivity even without frequency stabilization.

163
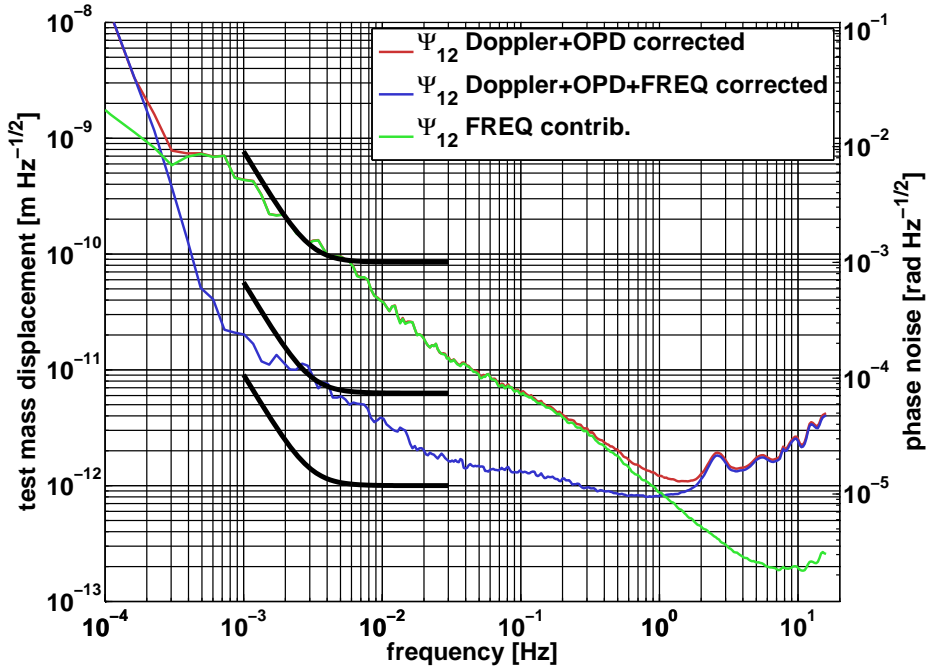
Figure 123: Red: linear spectral densities of the OPD-corrected phase $\Psi_{12_{\text{opdns}}}$. Blue: the phase $\Psi_{12_{\text{freqns}}}$ obtained from the laser frequency noise subtraction. Green: corresponding contribution of laser frequency noise Ψ_{12}^{FREQ}.

In this case, the coupling coefficient c_{12} obtained from the fit is

$$c_{12} = 5.26 \times 10^{-2} \pm 9.96 \times 10^{-6} \text{ [rad/rad]}$$

This corresponds to an armlength difference of approximately 19 mm in accordance with the corresponding value of 14.5 mm measured in [44]. The complete noise subtraction technique and the obtained results are briefly summarized in the following section.

9.4.4 *Outline of entire algorithm*

The noise subtraction algorithm presented here is divided in three subsequent steps: Doppler correction $\Rightarrow$ correction of non-linear OPD noise $\Rightarrow$ correction of laser frequency noise. The results obtained from each step are used as input for the subsequent noise correction. Each noise source affects the interferometer sensitivity in a different frequency bandwidth that needs to be properly taken into account in order to apply a linear fit algorithm to determine the corresponding coupling coefficients.

Moreover, original interferometer data contains noise contributions from sources that dominate its time evolution and have not yet been accounted for in this algorithm, such as temperature fluctuations. Therefore, the data is band-pass filtered in the frequency range of $0.4 - 500$ mHz in order to decouple these effects from the time series, thus obtaining a data stream governed by the noise contributions described above. The band-pass filtered data are used to obtain the coupling factors of each noise source by a linear fit algorithm, however, the noise subtraction is applied on the original unfiltered data using these same coefficients.

A flow diagram describes the entire algorithm is presented in Figure 124. The sequence of the algorithm has been defined such that non-linear OPD noise is corrected first in the measured phases Ψ_1, Ψ_{12}, and also Ψ_F before entering the laser frequency noise subtraction step. However, this is numerically not optimal as the contribution of laser frequency noise is much higher than the OPD noise, which means that the fit has to estimate a relatively small coupling factor out of noisy data overcasting the non-linear OPD contribution. Even under these circumstances, the algorithm seems to perform sufficiently well, but this effect can be further investigated in order to optimize the technique.

165

Chapter 9
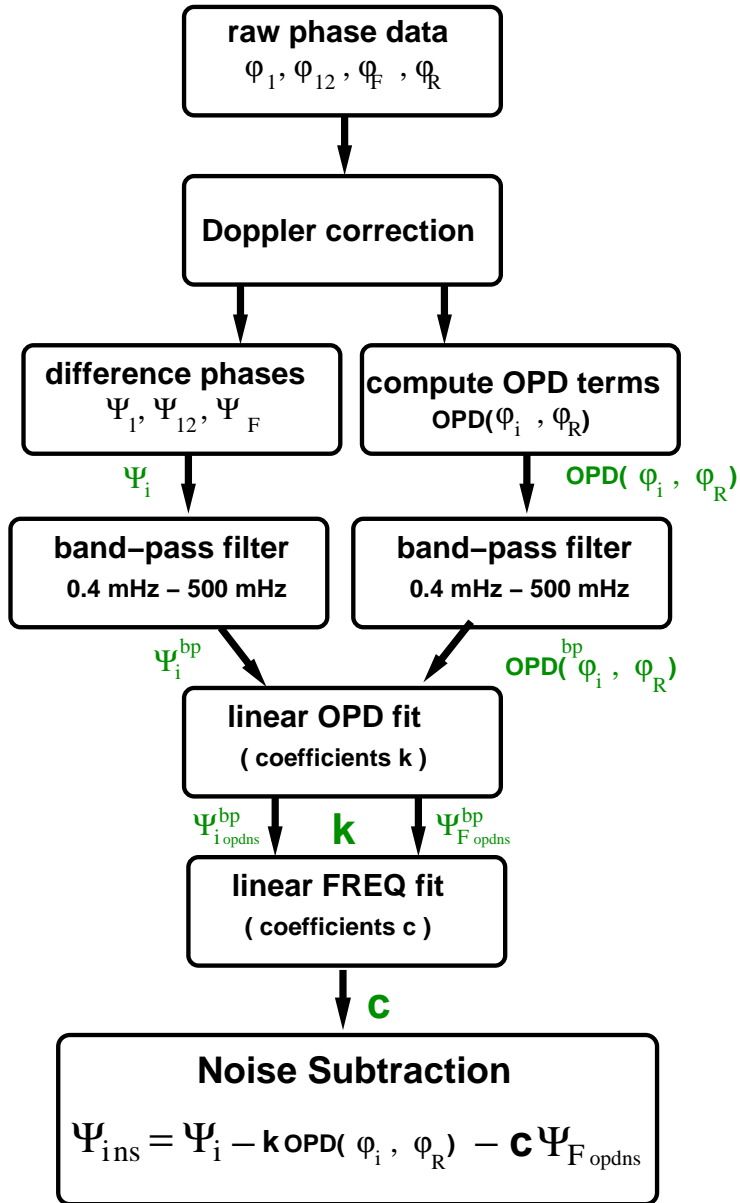
Figure 124: Flow diagram of the entire noise subtraction algorithm.

The results obtained for the example presented here are summarized in the plot of Figure 125, which shows the LSDs of the original data Ψ_{12}, the corrected data obtained at the output of the complete noise subtraction Ψ_{12ns}, and each noise contribution: Doppler shift, non-linear OPD noise, and laser frequency fluctuations.
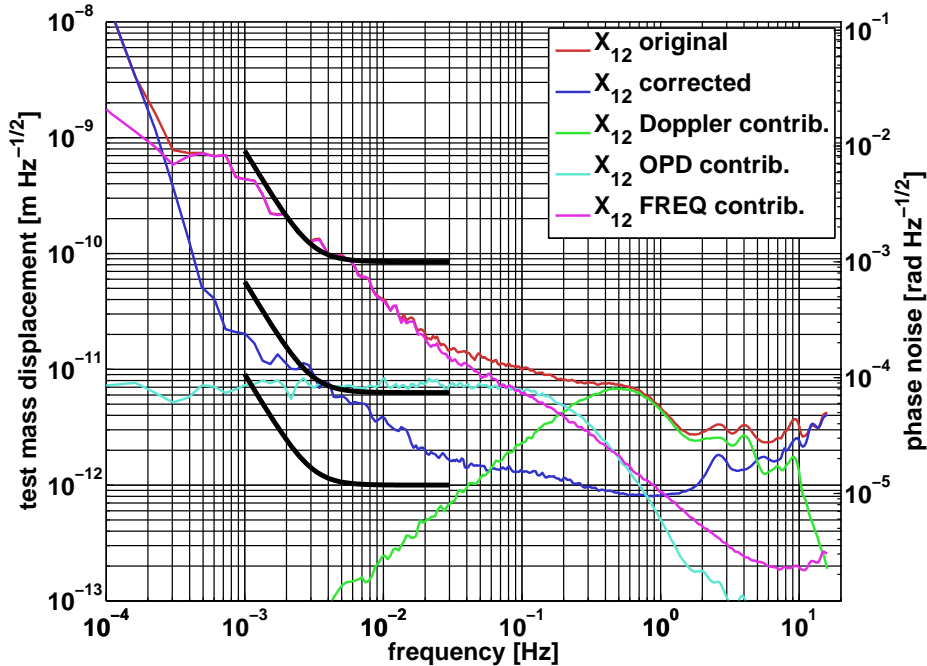
Figure 125: Red: linear spectral density of the original measured phase Ψ_{12}. Blue: LSD of the corrected phase Ψ_{12ns} obtained from the noise subtraction algorithm. Green: noise contribution of the Doppler shift $\Psi_{12}^{Doppler}$. Cyan: contribution of non-linear OPD noise Ψ_{12}^{OPD}. Magenta: noise contribution of laser frequency fluctuations Ψ_{12}^{FREQ}.

Besides the case of noise subtraction on free-running measured data as presented above, the method has been applied on partially and fully stabilized measurements, where excess noise remaining unsuppressed by control loop was fitted and subtracted from the data.

Stabilized laser frequency and free-running OPD

Figure 126 shows LSDs obtained from the noise subtraction algorithm applied to the measured difference phase Ψ_1 under conditions of operative laser frequency stabilization and free-running OPD.
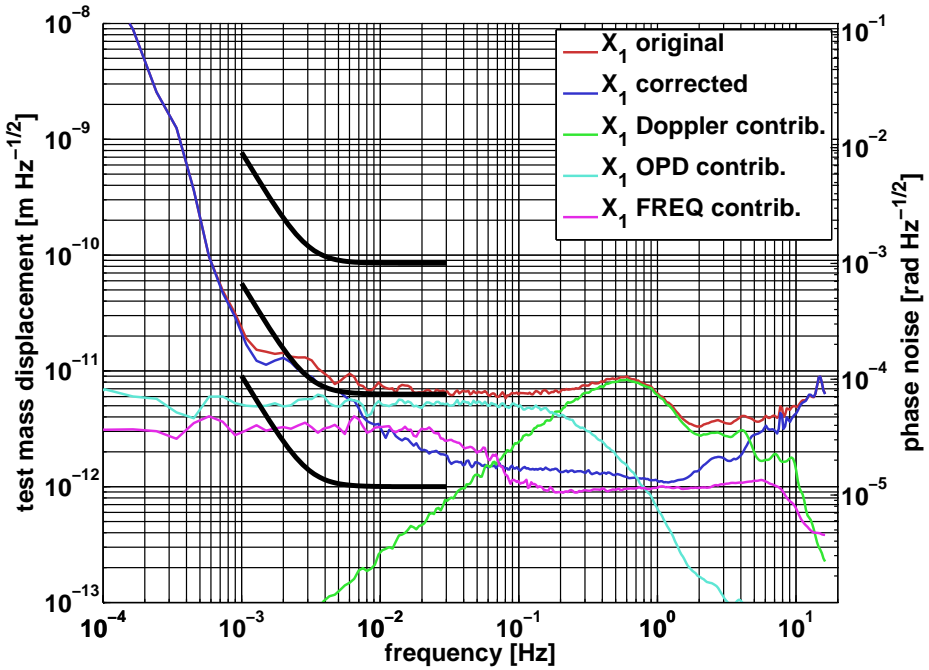
Figure 126: Measurement with stabilized laser frequency and free-running OPD. Red: linear spectral density of the original measured phase Ψ_1. Blue: LSD of the corrected phase Ψ_{1ns} obtained from the noise subtraction algorithm. Green: noise contribution of the Doppler shift $\Psi_1^{Doppler}$. Cyan: contribution of non-linear OPD noise Ψ_1^{OPD}. Magenta: noise contribution of laser frequency fluctuations Ψ_1^{FREQ}.

It can be seen that the contribution of non-linear OPD noise (cyan trace) in the original data clearly limits the interferometer sensitivity at approximately

$5 \, \text{pm}/\sqrt{\text{Hz}}$. The following coupling coefficients with their corresponding errors were determined for this noise source by the method presented above

$$
\begin{pmatrix}
\mathbf{k_1} \, [\text{rad}] & \delta\mathbf{k_1} \, [\text{rad}] \\
5.00 \times 10^{-5} & 1.53 \times 10^{-7} \\
-4.09 \times 10^{-5} & 1.53 \times 10^{-7} \\
-7.38 \times 10^{-5} & 9.50 \times 10^{-8} \\
-2.88 \times 10^{-5} & 9.53 \times 10^{-8}
\end{pmatrix}
$$

Furthermore, the magenta trace is the contribution of remaining laser frequency noise that was not suppressed by the control loop, and limits the interferometer sensitivity at a level of $3 \, \text{pm}/\sqrt{\text{Hz}}$ between 10 mHz and 30 mHz. The coupling coefficient estimated for this case is

$$\mathbf{c_1} = 3.03 \times 10^{-2} \pm 1.73 \times 10^{-4} \, [\text{rad/rad}].$$

A significant improvement from the Doppler correction (green trace) can also be observed at frequencies above 200 mHz.

Stabilized system: excess laser frequency noise

Figure 127 shows LSDs obtained for the case where the measurement was conducted in fully stabilized condition, with active OPD and laser frequency control loops. The plot shows that the Doppler shift is the dominant noise above 1 Hz, and below this point up to 40 mHz excess noise introduced by the laser frequency control loop is the limiting factor. The coefficient obtained from the fit for this case is

$$\mathbf{c_{12}} = 4.69 \times 10^{-2} \pm 4.44 \times 10^{-4} \, [\text{rad/rad}].$$

From the traces (green and magenta, respectively) of the noise contributions computed for the Doppler shift and the noise introduced by the laser frequency control loop, it can be seen that the effect of non-linear OPD noise was negligible in this measurement, which is consistent with the corresponding contribution

169

Chapter 9
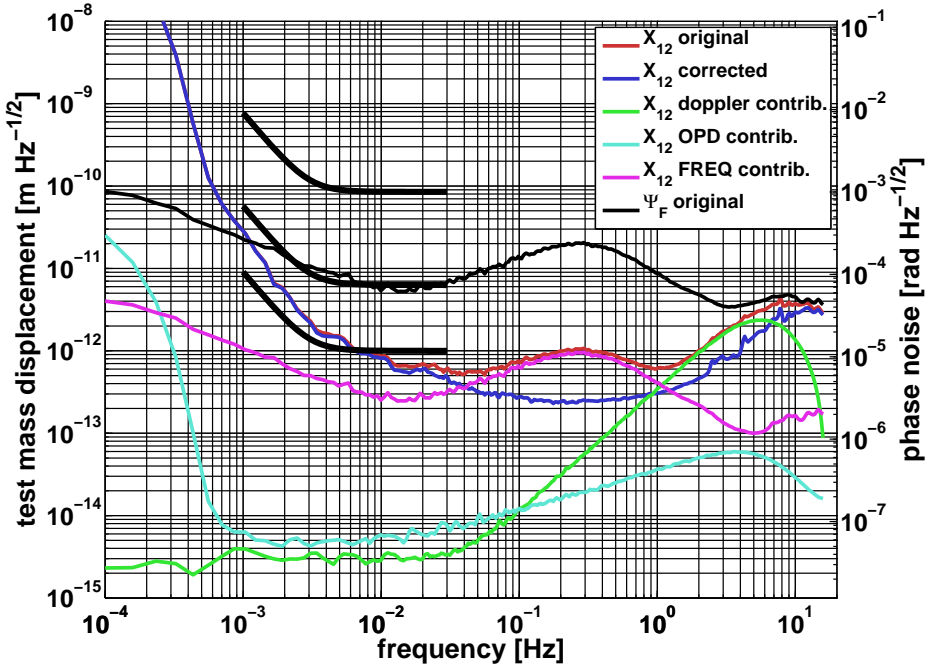
Figure 127: Red: linear spectral density of the original measured phase Ψ_{12} expressed as TM displacement noise X_{12}. Blue: LSD of the corrected phase Ψ_{12ns} obtained from the noise subtraction algorithm. Green: noise contribution of the Doppler shift $\Psi_{12}^{Doppler}$. Cyan: contribution of non-linear OPD noise Ψ_{12}^{OPD}. Magenta: noise contribution of laser frequency fluctuations Ψ_{12}^{FREQ}. Black: linear spectral density of the original measured phase Ψ_F

computed by the noise subtraction algorithm (cyan trace). The coefficients obtained from the fit in this case are

$$
\begin{pmatrix}
\mathbf{k}_{12}[\text{rad}] & \delta\mathbf{k}_{12}[\text{rad}] \\
-4.91 \times 10^{-5} & 4.71 \times 10^{-7} \\
3.33 \times 10^{-5} & 4.42 \times 10^{-7} \\
\mathbf{-6.19 \times 10^{-7}} & \mathbf{2.05 \times 10^{-7}} \\
3.98 \times 10^{-5} & 4.05 \times 10^{-7}
\end{pmatrix}
$$

The error of the coefficient for the third OPD term ($\sin(\varphi_{12} + \varphi_R) \sin(\varphi_{12} - \varphi_R)$) is approximately 33% and very large compared to the other terms, which is also an indicator that the non-linear OPD noise present in this measurement was so small that it vanished in the noise floor of the measurement, where other effects become significant, such as, for instance, thermal expansion of the Zerodur® baseplate.

According to the results obtained from applying this noise subtraction algorithm to different cases, where the measurement conditions vary from free-running to fully stabilized, and especially by taking into account the errors of the coefficients computed by the fit routine, this method has proven to be a powerful technique to characterize the coupling of diverse noise sources in the instrument and correct for their contribution, even in the presence of active stabilizations and remaining unsuppressed excess noise.

Nevertheless, it is always necessary to be prudent in the use of noise subtraction techniques and critically evaluate the obtained result, as it could also corrupt the data. This has been evidenced in the latter case, even though the contribution of this third OPD coefficient was negligible to the total noise floor of the measurement after the noise subtraction. It is always preferable to remove a noise source at its origin instead of applying analysis techniques to subtract it in post-processing. The LTP interferometry has been designed accordingly.

This noise subtraction technique and the angular noise subtraction algorithm of Section 9.2 have been presented separately for explanatory purposes. However, they can be regarded as a single method that accounts: test mass angular noise, Doppler shift, non-linear OPD noise, and laser frequency fluctuations. A sample MATLAB® script that makes use of the LTPDA toolbox for this kind of integrated analysis is given in Appendix A. A similar analysis has been also implemented

171

Chapter 9

with the LTPDA GUI[7] that produces the same results. Screenshots of the block representations for the analysis are shown in Appendix B.

The implementation of both the script-based and the GUI-based noise subtraction algorithms evidenced the necessity of implementing dedicated processing methods in the LTPDA toolbox in order to ease this kind of data analysis to the user.

---

7 This work was done together with Miquel Nofrarias.

SUMMARY AND OUTLOOK

This Part presented a detailed description of the measurement principle of the LTP interferometry and its specific implementation at the level of engineering and flight model hardware.

The required test mass displacement and angular sensitivity of $6.3\,\mathrm{pm}/\sqrt{\mathrm{Hz}}$ and $20\,\mathrm{nrad}/\sqrt{\mathrm{Hz}}$, respectively, has been demonstrated by operating the optical bench engineering model with laboratory breadboard equipment for the optical modulation and control loops, as well as with dedicated engineering models manufactured by industrial partners.

As the LISA Pathfinder missions approaches its integration phase, deliverables of the subunits need to be precisely characterized and tested in functionality and noise level.

The case of the testbed setup for the Laser Assembly engineering model presented in Section 8.4, is a representative example of the effort jointly invested by scientists and industrial partners, in order to obtain the required performance of the system. The results from interferometric test mass displacement sensitivity measurements with fully operating stabilization systems were obtained as team work within the AEI LTP group in collaboration with Kayser-Threde Munich, as industrial partner in charge of the Laser Assembly.

Furthermore, the application of a real-time wavefront detector to help in the design and characterization of quasi-monolithic fiber injectors for the LTP optical bench has been achieved in close collaboration with the University of Glasgow, which is the institution in charge of delivering the flight model optical bench.

This device has been also very useful in the characterization of optical components for LTP, such as the optical window, leading to noise predictions of the potential effects of this component on the noise level of the phase measurement. Due to its wide range of application in optical metrology, it will also be used in forthcoming LISA investigations, such as the design and characterization of the telescope, and development of the initial acquisition sensor.

In addition, the cross-coupling between angular and displacement degrees of freedom in the LTP interferometer has been investigated under representative conditions of the expected on-orbit residual test mass angular noise. Hardware simulations of this effect were performed by using PZT-actuated mirrors as movable test masses, which led to the quantification of the excess noise introduced into the length measurement that prevents the interferometer of reaching its required sensitivity in the overall observation band. In order to correct this excess noise, a noise subtraction technique capable of eliminating this noise contribution in the length measurement has been developed.

Moreover, this study required the assessment on the mechanical stability and steerability of piezo-electric transducers at the picometer level and millihertz frequencies, which is also an important finding for LISA, since the current baseline design foresees such components in the main optical path, like the point-ahead angle mechanism that was presented in Chapter 4.

A more general noise subtraction technique was also developed to characterize the coupling of noise sources in the LTP interferometer, and is capable of properly correct most of the sensitivity limiting factors, such as Doppler shift, laser frequency fluctuations, and non-linear optical pathlength difference noise. As it was presented in detail in Chapter 8, dedicated stabilization systems have been developed to counteract these specific noise sources.

This technique has not only proven the capability of subtracting the total noise contribution of these effects in a free-running measurement (no operative stabilizations), but it is also able to subtract excess noise that remained unsuppressed by the control loops. The fact that all required measurement information is available at the output of the LTP data management unit (DMU), allows to conduct measurement runs to fit the coupling of these noise source for in-orbit conditions, which is encouraged to be included as part of the LISA Pathfinder experimental master plan.

The noise subtraction algorithm itself is a time-domain routine which represents a suitable fall-back strategy in case of malfunction of the stabilizations or presence of excess noise remaining unsuppressed. Nevertheless, it is encouraged to conduct further studies on the algorithm, in order to improve the parameter estimations and even expanding the model to account for additional noise sources, such as temperature fluctuations.

For explanatory purposes, this noise subtraction technique and the angular noise subtraction algorithm were presented separately, but they can be regarded as a single method that accounts for the coupling of Doppler shift, non-linear OPD noise, laser frequency fluctuations, and the cross-talk between angular and displacement degrees of freedom, which has been shown to be significant.

Although the performance investigations presented in this Part were specifically conducted for the LTP interferometry, similar topics and techniques are expected to be investigated and further developed for LISA, such as the application of the real-time wavefront detector for characterization of the fiber injectors and the optical window, which are both currently included in the baseline design. The same applies to the results obtained from investigating the cross-talk between angular and displacement degrees of freedom, and the associated assessment of the stability of piezo-electric transducers. Noise subtraction techniques are common to have a wide application range, however, as mentioned in Chapter 9, their application must be performed carefully, as the input parameters and configuration of the algorithm strongly depend on the physical system to be analyzed.

CONCLUSIONS

This thesis presents the development and implementation of three different optical metrology techniques for the measurement of test mass attitude and displacement.

An optical cavity has been designed for displacement measurements at the level of $1 \, \mathrm{pm}/\sqrt{\mathrm{Hz}}$ in the millihertz frequency band. This test facility was developed for stability verification of prototypes of the LISA point-ahead angle mechanism. Initial testing demonstrated the required sensitivity at almost all frequencies, with the exception of an excess noise shoulder in the frequency range of $1 - 10 \, \mathrm{mHz}$. This limiting factor was traced to originate in the modulation system under the influence of temperature fluctuations, affecting the fiber-coupled electro-optic modulator. As part of subsequent investigations outside the scope of this thesis, the procurement of a vacuum compatible device that could be placed inside a thermally stable environment of $10^{-5} \, \mathrm{K}/\sqrt{\mathrm{Hz}}$, eventually led to a measurement noise floor completely below the requirements. However, test mass displacements of more than one laser wavelength are expected in space-based gravitational wave observations which would prevent to maintain the cavity in resonance, thus making resonant cavities not suitable for this application.

Furthermore, a homodyne interferometry technique based on the deep phase modulation (several radians) of one interferometer arm was developed. The phase modulation enables to operate the interferometer with constant high sensitivity over a wide dynamic range, thus overcoming the limitation of the previous method. Test mass attitude and displacement measurements conducted at the engineering model of the LTP optical bench resulted in readout sensitivities of better than $10 \, \mathrm{nrad}/\sqrt{\mathrm{Hz}}$ and $10 \, \mathrm{pm}/\sqrt{\mathrm{Hz}}$ at millihertz frequencies, respectively. Two main noise sources were identified and corrected in this experiment. One is the effect of the analog electronics that corrupts the relative amplitude of the frequency components used to extract the interferometer phase by a fit algorithm in the frequency domain. This error was removed by correcting the complex amplitudes with the corresponding complex value of the inverse transfer function of the analog electronics at the 10 frequencies of interest ($280, \, 560, \ldots, 2800 \, \mathrm{Hz}$). The second noise source is fluctuations of the laser frequency that proportionally translate to interferometer phase noise. This noise

source was treated in two different ways that yielded comparable results: (a) a commercial pre-stabilized laser system that is sufficiently stable in its frequency was used in a measurement; (b) an independent measurement of the laser frequency fluctuations is obtained from an additional interferometer on the LTP OB EM with intentionally large armlength mismatch. A noise subtraction algorithm uses this information to estimate the corresponding coupling factor into the phase measurement, and subtracts its contribution accordingly. The achieved readout sensitivity is comparable to the performance of the LTP interferometry within one order of magnitude, while applying a simpler modulation scheme at the expense of a more complex data processing required for the interferometer.

In addition, investigations on the baseline heterodyne interferometry designed for LISA Pathfinder were conducted. Its status, as of May 2009, is presented together with the development of a test facility for engineering models of the optical metrology subunits. The required test mass interferometric readout sensitivity of $20\,\mathrm{nrad}/\sqrt{\mathrm{Hz}}$ and $6.3\,\mathrm{pm}/\sqrt{\mathrm{Hz}}$ has been demonstrated with engineering models of the optical bench and laser assembly. A previously developed real-time wavefront detector was applied in the design and manufacture of quasi-monolithic fiber injectors for the LTP optical bench and the characterization of coated optical windows, leading to acceptable noise predictions of their potential effects on the noise level of the phase measurement. Hardware simulations of in-orbit test mass dynamics were conducted to characterize the cross-coupling between angular and displacement degrees of freedom in the LTP interferometer. Moreover, a time-domain noise subtraction technique capable to correct for sensitivity limiting effects like the coupling of test mass angular noise into displacement readout, and fluctuations of the laser frequency and non-linear optical pathlength difference was developed.

The fact that all required information is available in the spacecraft and that this technique works in the time-domain, makes it a feasible fall-back strategy in the case of malfunction of the active stabilizations or under the presence of excess noise remaining unsuppressed in order to continue producing high quality interferometric data for test mass and spacecraft control.

Picometer-accurate interferometry can be obtained by more than one technique, but there are always unexpected noise sources that can only be found in realistic experiments. Their removal requires various techniques such as auxiliary stabilizations or post-processing of the data. Auxiliary signals are indispensable for

diagnosis, characterization, and eventual removal – if possible – of these excess noise sources.

Part V

APPENDIX

A

LTPDA SCRIPT FOR NOISE SUBTRACTION ANALYSIS

This appendix gives a compact LTPDA script for the entire noise subtraction technique that considers: Doppler shift, non-linear OPD noise, laser frequency noise, and test mass angular jitter.

The output at the last stage of the analysis, which is in this case the output of the angular noise subtraction, psi1_noisesub and psi12_noisesub has been corrected from the noise contributions mentioned above. The script starts here:

```
%% LTPDA script for noise subtraction in the LTP interferometer
%  Doppler,OPD,laser frequency, and TM angular noise
%  F Guzman 20—05—09, Albert Einstein Institute Hannover
%% Start
mc;

%% Loading longitudinal phases raw data
rawphi1_doppler =ao('rawphi1.mat');%Loading rawphi1
rawphi12_doppler=ao('rawphi12.mat');%Loading rawphi12
rawphiF_doppler =ao('rawphiF.mat');%Loading rawphiF
rawphiR_doppler =ao('rawphiR.mat');%Loading rawphiR

%% Loading angular raw data
phi1  = ao( 'phi1.mat' );%Loading phi1
eta1  = ao( 'eta1.mat' );%Loading eta1
phi12 = ao( 'phi12.mat' );%Loading phi12
eta12 = ao( 'eta12.mat' );%Loading eta12

%% defines sample frequency for filter design
fs=rawphi1_doppler.fs;

%% DOPPLER CORRECTION ON RAW—PHASES
dpl=plist('bin',50);
rawphi1  = dopplercorr(rawphi1_doppler , dpl);
rawphi12 = dopplercorr(rawphi12_doppler, dpl);
```

```
rawphiF  = dopplercorr(rawphiF_doppler , dpl);
rawphiR  = dopplercorr(rawphiR_doppler , dpl);

%% Computing doppler—corrected difference phases
psi1=rawphi1—rawphiR;
psi12=rawphi12—rawphiR;
psiF=rawphiF—rawphiR;

%% OPD PRE—PROCESSING: TERMS COMPUTATION
% Computing OPD TERMS PSI_1
opdterm1a=sin((rawphiR+rawphi1)/2).*sin((rawphiR—rawphi1)/2); % sin((phiR
    +phiM)/2)*sin((phiR—phiM)/2)
opdterm1b=cos((rawphiR+rawphi1)/2).*sin((rawphiR—rawphi1)/2); % cos((phiR
    +phiM)/2)*sin((phiR—phiM)/2)
opdterm1c=sin(rawphiR+rawphi1).*sin(rawphiR—rawphi1); % sin(phiR+phiM)*
    sin(phiR—phiM)
opdterm1d=cos(rawphiR+rawphi1).*sin(rawphiR—rawphi1); % cos(phiR+phiM)*
    sin(phiR—phiM)
% Computing OPD TERMS PSI_12
opdterm12a=sin((rawphiR+rawphi12)/2).*sin((rawphiR—rawphi12)/2); % sin((
    phiR+phiM)/2)*sin((phiR—phiM)/2)
opdterm12b=cos((rawphiR+rawphi12)/2).*sin((rawphiR—rawphi12)/2); % cos((
    phiR+phiM)/2)*sin((phiR—phiM)/2)
opdterm12c=sin(rawphiR+rawphi12).*sin(rawphiR—rawphi12); % sin(phiR+phiM)
    *sin(phiR—phiM)
opdterm12d=cos(rawphiR+rawphi12).*sin(rawphiR—rawphi12); % cos(phiR+phiM)
    *sin(phiR—phiM)
% Computing OPD TERMS PSI_F
opdtermFa=sin((rawphiR+rawphiF)/2).*sin((rawphiR—rawphiF)/2); % sin((phiR
    +phiM)/2)*sin((phiR—phiM)/2)
opdtermFb=cos((rawphiR+rawphiF)/2).*sin((rawphiR—rawphiF)/2); % cos((phiR
    +phiM)/2)*sin((phiR—phiM)/2)
opdtermFc=sin(rawphiR+rawphiF).*sin(rawphiR—rawphiF); % sin(phiR+phiM)*
    sin(phiR—phiM)
opdtermFd=cos(rawphiR+rawphiF).*sin(rawphiR—rawphiF); % cos(phiR+phiM)*
    sin(phiR—phiM)

%% Band—pass filtering data
% Load bandpass second order [0.4 500] mHz
bppl = plist('type', 'bandpass','fs', fs,'fc',[0.0004 0.5],'order',2);
bp = miir( bppl ); fpl = plist(param('filter', bp));
% filtering difference phases
psi1bp  = filtfilt( psi1 , fpl);
psi12bp = filtfilt( psi12, fpl);
psiFbp  = filtfilt( psiF , fpl);
% filtering angular data
phi1bp  = filtfilt( phi1 , fpl);
eta1bp  = filtfilt( eta1 , fpl);
phi12bp = filtfilt( phi12, fpl);
```

```matlab
eta12bp = filtfilt( eta12, fpl);
% filter OPD terms PSI_1
opdterm1bpa  = filtfilt( opdterm1a , fpl);
opdterm1bpb  = filtfilt( opdterm1b , fpl);
opdterm1bpc  = filtfilt( opdterm1c , fpl);
opdterm1bpd  = filtfilt( opdterm1d , fpl);
% filter OPD terms PSI_12
opdterm12bpa  = filtfilt( opdterm12a , fpl);
opdterm12bpb  = filtfilt( opdterm12b , fpl);
opdterm12bpc  = filtfilt( opdterm12c , fpl);
opdterm12bpd  = filtfilt( opdterm12d , fpl);
% filter OPD terms PSI_F
opdtermFbpa  = filtfilt( opdtermFa , fpl);
opdtermFbpb  = filtfilt( opdtermFb , fpl);
opdtermFbpc  = filtfilt( opdtermFc , fpl);
opdtermFbpd  = filtfilt( opdtermFd , fpl);

%% OPD noise subtraction PSI_1
% LSCOV, coeffiecients estimation
coeffsOPD1  = lscov(opdterm1bpa, opdterm1bpb, opdterm1bpc, opdterm1bpd,
    psi1bp);
% Linear combination
psi1_opdnoisebp = lincom(opdterm1bpa, opdterm1bpb, opdterm1bpc,
    opdterm1bpd, coeffsOPD1);
psi1_opdnoisebp.setYunits('rad');
psi1_opdnoise = lincom(opdterm1a, opdterm1b, opdterm1c, opdterm1d,
    coeffsOPD1);
psi1_opdnoise.setYunits('rad');
% Noise subtraction
psi1_opdnsbp = psi1bp — psi1_opdnoisebp;
psi1_opdns = psi1 — psi1_opdnoise;

%% OPD noise subtraction PSI_12
% LSCOV, coeffiecients estimation
coeffsOPD12  = lscov(opdterm12bpa, opdterm12bpb, opdterm12bpc,
    opdterm12bpd,psi12bp);
% Linear combination
psi12_opdnoisebp = lincom(opdterm12bpa, opdterm12bpb, opdterm12bpc,
    opdterm12bpd, coeffsOPD12);
psi12_opdnoisebp.setYunits('rad');
psi12_opdnoise = lincom(opdterm12a, opdterm12b, opdterm12c, opdterm12d,
    coeffsOPD12);
psi12_opdnoise.setYunits('rad');
% Noise subtraction
psi12_opdnsbp = psi12bp — psi12_opdnoisebp;
psi12_opdns = psi12 — psi12_opdnoise;

%% OPD noise subtraction PSI_F
% LSCOV, coeffiecients estimation
```

```matlab
coeffsOPDF  = lscov(opdtermFbpa, opdtermFbpb, opdtermFbpc, opdtermFbpd,
    psiFbp);
% Linear combination
psiF_opdnoisebp = lincom(opdtermFbpa, opdtermFbpb, opdtermFbpc,
    opdtermFbpd, coeffsOPDF);
psiF_opdnoisebp.setYunits('rad');
psiF_opdnoise = lincom(opdtermFa, opdtermFb, opdtermFc, opdtermFd,
    coeffsOPDF);
psiF_opdnoise.setYunits('rad');
% Noise subtraction
psiF_opdnsbp = psiFbp — psiF_opdnoisebp;
psiF_opdns = psiF — psiF_opdnoise;

%% Laser frequency noise subtraction
% LSCOV, coefficients estimation
coeffs1F  = lscov(psiF_opdnsbp, psi1_opdnsbp); % coeffiecients for Psi_1
coeffs12F = lscov(psiF_opdnsbp, psi12_opdnsbp); % coeffiecients for
    Psi_12
% Linear combination
psi1_freqnoisebp = lincom(psiF_opdnsbp, coeffs1F);
psi1_freqnoise = lincom(psiF_opdns, coeffs1F);
psi1_freqnoisebp.setYunits('rad');
psi1_freqnoise.setYunits('rad');
%
psi12_freqnoisebp = lincom(psiF_opdnsbp, coeffs12F);
psi12_freqnoise = lincom(psiF_opdns, coeffs12F);
psi12_freqnoisebp.setYunits('rad');
psi12_freqnoise.setYunits('rad');
% Noise subtraction
psi1_freqnsbp = psi1_opdnsbp — psi1_freqnoisebp;
psi1_freqns  = psi1_opdns — psi1_freqnoise;
%
psi12_freqnsbp = psi12_opdnsbp — psi12_freqnoisebp;
psi12_freqns  = psi12_opdns — psi12_freqnoise;

%% Angular noise subtraction
coeffs_ang1 = lscov(phi1bp, eta1bp, psi1_freqnsbp);
coeffs_ang12 = lscov(phi1bp, eta1bp, phi12bp, eta12bp, psi12_freqnsbp);
% Linear combination
psi1_angnoise = lincom(phi1, eta1, coeffs_ang1);
psi1_angnoise.setYunits('rad');
%
psi12_angnoise= lincom(phi1, eta1, phi12, eta12, coeffs_ang12);
psi12_angnoise.setYunits('rad');
% Noise subtraction
psi1_noisesub  = psi1_freqns — psi1_angnoise;
%
psi12_noisesub = psi12_freqns — psi12_angnoise;
```

B

LTPDA GUI DIAGRAMS FOR NOISE SUBTRACTION ANALYSIS

This appendix presents a similar analysis as given in Appendix A (but does not include the test mass angular noise subtraction) and has been implemented[1] with the LTPDA GUI.

- Pre-processing: loads data, Doppler correction, and applies the band-pass filtering.
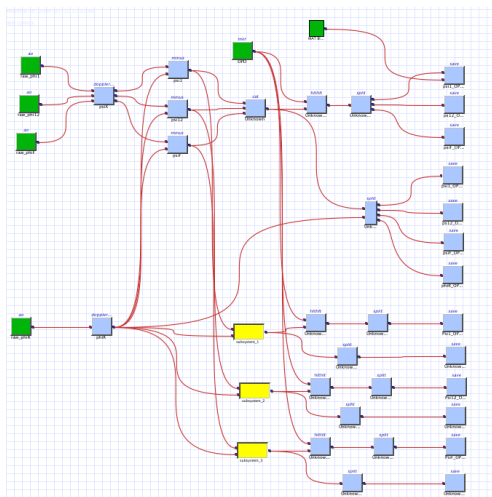
Figure 128: Block diagram of the noise subtraction algorithm performed with the LTPDA GUI.

---

1 This work was done together with Miquel Nofrarias.

- Subsystem (little yellow blows in the pre-processing stage): computation of non-linear OPD terms
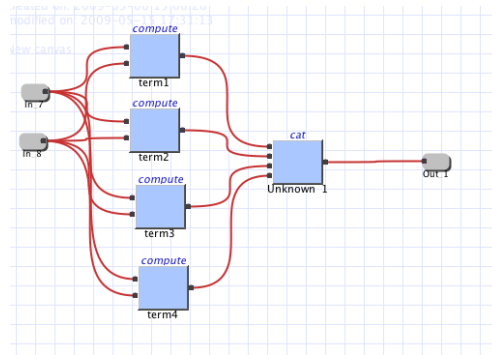

Figure 129: Subsystem: yellow blocks of pre-processing stage that compute the non-linear OPD terms.
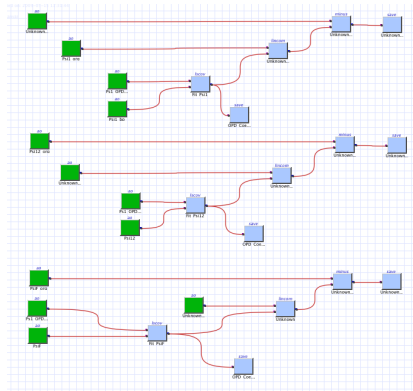
- OPD noise subtraction:

Figure 130: Block diagram of the OPD noise subtraction.
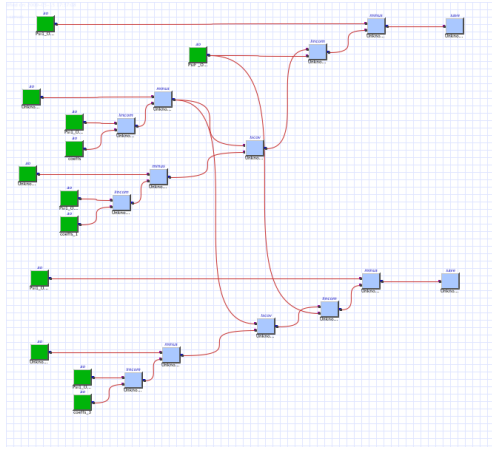
• Laser frequency noise subtraction:

Figure 131: Block diagram of the laser frequency noise subtraction.

BIBLIOGRAPHY

[1] Albert Einstein.
Prinzipielles zur allgemeinen Relativitätstheorie.
Annalen der Physik, 55, 1918.

[2] S. Skorupka.
Private communication.
2009.

[3] R. Gerndt.
S2-ASD-RS-3010: LTP OMS requirements specification.
Technical report, EADS Astrium Deutschland, 2007.

[4] Anthony E. Siegman.
Lasers.
University Science Books, 1986.

[5] Sascha Skorupka.
Rauschuntersuchungen an hochstabilen Lasersystemen für die wissenschaftliche Weltraummission LISA.
PhD thesis, University of Hannover and Max Planck Insitute for Gravitational Physics, 2007.
in German.

[6] Hild, S.
The status of GEO600.
Classical and Quantum Gravity, (23):643–651, 2006.

[7] E. Morrison, B.J. Meers, D.I. Robertson, H. Ward.
Experimental demonstration of an automatic alignment system for optical interferometers.
Applied Optics, 33:5037–5040, 1994.

[8] E. Morrison, B.J. Meers, D.I. Robertson, H. Ward.
Automatic alignment of optical interferometers.
Applied Optics, 33:5041–5049, 1994.

[9] F. Guzmán Cervantes, G. Heinzel, A. García Marín, V. Wand, F. Steier, O. Jennrich and K. Danzmann.
Real-time phase-front detector for heterodyne interferometers.
Applied Optics, 46, 2007.

[10] F. Guzmán Cervantes.
Real-time spatially resolving phasemeter for LISA Pathfinder.
Master's thesis, Albert Einstein Institute Hannover and University of Oldenburg, 2004.

[11] Yves Surrel.
Fringe Analysis.
P.K. Rastogi (Ed.):Photomechanics,Topics App. Phys. 77,55-102, 2000.

[12] Klaus Freischlad and Chris L. Koliopoulos.
Fourier description of digital phase-measuring interferometry.
J. Opt. Soc. Am. A. 7,542-551, 1990.

[13] Dennis C. Ghiglia and Louis A. Romero.
Robust two-dimensional weighted and unweighted phase unwrapping that uses fast transforms and iterative methods.
J. Opt. Soc. Am. A., 11, 1994.

[14] Thomas J. Flynn.
Two-dimensional phase unwrapping with minimum weighted discontinuity.
J. Opt. Soc. Am. A., 14, 1997.

[15] Dennis C. Ghiglia and Mark D. Pritt.
Two-Dimensional Phase Unwrapping: theory, algorithms, and software.
John Wiley & Sons, Inc., 1998.

[16] LISA study team.
Laser Intereferometer Space Antenna: A Cornerstone Mission for the Observation of Gravitational Waves.
2000.
System and Technology Study Report (ESA-SCI(2000)11).

[17] O. Jennrich.
Private communication.
2009.

[18] LISA-EST-SW-395: Point Ahead Angle Mechanism (PAAM) development for LISA.
Technical report, European Space Agency, 2006.

[19] Elliffe, EJ; Bogenstahl, J; Deshpande, A et al.
Hydroxide-catalysis bonding for stable optical systems for space.
Classical and Quantum Gravity, (22):257–267, 2005.

[20] B. Sheard, G. Heinzel.
Point-ahead angle mechanism (PAAM) testing.
Technical report, Albert Einstein Institute Hannover, 2007.

[21] Michael Tröbs.
Laser development and stabilization for the spaceborne interferometric gravitational wave detector LISA.
PhD thesis, University of Hannover, 2005.

[22] R. W. P. Drever, J. L. Hall, F. V. Kowalski, J. Hough, G. M. Ford, A. J. Munley and H. Ward.
Laser phase and frequency stabilization using an optical resonator.
Applied Physics B, 31, 1983.

[23] S. Scott *et al*.
MSE memo 93c: Thermal contact resistance for Viton O-rings.
`http://www.psfc.mit.edu/~sscott/MSEmemos/index.htm`, 2008.

[24] William J. Weber, Daniele Bortoluzzi, Antonella Cavalleri, Ludovico Carbone, Mauro Da Lio, Rita Dolesi, Giorgio Fontana, C. D. Hoyle, Mauro Hueller, and Stefano Vitale.
Position sensors for flight testing of LISA drag-free control.
Proceedings SPIE International Society of Optical Engineering, 31, 2002.

[25] R. Dolesi, D. Bortoluzzi, P. Bosetti, L. Carbone, A. Cavalleri, I. Cristofolini, M. DaLio, G. Fontana, V. Fontanari, B. Foulon, C. D. Hoyle, M. Hueller, F. Nappo, P. Sarra, D. N. A. Shaul, T. Sumner, W. J. Weber and S. Vitale.
Gravitational sensor for LISA and its technology demonstration mission.
Classical and Quantum Gravity, 20, 2003.

[26] Thilo Schuldt, Hans-Jürgen Kraus, Dennis Weise, Achim Peters, Ulrich Johann, and Claus Braxmaier.
A High Sensitivity Heterodyne Interferometer as Optical Readout for the LISA Inertial Sensor.
AIP Conf Proc, 873:374–378, November 2006.

Merkowitz S and Livas JC eds Proceedings of the 6th LISA Symposium.

[27] Stuart M. Aston and Clive C. Speake.
An Interferometric Based Optical Read-Out Scheme For The LISA Proof-Mass.
AIP Conf Proc, 873:326–333, November 2006.
Merkowitz S and Livas JC eds Proceedings of the 6th LISA Symposium.

[28] Fausto Acernese, Rosario De Rosa, Luciano Di Fiore, Fabio Garufi, Adele La Rana, and Leopoldo Milano.
Some Progress In The Development Of An Optical Readout System For The LISA Gravitational Reference Sensor.
AIP Conf Proc, 873:339–343, November 2006.
Merkowitz S and Livas JC eds Proceedings of the 6th LISA Symposium.

[29] G. Heinzel.
Optical Readout for LISA: deep internal modulation.
First LISA Optical Readout Meeting, June 2005.

[30] Sudarshanam, VS; Srinivasan, K.
Linear readout of dynamic phase-change in a fiber-optic homodyne interferometer.
Optics Letters, (14):140–142, 1989.

[31] Jin, W; Zhang, LM; Uttamchandani, D; Culshaw, B.
Modified J1 ... J4 method for linear readout of dynamic phase-changes in a fiberoptic homodyne interferometer.
Applied Optics, (30):4496–4499, 1991.

[32] Sudarshanam, VS; Claus, RO.
Generic J1...J4 method of optical-phase detection: Accuracy and range enhancement.
Journal of modern optics, (40):483–492, 1993.

[33] Gerhard Heinzel.
Advanced optical techniques for laser-interferomertric gravitational-wave detectors.
PhD thesis, University of Hannover and Max Planck Institute for Quantum Optics, 1999.
MPQ report 243.

[34] I. S. Gradstein, I. M. Ryzhik.
Table of Integrals, Series and Products.
Academic Press, San Diego, 5th edition, 1994.

[35] J. A. Nelder, R. Mead.
A simplex method for function minimization.
Computer Journal, (7):308–313, 1965.

[36] Marquardt, D.
An Algorithm for Least-Squares Estimation of Nonlinear Parameters.
SIAM Journal on Applied Mathematics, (11):431–441, 1963.

[37] William H. Press, Saul A. Teukolsky, William T. Vetterling, Brian P. Flannery.
Numerical Recipes in C.
(2nd edition):431–441, 1992.

[38] G. Heinzel, F. Guzmán.
paper in preparation.

[39] I. Freitag, A. Tünnermann, H. Welling.
Power scaling of diode-pumped monolithic Nd:YAG lasers to output powers of several watts.
Optics Communications, 1995.

[40] Antonio F. García Marín.
Minimisation of pathlength noise for LISA.
PhD thesis, University of Hannover and Max Planck Insitute for Gravitational Physics, 2007.

[41] Heinzel, G; Braxmaier, C; Caldwell, M; Danzmann, K; Draaisma, F; Garcia, A; Hough, J; Jennrich, O; Johann, U; Killow, C; Middleton, K; te Plate, M; Robertson, D; Rudiger, A; Schilling, R; Steier, F; Wand, V; Ward, H.
Successful testing of the LISA Technology Package (LTP) interferometer engineering model.
Classical and Quantum Gravity, (22):149–154, 2005.

[42] FFTW subroutine package.
`http://www.fftw.org/`.

[43] V. Wand, J. Bogenstahl, C. Braxmaier, K. Danzmann, A. García, F. Guzmán, G. Heinzel, J. Hough, O. Jennrich, C. Killow, D. Robertson, Z. Sodnik, F. Steier, and H. Ward.
Noise sources in the LTP heterodyne interferometer.
Classical and Quantum Gravity, 23, 2006.

[44] G. Heinzel, A. García, V. Wand, F. Guzmán, F. Steier, C. Killow, D. Robertson, H. Ward, C. Braxmaier.

S2-AEI-TN-3028: Investigation of noise sources in the LTP interferometer.
Technical report, Albert Einstein Institute Hannover, University of Glasgow, and EADS Astrium Deutschland, 2005.

[45] G. Heinzel, V. Wand, A. García, O. Jennrich, C. Braxmaier, D. Robertson, K.Middleton, D. Hoyland, A. Rüdiger, R. Schilling, U. Johann, K Danzmann.
The LTP interferometer and Phasemeter.
Classical and Quantum Gravity, 21:581–587, 2004.

[46] F. Guzmán Cervantes, F. Steier, G. Wanner, G. Heinzel, K. Danzmann.
Subtraction of test mass angular noise in the LISA technology package interferometer.
Applied Physics B, 90, 2008.

[47] Anza, S. et al.
The LTP experiment on the LISA Pathfinder mission.
Classical and Quantum Gravity, (22):125–138, 2005.

[48] G. Heinzel, C. Braxmaier, R. Schilling, A. Rüdiger, D. Robertson, M. te Plate, V. Wand, K. Arai, U. Johann, K. Danzmann.
Interferometry for the LISA technology package (LTP) aboard SMART-2.
Classical and Quantum Gravity, 20, April 2003.

[49] Braxmaier, Claus; Heinzel, Gerhard; Middleton, Kevin; Caldwell, Martin E.; Konrad, W.; Stockburger, H.; Lucarelli, S.; te Plate, Maurice B.; Wand, V.; Garcia, Antonio C.; Draaisma, F.; Pijnenburg, J.; Robertson, D. I.; Killow, Christian J.; Ward, Harry; Danzmann, Karsten; Johann, Ulrich.
LISA pathfinder optical interferometry.
Proceedings of SPIE: Gravitational Wave and Particle Astrophysics Detectors, 5500, 2005.

[50] J Bogenstahl, L Cunningham, E D Fitzsimons, J Hough, C J Killow, M Perreur-Lloyd, D Robertson, S Rowan and H Ward.
LTP fibre injector qualification and status.
Journal of Physics: Conference Series, 154, 2009.

[51] U. Denskat.
S2-ASD-RS-3018 Phasemeter Processing and Laser Control Specification 3.0.
Technical report, EADS Astrium Deutschland, 2008.

[52] A. García *et. al.*
paper in preparation.

[53] G. Heinzel.
*LISO – Program for **L**inear **S**imulation and **O**ptimization of analog electronic circuits.*

[54] LTPDA: a MATLAB toolbox for accountable and reproducible data analysis.
`http://www.lisa.aei-hannover.de/ltpda/`.

[55] M. Hewitson, M. Armano, M. Benedetti, J. Bogenstahl, D. Bortoluzzi, P. Bosetti, N. Brandt, A. Cavalleri, G. Ciani, I. Cristofolini, M. Cruise, K. Danzmann, I. Diepholz, R. Dolesi, J. Fauste, L. Ferraioli, D. Fertin, W. Fichter, A. García, C. García, A. Grynagier, F. Guzmán, E. Fitzsimons, G. Heinzel, D. Hollington, J. Hough, M. Hueller, D. Hoyland, O. Jennrich, B. Johlander, C. Killow, A. Lobo, D. Mance1, I. Mateos, P. W. McNamara, A. Monsky, D. Nicolini, D. Nicolodi, M. Nofrarias, M. Perreur-Lloyd, E. Plagnol, G. D. Racca, J. Ramos-Castro, D. Robertson, J. Sanjuan, M. O. Schulte, D. N. A. Shaul, M. Smit, L. Stagnaro, F. Steier, T. J. Sumner, N .Tateo, D. Tombolato, G. Vischer, S. Vitale, G. Wanner, H. Ward, S. Waschke11, V. Wand, P. Wass, W. J. Weber, T. Ziegler and P. Zweifel.
Data analysis for the LISA Technology Package.
Classical and Quantum Gravity, 26, 2009.

[56] H. Ward, C. Killow, D. Robertson.
S2-UGL-DDD-3004: OBI - Revised Fibre Injector Design.
Technical report, University of Glasgow, 2008.

[57] W. Fichter.
Private communication.
2006.

[58] G. Heinzel.
S2-AEI-TN-3034: Generation of random time series with prescribed spectra.
Technical report, Albert Einstein Institute Hannover, 2006.

[59] G. Wanner, G. Heinzel.
S2-AEI-TN-3051: LTP OBI alignment simulations.
Technical report, Albert Einstein Institute Hannover, 2008.

[60] A. Monsky, F. Steier, A. García, M. Hewitson, M. Nofrarias, G. Heinzel.
S2-AEI-TN-3058: OPD noise investigations for LTP.
Technical report, Albert Einstein Institute Hannover, 2009.

[61] G. Heinzel.
Private communication.
2009.

ACKNOWLEDGMENTS

FELIPE GUZMÁN CERVANTES

PERSONAL INFORMATION

address	Philipsbornstr. 14, 30165 Hannover, Germany.
born on	September 24th, 1980 in San José, Costa Rica.
citizenship	Costa Rican, German.
email	felipe.guzman@nasa.gov

EDUCATION

04/2005–06/2009 Doctoral studies in Physics, Albert Einstein Institute (Max Planck Institute for Gravitational Physics and Leibniz Universität Hannover), Hannover, Germany.

10/2002–02/2005 Master of Science in Physics, Carl-von-Ossietzky Universität Oldenburg, Oldenburg, Germany.

03/1998–09/2001 Bachelor in Electrical Engineering, Universidad de Costa Rica, San José, Costa Rica.

02/1993–12/1997 High school, San José, Costa Rica.

03/1987–12/1992 Primary school, San José, Costa Rica.

PROFESSIONAL INFORMATION

10/2003–07/2009 Scientific assistant, Albert Einstein Institute, Hannover, Germany.

02/2006–05/2006 Visiting scientist, University of Glasgow, UK.

05/2005–04/2007 Member of the European Graduate College for Interference and Quantum Applications.

04/2007–04/2009 Member of the International Max Planck Research School on Gravitational Wave Astronomy.

PUBLICATIONS

[1] M. Hewitson, M. Armano, M. Benedetti, J. Bogenstahl, D. Bortoluzzi, P. Bosetti, N. Brandt, A. Cavalleri, G. Ciani, I. Cristofolini, M. Cruise, K. Danzmann, I. Diepholz, R. Dolesi, J. Fauste, L. Ferraioli, D. Fertin, W. Fichter, A. García, C. García, A. Grynagier, F. Guzmán, E. Fitzsimons, G. Heinzel, D. Hollington, J. Hough, M. Hueller, D. Hoyland, O. Jennrich, B. Johlander, C. Killow, A. Lobo, D. Mance, I. Mateos, P. W. McNamara, A. Monsky, D. Nicolini, D. Nicolodi, M. Nofrarias, M. Perreur-Lloyd, E. Plagnol, G. D. Racca, J. Ramos-Castro, D. Robertson, J. Sanjuan, M. O. Schulte, D. N. A. Shaul, M. Smit, L. Stagnaro, F. Steier, T. J. Sumner, N. Tateo, D. Tombolato, G. Vischer, S. Vitale, G. Wanner, H. Ward, S. Waschke, V. Wand, P. Wass, W. J. Weber, T. Ziegler and P Zweifel.
Data analysis for the LISA Technology Package.
Class. Quantum Grav., 26, 2009.

[2] M. Armano, M. Benedetti, J. Bogenstahl, D. Bortoluzzi, P. Bosetti, N. Brandt, A. Cavalleri, G. Ciani, I. Cristofolini, A.M. Cruise, K. Danzmann, I. Diepholz, G. Dixon, R. Dolesi, J. Fauste, L. Ferraioli, D. Fertin, W. Fichter, M. Freschi, A. García, C. García, A. Grynagier, F. Guzmán, E. Fitzsimons, G. Heinzel, M. Hewitson, D. Hollington, J. Hough, M. Hueller, D. Hoyland, O. Jennrich, B. Johlander, C. Killow, A. Lobo, D. Mance, I. Mateos, P.W. McNamara, A. Monsky, D. Nicolini, D. Nicolodi, M. Nofrarias, M. Perreur-Lloyd, E. Plagnol, G.D. Racca, J. Ramos-Castro, D. Robertson, J. Sanjuan, M.O. Schulte, D.N.A. Shaul, M. Smit, L. Stagnaro, F. Steier, T.J. Sumner, N. Tateo, D. Tombolato, G. Vischer, S. Vitale, G. Wanner, H. Ward, S. Waschke, V. Wand, P. Wass, W.J. Weber, T. Ziegler and P. Zweifel.
LISA Pathfinder: the experiment and the route to LISA.
Class. Quantum Grav., 26, 2009.

[3] A. Monsky, M. Hewitson, L. Ferraioli, G. Wanner, M. Nofrarias, M. Hueller, I. Diepholz, A. Grynagier, M. Armano, M. Benedetti, J. Bogenstahl, D. Bortoluzzi, P. Bosetti, N. Brandt, A. Cavalleri, G. Ciani, I. Cristofolini, M. Cruise, K. Danzmann, R. Dolesi, J. Fauste, D. Fertin, W. Fichter, A. García, C. García, F. Guzmán, E. Fitzsimons, G. Heinzel, D. Hollington, J. Hough, D. Hoyland, O. Jennrich, B. Johlander, C. Killow, A. Lobo,

D. Mance, I. Mateos, P. W. McNamara, D. Nicolini, D. Nicolodi, M. Perreur-Lloyd, E. Plagnol, G. D. Racca, J. Ramos-Castro, D. Robertson, J. Sanjuan, M. O. Schulte, D. N. A. Shaul, M. Smit, L. Stagnaro, F. Steier, T. J. Sumner, N. Tateo, D. Tombolato, G. Vischer, S. Vitale, H. Ward, S. Waschke, P. Wass, W. J. Weber, T. Ziegler and P. Zweifel.
The first mock data challenge for LISA Pathfinder.
Class. Quantum Grav., 26, 2009.

[4] F. Steier, F. Guzmán Cervantes, A. F. García Marín, D. Gerardi, G. Heinzel and K. Danzmann.
The end-to-end testbed of the optical metrology system on-board LISA Pathfinder.
Class. Quantum Grav., 26, 2009.

[5] Marina Dehne, Felipe Guzmán Cervantes, Benjamin Sheard, Gerhard Heinzel and Karsten Danzmann.
Laser interferometer for spaceborne mapping of the Earth's gravity field.
J. Phys.: Conf. Ser., 154, 2009.

[6] M. Dehne, F. Guzmán Cervantes, B. Sheard, G. Heinzel and K. Danzmann.
Laser Interferometer for a GRACE follow-on mission.
IAG Symposia series, 90, 2008.

[7] F. Guzmán Cervantes, F. Steier, G. Wanner, G. Heinzel, K. Danzmann.
Subtraction of test mass angular noise in the LISA technology package interferometer.
Applied Physics B, 90, 2008.

[8] F. Guzmán Cervantes, G. Heinzel, A. García Marín, V. Wand, F. Steier, O. Jennrich and K. Danzmann.
Real-time phase-front detector for heterodyne interferometers.
Applied Optics, 46, 2007.

[9] V. Wand, F. Guzmán, G. Heinzel, K. Danzmann.
LISA Phasemeter development.
AIP Conference Proceedings, 873, 2006.

[10] A. García Marín, J. Bogenstahl, F. Guzmán Cervantes, F. Steier, J. Reiche, S. Skorupka, V. Wand, M. Nofrarias, J. Sanjuan, O. Jennrich, G. Heinzel, and K. Danzmann.
Interferometric characterization of the optical window for LISA Pathfinder and LISA.
AIP Conference Proceedings, 873, 2006.

[11] C. Killow, J. Bogenstahl, F. Guzmán Cervantes, M. Perreur-Lloyd, D. Robertson, F. Steier, and H. Ward.
Construction of the LTP Optical Bench Interferometer.
AIP Conference Proceedings, 873, 2006.

[12] G. Heinzel, J. Bogenstahl, C. Braxmaier, K. Danzmann, A. García, F. Guzmán, J. Hough, D. Hoyland, O. Jennrich, C. Killow, D. Robertson, Z. Sodnik, F. Steier, H. Ward and V. Wand.
Interferometry for the LISA technology package LTP: an update.
Journal of Physics: Conference Series, 32, 2006.

[13] V. Wand, J. Bogenstahl, C. Braxmaier, K. Danzmann, A. García, F. Guzmán, G. Heinzel, J. Hough, O. Jennrich, C. Killow, D. Robertson, Z. Sodnik, F. Steier, and H. Ward.
Noise sources in the LTP heterodyne interferometer.
Classical and Quantum Gravity, 23, 2006.

[14] A. García Marín, V. Wand, F. Steier, F. Guzmán Cervantes, J. Bogenstahl, O. Jennrich, G. Heinzel and K. Danzmann.
On-orbit alignment and diagnostics for the LISA Technology Package.
Classical and Quantum Gravity, 23, 2006.

[15] A. García Marín, G. Heinzel, R. Schilling, A. Rüdiger, V. Wand, F. Steier, F. Guzmán Cervantes, A. Weidner, O. Jennrich, F. Meca Meca and K. Danzmann.
Phase locking to a LISA arm: first results on a hardware model.
Classical and Quantum Gravity, 22, 2005.